**General Disclaimer**

One or more of the Following Statements may affect this Document

- This document has been reproduced from the best copy furnished by the organizational source. It is being released in the interest of making available as much information as possible.

- This document may contain data, which exceeds the sheet parameters. It was furnished in this condition by the organizational source and is the best copy available.

- This document may contain tone-on-tone or color graphs, charts and/or pictures, which have been reproduced in black and white.

- This document is paginated as submitted by the original source.

- Portions of this document are not fully legible due to the historical nature of some of the material. However, it is the best reproduction available from the original submission.
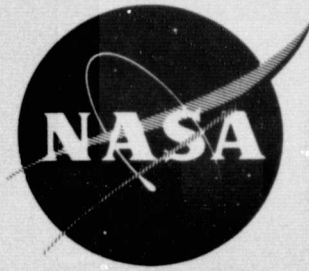
Produced by the NASA Center for Aerospace Information (CASI)

DETAILED TECHNICAL REPORT

"APPLICATION OF REMOTE SENSING FOR
PREDICTION AND DETECTION OF THERMAL POLLUTION"
(PHASE 2)

by

T. Nejat Veziroglu and Samuel S. Lee

prepared for

NATIONAL AERONAUTICS AND SPACE ADMINISTRATION

NASA CONTRACT NAS10 — 8740

Department of Mechanical Engineering

School of Engineering and Environmental Design

University of Miami

Coral Gables, Florida

December, 1975

STANDARD TITLE PAGE

1. Report No. CR-139188	2. Government Accession No.	3. Recipient's Catalog No.
4. Title and Subtitle Application of Remote Sensing for Prediction and Detection of Thermal Pollution (Phase 2)		**5. Report Date** December, 1975
		6. Performing Organization Code
7. Author(s) T. Nejat Veziroglu and Samuel S. Lee		**8. Performing Organization Report No.**
9. Performing Organization Name and Address Department of Mechanical Engineering School of Engineering and Environmental Design, University of Miami Coral Gables, Florida, 33124		**10. Work Unit No.**
		11. Contract or Grant No. NAS10-8740
12. Sponsoring Agency Name and Address John F. Kennedy Space Center Kennedy Space Center, Florida		**13. Type of Report and Period Covered** Detailed Technical Report
		14. Sponsoring Agency Code

15. Supplementary Notes

16. Abstract This report covers the second phase of a three year project aimed at the development of a predictive mathematical model for thermal pollution in connection with remote sensing measurements. This study serves the following purposes: (1) the development and testing of a generalized mathematical model to predict three-dimensional temperature and salinity distribution in coastal regions receiving hot discharges; and (2) the investigation of the thermal remote sensing systems by directly relating them to thermal radiation from the sea surfaces and by better accounting for the absorption in the atmosphere. In this twelve-month period, the rigid-lid model has been developed and its application to far-field study has been completed. The velocity and temperature fields have been computed for different atmospheric conditions and for different boundary currents produced by tidal effects. In connection with the theoretical work, six experimental studies of the two sites in question (Biscayne Bay site and Hutchinson Island site) have been carried out. The temperature fields obtained during the tests at the Biscayne Bay site have been compared with the predictions of the rigid-lid model study. The comparison of the theoretical and experimental results is encouraging. The rigid-lid model is also being applied to near-field study. Preliminary results for a simple case have been obtained and execution of more realistic cases has been initiated.

In parallel with the above described work, the development of a free-surface model has been initiated. The governing equations have been formulated and the computer programs have been written. De-bugging of the computer program is in progress.

17. KeyWords Thermal Pollution, Remote Sensing, Mathematical Model	18. Distribution Statement

19. Security Classif.(of this report) Unclassified	20. Security Classif.(of this page) Unclassified	21. No. of Pages	22. Price

KSC FORM 16-272 (5/72)

Detailed Technical Report

Application of Remote Sensing for Prediction and Detection of Thermal Pollution (Phase 2)

by

T. Nejat Veziroglu & Samuel S. Lee

Prepared for:

Department of Mechanical Engineering
School of Engineering and Environmental Design
University of Miami
Coral Gables, Florida

December, 1975

University of Miami

Thermal Pollution Research Team

Principal Investigators:

Dr. T. Nejat Veziroglu
Director, Clean Energy Research Institute
and
Associate Dean for Research

Dr. Samuel S. Lee
Director, Thermal Pollution Research Laboratory
and
Chairman, Mechanical Engineering Department

Investigators:

Dr. Homer Hiser
Director, Remote Sensing Laboratory

Dr. Norman Weinberg
Professor of Electrical Engineering

Dr. Joseph Hirschberg
Director, Optics Laboratory

Dr. Subrata Sengupta
Research Assistant Professor

Research Assistants:

Mr. James Byrne

Mr. Ching-Fen Tsai

Ms. Donna Rona

TABLE OF CONTENTS

I. INTRODUCTION

A major source of the thermal pollution of rivers, lakes and estuaries is the hot water discharges from power plants. As the demand for electric power in this country continues to increase, more and more power plants will be built. The trend is that large power plants, including more nuclear powered stations, will be built, and groups of these units will be located at a single site - usually in coastal areas. This will result in sharp increases in thermal pollution. Thus, proper management of the water resources and the related thermal pollution problems is essential to preserve the environment in estuarine and coastal marine waters. In order to achieve this goal it is necessary to have a thorough understanding of the motion and diffusion of thermal discharges and the extent of the region affected. To obtain the understanding of the hydrodynamics and thermodynamics of earth's water basins requires extensive field data collection. Even the most rudimentary data acquisition field trip is extremely expensive. Experimental observations from physical models are often unsatisfactory owing to the impossibility of obtaining appropriate similarity. Developing theoretical predictive ability is considered to be the better way to obtain the large volume of information required to understand the environment. Models can be used predictively to arrive at meaningful decision parameters a priori for site selection for power plants and other modifying factors.

In a NASA sponsored feasibility study (refs.1 and 2)completed in January 1974, a team of researchers at the University of Miami concluded that it is feasible to develop a generalized three-dimensional predictive, mathematical model, involving remote sensing and in-situ measurements to supply necessary parameters. It was recommended that the development of the mathematical model be conducted over four phases covering a time

period of three years. Three sites were proposed to be used
for the development and testing of the model. These three
power plant sites are the Florida Power and Light Company's
Turkey Point and Cutler Ridge facilities, and Port St. Lucie
Nuclear Power Plant units on Hutchinson Island. These three
sites are located in South Florida, close to both the Kennedy
Space Center and the University of Miami. Another interesting
feature is their geographical contrast. The Turkey Point and
Cutler Ridge facilities are located at a shallow lagoon type
estuary, while the Hutchinson plant discharges into the off-
shore continental shelf. These sites should provide a good
test area for the generalized nature of the proposed three-
dimensional model. The initial plan was that a single model
would be developed for application to thermal pollution prob-
lems caused by thermal discharges with a six-month Phase I
study to conduct preliminary model development. A twelve-
month Phase II study was to be devoted to model developing
using Biscayne Bay site as a test case. A twelve-month Phase
III study was to apply the model to the Hutchinson Island site.
A six-month final phase study was to be used for evaluation
and assessment of the mathematical model. As time passed, a
closed circuit cooling canal system was constructed for the
Turkey Point facility and hot water was no longer discharged
into the lower Biscayne Bay from this plant. The study plan
was modified accordingly with the model study in Biscayne Bay
concentrated on the Cutler Ridge Power Plant site. The first
phase of the project covered the period March 1974 through
October 1974. At the conclusion of the first phase study it
was found that a division of the model into near and far
fields would be more desirable to describe the details of the
plume as well as the larger recipient domain. It was also
found that in a large number of locations, namely inland
lakes, surface waves were not an important factor and could
be ignored to save computation time. This prompted division

of the modeling effort to rigid-lid and free-surface applications. The final report for the Phase I study includes the detailed rational and formulation of the separate programs. It should be noted that there are essentially two basic programs, the rigid-lid and the free-surface. They are applied to near and far field studies by appropriate modification to the boundary inputs to the model and the grid size to be used. However, the initial modification from far-field to near-field for either the rigid-lid or the free surface model is not trivial. In that sense there are four modeling efforts. During the period of the first phase study, the equipment for in-situ measurements was ordered, calibrated and tested. A data gathering test was carried out at the Biscayne Bay site. The theoretical study was initiated with a rigid-lid model (assuming fixed surface level). The model was formulated, the computer program developed and de-bugged.

The present contract, which was initiated on October 15, 1974 and covers a period of twelve months, covers the second phase of the model development. This study (refs. 3 and 4) serves the following purposes: (1) the development and testing of a generalized mathematical model to predict three-dimensional temperature and salinity distribution in coastal regions receiving hot discharges; and (2) the investigation of the thermal remote sensing systems by directly relating them to thermal radiation from the sea surfaces and by better accounting for the absorption in the atmosphere. This study program is being carried out in four parts. They are closely related and are to be conducted concurrently. The mathematical model development is the major part of the project. Remote sensing and in-situ measurements are needed to support the model development. At the same time, a turbidity remote sensing system is being developed. The relationship between these various phases of the study may be shown by a flow

diagram in Fig. I-1.

In this twelve-month period, the rigid-lid model has been developed and its application to far-field study has been completed. The velocity and temperature fields have been computed for different atmospheric conditions and for different boundary currents produced by tidal effects. The computations have been carried out for different time periods between 1 and 6 hours of real time. In parallel with the theoretical work, six experimental studies of the two sites in question (Biscayne Bay site and Hutchinson Island site) have been carried out. Four of the data gathering experiments were carried out at the Biscayne Bay site. Three of the experiments included airborne infrared data gathering by NASA-6 aircraft. Two experiments have been carried out at the Hutchinson Island site, one of which included airborne infrared data recording. The temperature fields obtained during the tests at the Biscayne Bay site have been compared with the predictions of the rigid-lid model study. The comparison of the theoretical and experimental results is encouraging.

In parallel with the above described work, the development of a free-surface model has been initiated. In this model the water surface level changes will be included. The governing equations have been formulated and the computer programs have been written. De-bugging of the computer program is in progress.

When the project is concluded, two important benefits will be obtained, viz., (1) it will be possible to select the proper sites for the future power stations so that they may cause little or no pollution, and (2) it will be possible to remotely monitor the discharges from the existing and future power plants to make sure that they do not exceed the allowable temperature limits and do not pollute.

REFERENCES

1. Veziroglu, T.N., and Lee, S.S., "Detailed Technical Report: Feasibility of Remote Sensing for Detecting Thermal Pollution," NASA Contract NAS 10-8402 Final Report, NASA CR-134453, December 1973.

2. Veziroglu, T.N., and Lee, S.S., "Executive Summary Report: Feasibility of Remote Sensing for Detecting Thermal Pollution," NASA Contract NAS 10-8402 Executive Report, December 1973.

3. Veziroglu, T.N., and Lee, S.S., "Detailed Technical Report: Prediction and Detection of Thermal Pollution," NASA Contract NAS 10-8498, Final Report, NASA CR-139182 October 1974.

4. Veziroglu, T.N., and Lee, S.S., "Executive Summary Report: Prediction and Detection of Thermal Pollution," NASA Contract NAS 10-8498, Executive Report, October 1974.
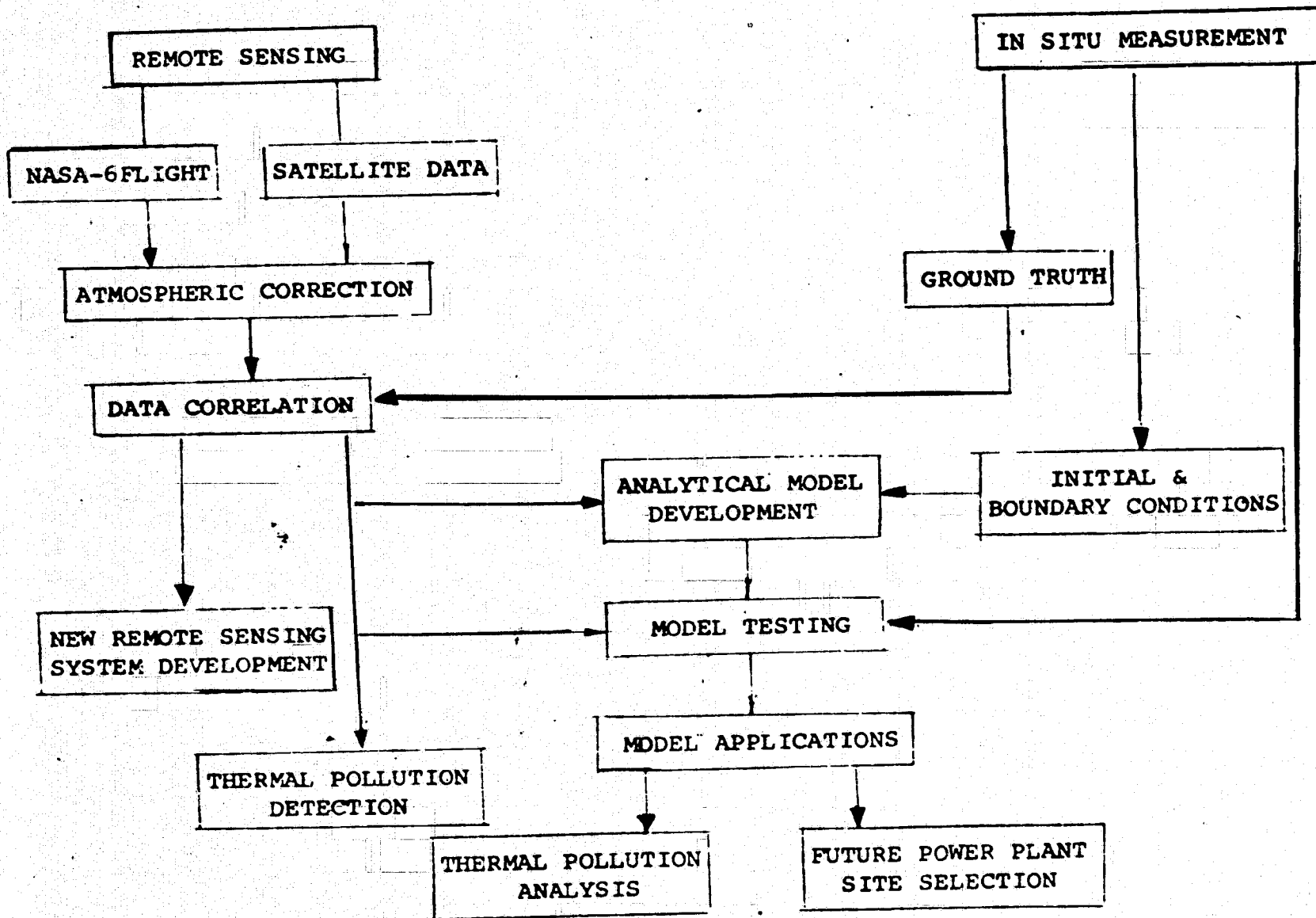
REMOTE SENSING

IN SITU MEASUREMENT

NASA-6 FLIGHT

SATELLITE DATA

ATMOSPHERIC CORRECTION

GROUND TRUTH

DATA CORRELATION

ANALYTICAL MODEL DEVELOPMENT

INITIAL & BOUNDARY CONDITIONS

NEW REMOTE SENSING SYSTEM DEVELOPMENT

MODEL TESTING

THERMAL POLLUTION DETECTION

MODEL APPLICATIONS

THERMAL POLLUTION ANALYSIS

FUTURE POWER PLANT SITE SELECTION

-9-

Fig. I-1. Relationships Between Various Phases of the Program.

II. GROUND TRUTH AND IN-SITU MEASUREMENTS

Ground truth is primarily a service function for the other parts of the project, such as Model Development and Remote Sensing, and, consequently, is not an "end product" by itself. Data from the field tests will be presented both here and in the Remote Sensing section.

A. Background

The major functions of this part of the project are to provide:

1) Ground truth for evaluation of remotely sensed measurements,

2) Boundary conditions and verification of the mathematical model, and

3) Assistance in the development of new techniques for remote sensing.

To perform these functions, the following duties are involved:

1) Ordering of instrumentation,

2) Calibration and testing of instruments,

3) Assistance in coordinating and planning field tests (boat trips with and without aircraft),

4) Supervision of measurements during field trips, and

5) Reduction of data and preparation of data records.

The quantities of interest in the measurement program are:

1) Temperatures at the surface and at various depths measured by direct means,

2) Surface temperature measured by infrared sensor (heat spy) for comparison with airborne thermal scanner,

3) Current speed and direction,

4) Salinity, and

5) Pertinent meteorological data, such as atmospheric temperature, wind speed and direction, humidity, and tidal information.

Direct temperatures are sensed by thermistors and the accuracy of these measurements is limited only by the calibration. At present, this is about $0.2^{\circ}C$, which is more than adequate both for correlating with the remote readings and providing the necessary information for the mathematical model. The other measurements will be discussed elsewhere.

B. Measurement System for Biscayne Bay

Most of the instruments discussed in detail in previous reports are currently being used for this phase of the project. Several changes have been made, however, to correct certain problem areas and to improve the system. Measurement of the resistance of the thermistors was somewhat difficult because the boat motion deflected the galvanometer in the wheatstone bridge. A digital type null device was designed to correct this fault and it operated satisfactorily. However, the bridge-null indicator measurement is still a fairly slow procedure. A direct resistance indicator with digital display (Fluke Model 8000A) has been used during the recent tests and has performed well. The accuracy is consistent with system requirements and the measurements have been repeatable.

As stated in previous reports, the modification to the General Oceanics Current Meter, which provides for audible signals to indicate the number of revolutions of the impeller blade, has proven very satisfactory for averaging the current flow over a short period, thus resulting in an average value

rather than an instantaneous one which could be misleading.
The counter also enables us to measure very low currents, which
are prevalent in many parts of Biscayne Bay.

The salinity measurements have been a problem.
Direct conductivity type instruments have proven unsatisfactory
due to the critical nature of the platinization of the elec-
trodes.   This appears to be a common fault of this type of in-
strument; accordingly, an induction type meter was purchased
(Beckman Type RSS-3), which measures conductivity and hence
salinity by noting the effect the conducting liquid has on a
calibrated oscillator.   This also has the advantage that it
can be quickly recalibrated by inserting a known resistance in
a loop through the sensor.   The initial calibration was done
chemically using known samples of saline solutions.   Performance
appeared to be satisfactory during the April 15 field trip but,
unfortunately, several readings were beyond the scale of the
instrument due to the highly saline condition of portions of
Biscayne Bay, a result of the prolonged dry spell in this area.
Satisfactory readings were obtained during the Sept. 4, 1975,
field trip in Biscayne Bay and the Sept. 18, 1975, measurements
off Hutchinson Island.

C.   Instruments for Hutchinson Island

Several additional instruments were added for the
experiments off Hutchinson Island because the water at the out-
let of the nuclear power plant is much deeper.   Rather than
splice the wires of the present thermistors, several new tem-
perature sensors were purchased with 60 feet of cable.   Under-
water splices may not be reliable and could be a serious problem
if a failure occurred during a field trip.

A new current meter was also purchased for these mea-
surements with pressurization for a depth of at least 100 feet.
The new instrument also has a built-in compass to give current
direction, a pressure indicator to read depth, and a temperature
sensor (thermistor) to give the temperature (within $1^{o}C$) where

the current is measured. This unit, the Endeco Type 110, has been tested and appears to operate satisfactorily. For low currents, the direct reading of the meter is somewhat inaccurate since the current flow is not steady. A counter on the number of revolutions of the impeller blade for a given unit of time allows the current to be averaged. Accordingly, a counter unit has been built with a self-contained timer with intervals of ½, 1, and 2 minutes. The counter has a maximum rate of 1000 counts per minute, which can handle currents greater than four knots since the rotor unit develops pulses whose calibration is 3.56 pulses per second per knot.

Other instruments for the measurement of resistance, salinity, atmospheric conditions, etc., will be the same as for the Biscayne Bay tests.

D. Field Trips

During the period of this contract, from Oct. 15, 1974, to Oct. 15, 1975, tests were conducted as follows:

Biscayne Bay:	Oct. 24, 1974
	Apr. 1, 1975
	Apr. 15, 1975
	Sept. 4, 1975
Hutchinson Island:	May 1, 1975
	Sept. 18, 1975

During the previous contract year, tests were performed in Biscayne Bay on July 29, 1974, Aug. 21, 1974, and Sept. 24, 1974. The data from these tests were reported in the final report for the previous contract.

The Oct. 24 test was conducted in the central region of Biscayne Bay in conjunction with the NASA 6 aircraft and the data sheets are included in the appendix. The major measurements on this data were the direct temperatures, the currents, and the surface temperature using an infrared sensor. A comparison of the temperatures obtained from the ground truth and

the aircraft is given in the Remote Sensing Section, and the current information has been used in the Mathematical Model.

The Apr. 1, Apr. 15, and Sept. 4 field trips focused on temperature measurements in the thermal plume from the discharge canal of the Cutler Ridge Power Plant, a fossil fueled facility. Although this type of generating unit does not have as large an increase in water temperature as a nuclear power plant, it is nevertheless quite appreciable and very useful for testing the mathematical model. The morning measurements during the Apr. 15 trip were in the central region of Biscayne Bay and the data is compared with the aerial results in the Remote Sensing Section. A single measurement in the central region of the Bay was taken on Sept. 4 in the afternoon for calibration purposes. Data sheets for all these tests are given in the appendix.

Maps of the near field data location points for the Apr. 15 and Sept. 4 trips are given in Figs. II-1 and II-2. The time of measurement and surface temperatures are also provided to facilitate reference to the data sheets. The surface temperatures are indicated on the isotherms obtained from the aerial scanner so that measurement comparisons can be more easily noted. These latter diagrams are given in the Remote Sensing Section. Isotherms for the tests on these dates are given in Figs. II-3 and II-4 for the extension of the centerline of the discharge canal into the Bay. Here the isotherms are shown where the depth and the distance from the mouth are the coordinates. This is useful in indicating the dissipation of the hot water as it is discharged into the Bay and could be compared with that predicted from the model.

The Apr. 1 test was conducted primarily for familiarization with that region of the Bay, including navigation and techniques for boat handling in very shallow water. Many surface measurements were made along the canal centerline although the navigational readings of some of the points are apparently in error. A diagram of the surface temperature as a function of distance from the mouth is presented in Fig. II-5 and this could be of use in analyzing other data and examining

the results from the mathematical model. Similar diagrams
for the Apr. 15 and Sept. 4 data are illustrated in Figs.
II-6 and II-7.

A preliminary test was made on May 1, 1975, off the
coast of Hutchinson Island in the vicinity of the future site
of the power plant outlet. To determine the effect of the
outlet water, it would be advisable to measure conditions at
several different times of the year before the plant goes into
operation. The major purposes of this test were to find suit-
able landmarks for navigation and location, examine temperatures
at various depths, and record currents.

For navigation purposes, the landmarks which would
prove most useful are the power plant itself, a radio-television
tower north of the power plant, and a small concrete tower
south of the power plant. There is a dock near the outlet pipe
which could be used for location. The inlet pipe area is
marked by buoys and these would also be helpful. The system
of navigation recommended here should include the depth. For
example, the 18 ft. depth contour runs almost parallel to the
coast and the boat's depth sounder can place us exactly at a
given depth; other depths follow similar contours. The other
dimension can be determined by sightings on the landmarks
mentioned above.

A test of conditions during the latter part of summer
was conducted on Sept. 18, 1975, off the coast of Hutchinson
Island. Unfortunately, weather conditions were poor and the boat
trip had to be cancelled after the morning runs. Several data
locations were obtained, however, and the data sheets are in-
cluded in the appendix. Several interesting observations can
be made from the data. First, the salinity was constant verti-
cally and this is of value in deciding how much a factor
salinity is in the model. The currents at all depths flowed
approximately northward as is to be expected and this will be
of considerable value in the model studies. The vertical

temperature gradients were slight, but this is normal for
this area. All instruments functioned as expected and the
techniques for taking ground truth measurements were improved
as a result of the experience.

The nuclear power plant will not be in full operation
until early 1976, and present plans call for oceanographic
measurements to be made in this vicinity during the fall and
early winter of 1975. When the plant is in operation, simi-
lar measurements will be acquired and the effect of the plant
can be noted. More specific plans including test dates will
be determined at a later time when availability of the aircraft
and other factors can be taken into account.

Data Point	Time	Surface °C	Temp. °F
A	1:25 PM	35.9	96.6
B	2:00 PM	34.8	94.6
C	2:10 PM	34.4	93.9
D	2:25 PM	32.5	90.5
E	2:40 PM	31.9	89.4
F	3:15 PM	29.7	85.5
G	3:05 PM	31.1	88.0
H	1:30 PM	34.4	93.9
I	3:00 PM	31.7	89.1

Hi Tide at Kings Bay: 1:00 PM

Plane Overhead at 1:00, 1:45, 2:35 PM.

N

Water Tower

Discharge Canal →

Kings Point

Inlet Channel

Chicken Key

Cupola

240 m.

DATA LOCATIONS - APRIL 15, 1975

Fig. II-1

Data Point	Time	Surface Temperature °C	°F
A	8:25 AM	38.3	100.9
B	11:40 AM	34.4	93.9
C	12:00 Noon	32.8	91.0
D	1:00 PM	33.0	91.4
E	9:55 AM	35.6	96.1
F	1:22 PM	33.8	92.8
G	1:30 PM	32.6	90.7
H	1:40 PM	31.9	89.4
I	1:09 PM	34.1	93.4
J	10:16 AM	35.0	95.0
K	9:42 AM	35.9	96.6
L	10:37 AM	31.6	88.9
M	1:54 PM	30.9	87.6

Hi Tide at Kings Bay: 8:54 AM

Plane Overhead at 9:11 AM, 9:55 AM, 1:10 PM, 1:47 PM

240 m.

Water Tower

Discharge Canal

Kings Point

Inlet Channel

Chicken Key

Cupola

-15-
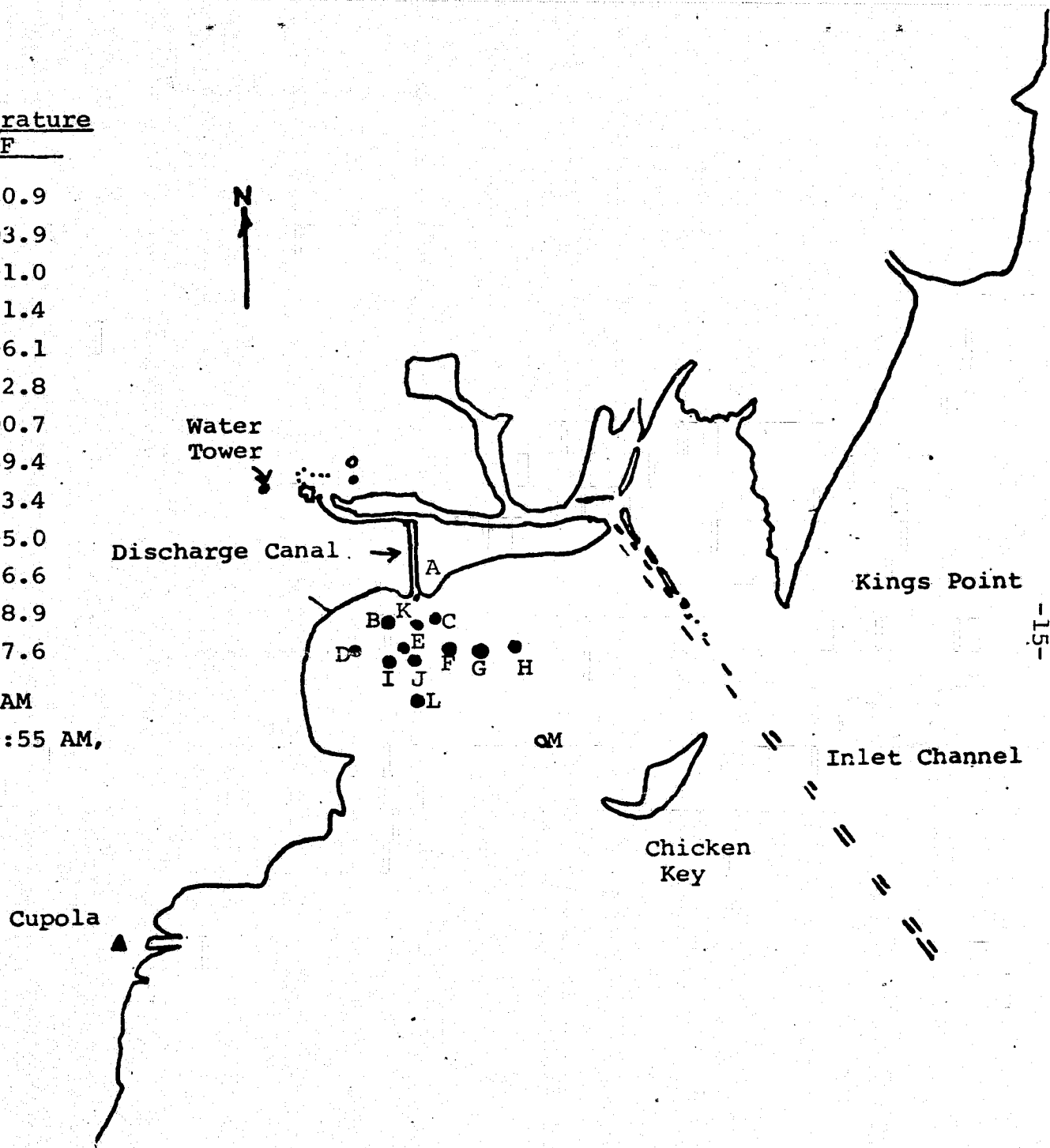
DATA LOCATIONS - SEPTEMBER 4, 1975

Fig. II-2

APRIL 15, 1975

ISOTHERMS OFF CUTLER RIDGE DISCHARGE CANAL IN BAY
ALONG CANAL CENTERLINE

Fig. II-3

Distance from Mouth of Discharge Canal, Meters

Depth – ft.

Temperature in °C

SEPTEMBER 4, 1975
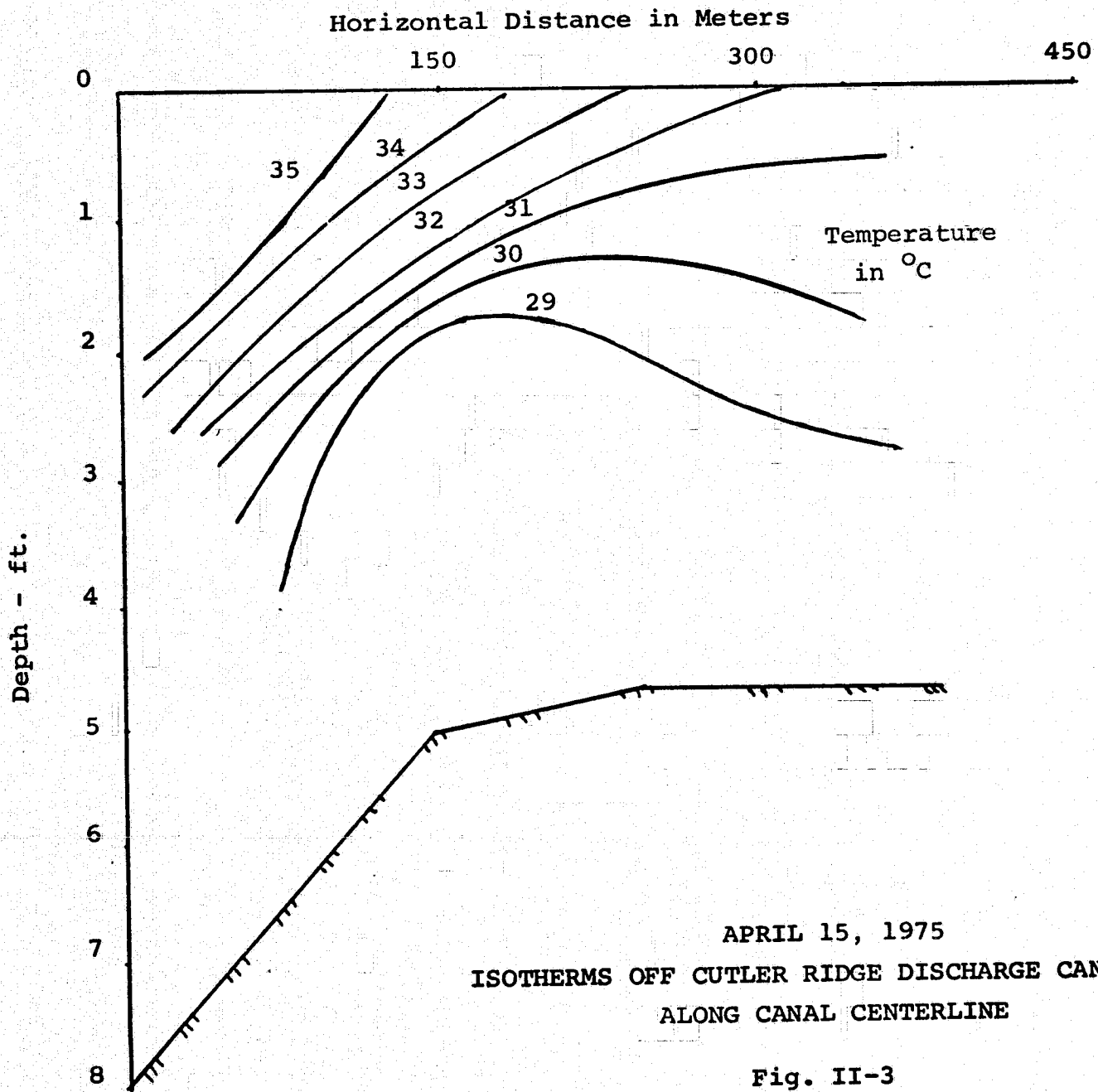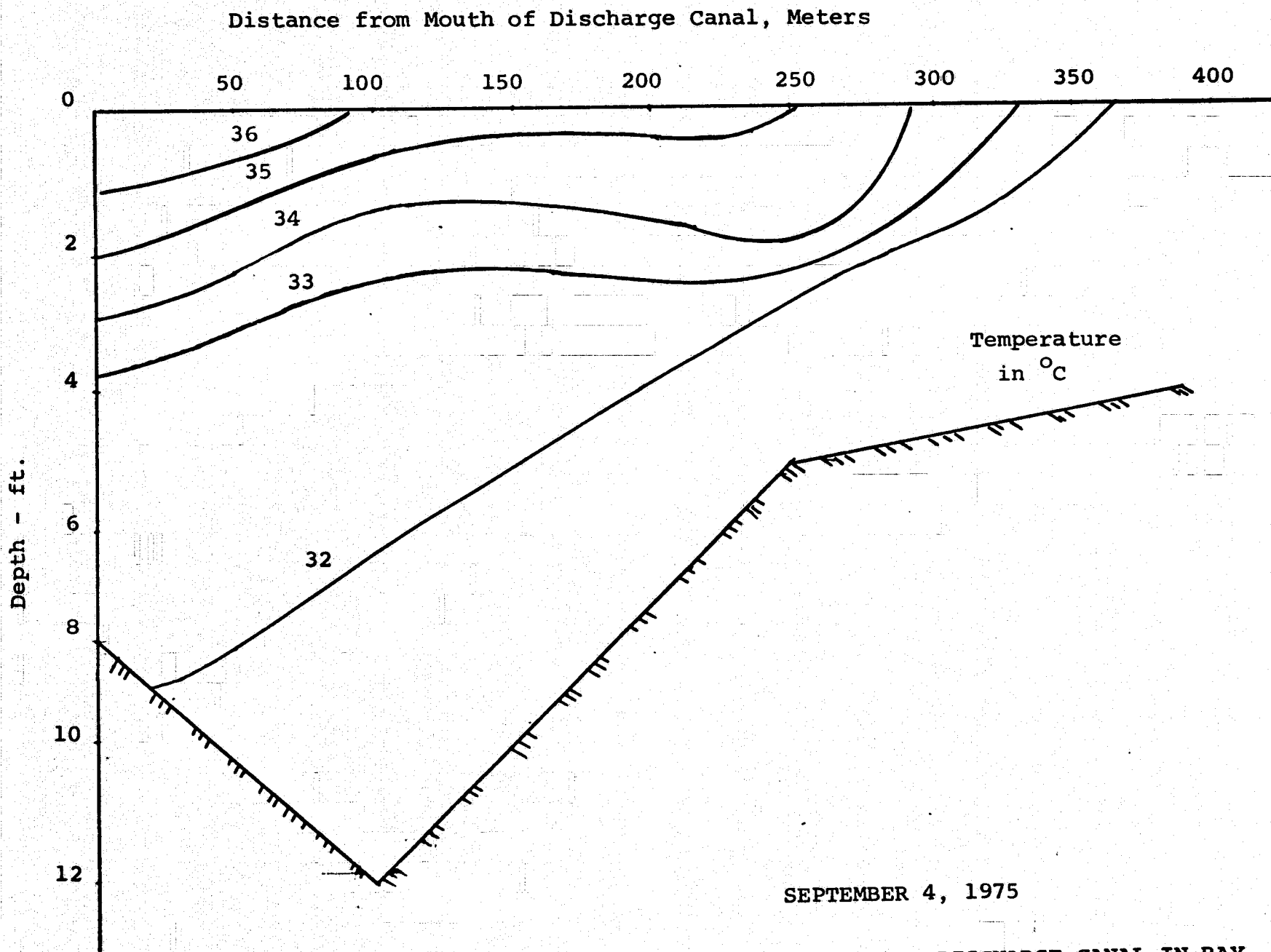
Fig. II-4

ISOTHERMS OFF CUTLER RIDGE DISCHARGE CANAL IN BAY
ALONG CANAL CENTERLINE
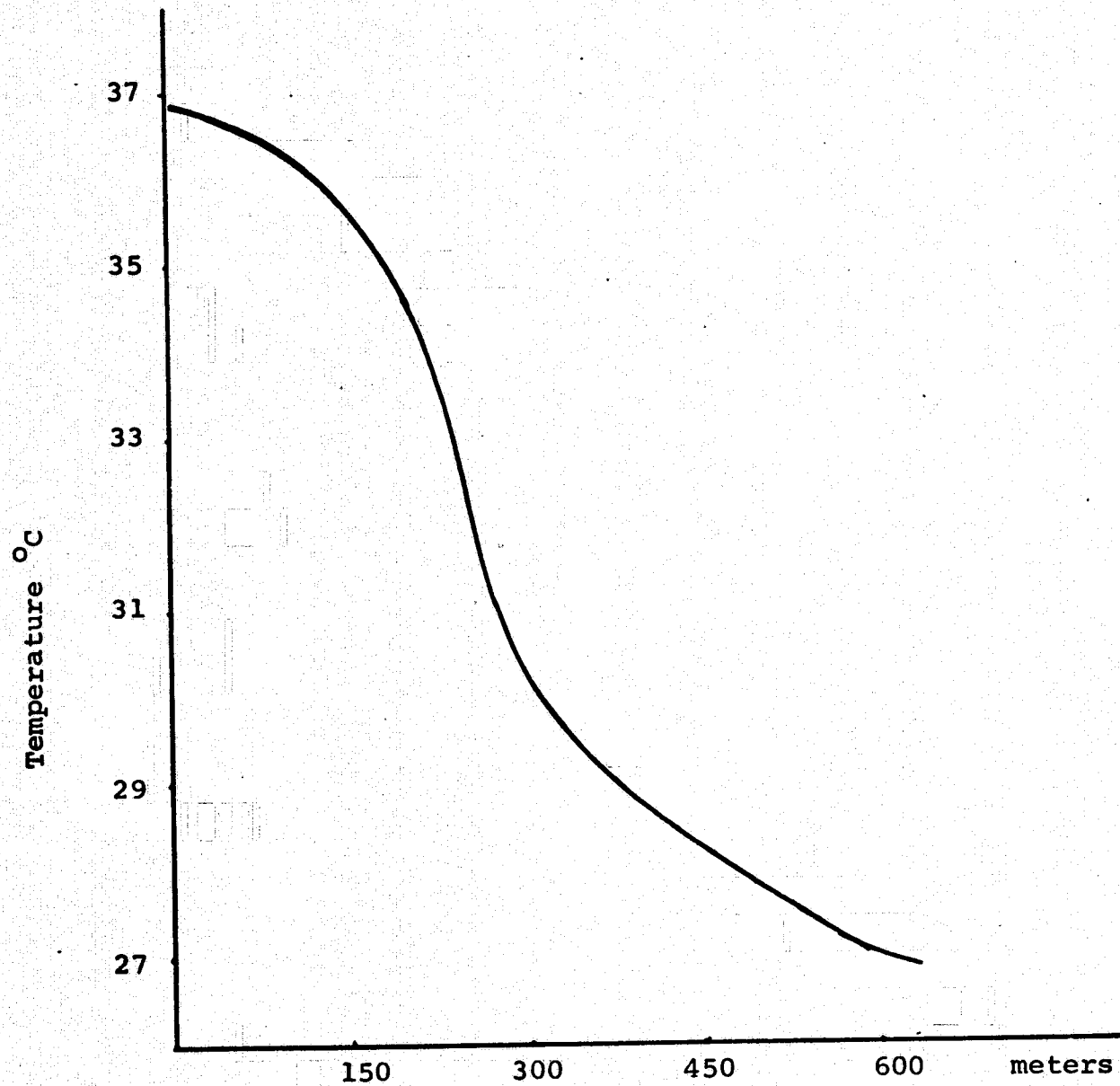
Fig. II-5

SURFACE TEMPERATURE VS DISTANCE FROM MOUTH OF
DISCHARGE CANAL ALONG CENTERLINE
APRIL 1, 1975
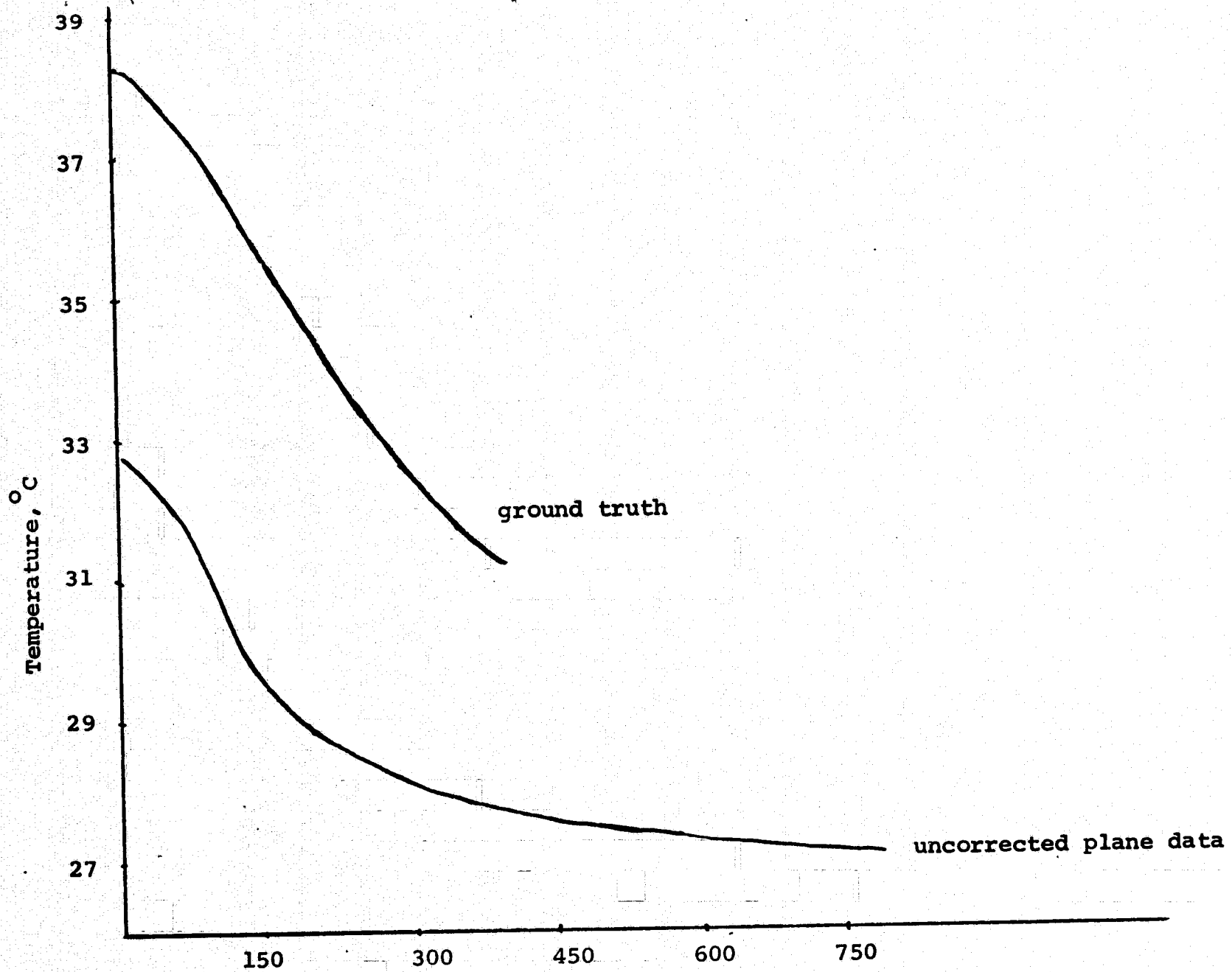
SURFACE TEMPERATURE VS. DISTANCE FROM MOUTH
OF DISCHARGE CANAL ALONG CENTERLINE
SEPT. 4, 1975
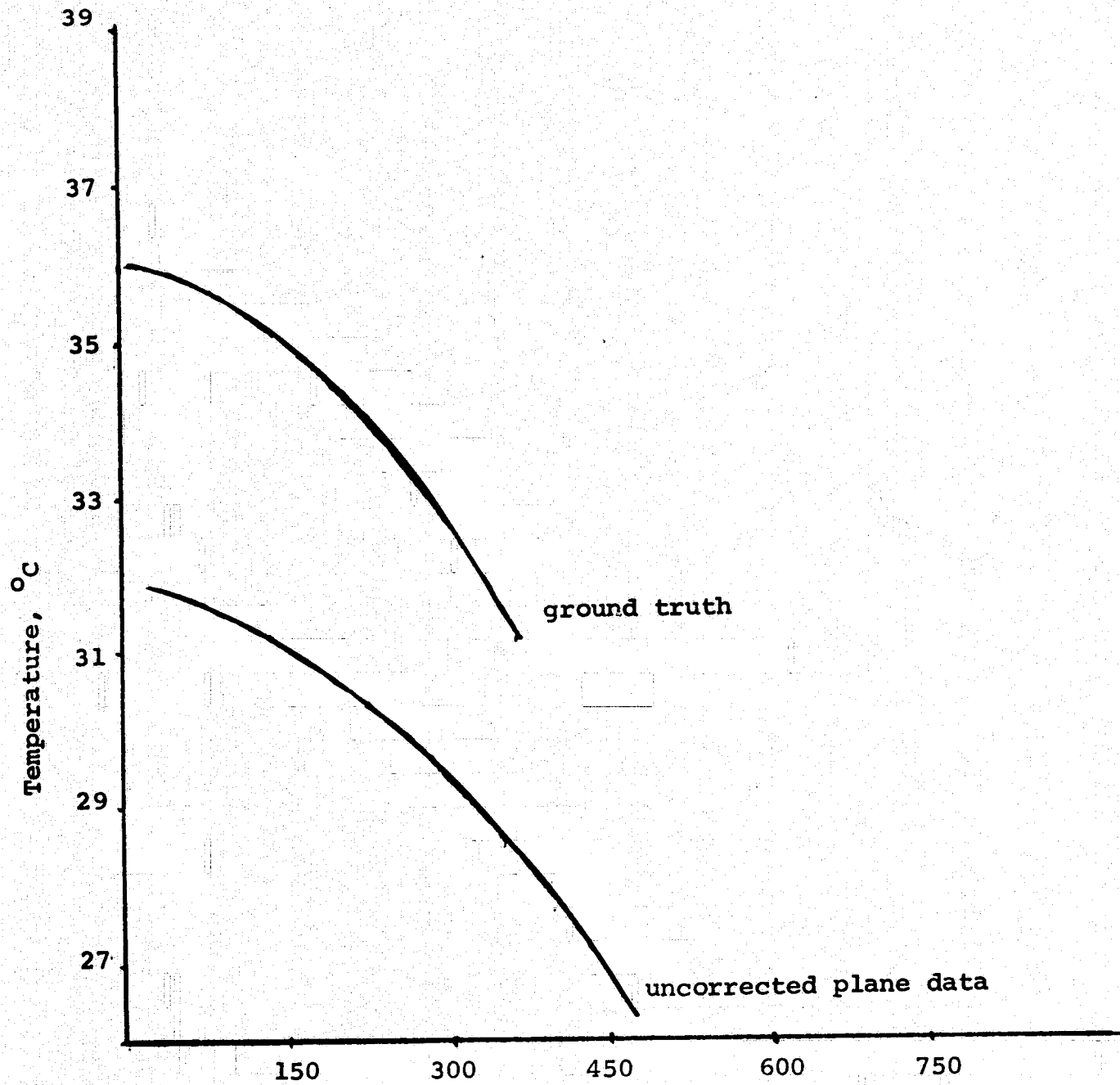
Fig. II-6

SURFACE TEMPERATURE VS. DISTANCE FROM MOUTH
OF DISCHARGE CANAL ALONG CENTERLINE

Fig. II-7   APRIL 15, 1975

III. REMOTE SENSING WATER SURFACE TEMPERATURE

Four thermal IR remote sensing experiments have been
conducted in Biscayne Bay using NOAA-3 and NOAA-4 polar-
orbit satellites and the Kennedy Space Center NASA-6 Beech-
craft C-45H aircraft. These were conducted on July 29, 1974,
October 24, 1974, April 15, 1975, and September 4, 1975.
Isotherms depicting a warm water plume from Cutler Ridge power
plant are presented for July 29, 1974 and April 15, 1975 from
the 8-14 micron thermal IR channel of the Daedalus multispectral
scanner aboard the NASA/KSC aircraft. Similar aircraft data
are being processed for September 4, 1975. A weak isotherm
pattern was mapped in Biscayne Bay on October 24, 1974 because
the Cutler Ridge power plant was not operating and so did not
produce a plume.

Digital maps of remotely sensed temperatures for Biscayne
Bay and surrounding areas from NOAA-3 and NOAA-4 satellites
using 10.5 to 12.5-micron IR sensors are presented for October
24, 1974 and April 15, 1975. Similar data are being processed
for September 4, 1975. On July 29, 1974, extensive cloud cover
prevented the NOAA-3 satellite-borne sensors from seeing Bis-
cayne Bay at the time of the morning overpass. However, the
aircraft was able to obtain data by flying beneath the cloud
base.

Unfortunately, the spatial resolution of thermal IR
measuring systems used in the present generation of satellites
does not provide as much detail as is desirable for this project,
although the spatial resolution of these thermal sensors is
improving with each new generation of satellites. Clouds may
prevent satellite-borne sensors from seeing the ocean surface
on some occasions but the frequency of observations is still
better than that obtainable by other means for similar costs.
It is believed that, ultimately, satellites can be used not only

for global ocean surface temperature mapping but should be able
to provide the accurate, high-resolution water temperature data
needed for monitoring thermal pollution from power plant dis-
charges, detecting cold water upwelling and springs, and for
model studies.

A. Corrections to Satellite and Aircraft Measurements
    of Sea Surface Temperature

Corrections must be applied to the satellite and air-
craft measurements in order to obtain the real sea surface
temperatures. These corrections are principally:

1) departures of the sea from a true blackbody
    condition, and

2) effects of the atmosphere through which the
    electromagnetic waves pass (Hiser et al.)[1].

Investigations have shown that the correction for
departure from a true blackbody is small [2]. It is probably
within the limits of instrumentation error for our purposes
(less than $0.5^{\circ}C$) and certainly much less than the atmospheric
effects. A radiometer measures total radiance, R, which is the
flux of radiation per unit solid angle per unit wavelength per
unit area. The total radiance is composed of an emitted and a
reflected component, namely:

$$R = EB + rN \qquad\qquad (3-1)$$

Here R is the total radiance of a surface, B is the radiance of
a blackbody at the surface temperature, E and r are the emittance
and reflectance of the surface, respectively, and N is the total
radiance falling on the surface (the sky radiance). The re-
flectance term in equation 3-1 is quite small for the ocean sur-
face except when a scanning radiometer looks directly at a small
sun glint spot on a relatively smooth sea. Therefore, the
radiance R measured by a radiometer would be nearly that of a
blackbody at the sea temperature (EB) if there were no trans-
mission losses through the atmosphere.

The infrared region of the spectrum from 8 to 14 microns, which is suitable for measuring terrestial temperatures of the order of $300^{O}K$, is subject to some absorption losses by gases and water vapor in the atmosphere (Fig. III-1).
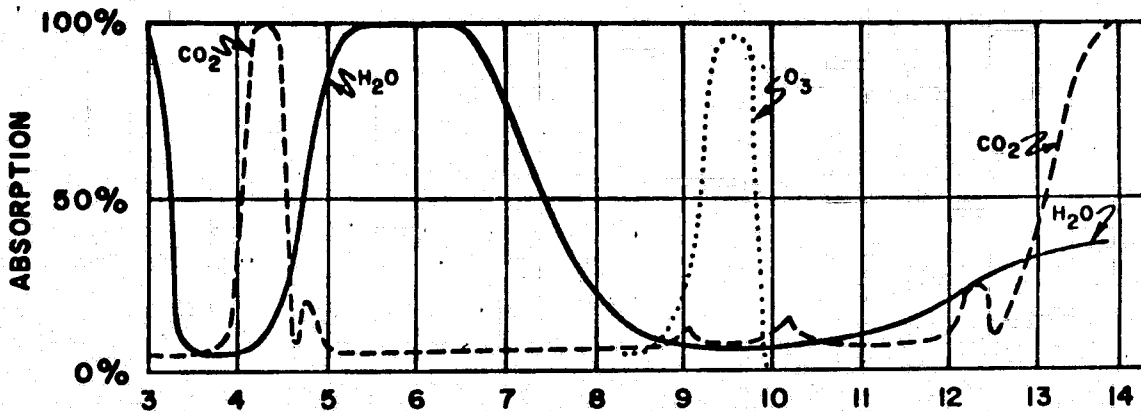

Fig. III-1. Absorption curves of H_2O, CO_2, and O_3, between 3 and 14μ.

Ozone (O_3) has a strong absorption band between 9 and 10 microns; however, it is primarily in the upper atmosphere and does not affect data gathered by aircraft. The VHRR on the NOAA satellites operates in the 10.5 to 12.5-micron region which is outside this ozone absorption band.

Water vapor is the major variable in this thermal IR region of the spectrum with a minor contribution by CO_2. If N_s is the radiance of the ocean surface observed at zero altitude and N is the radiance as observed in a narrow spectral region from a satellite, the correction to the satellite observed radiance for the intervening air column is given by:

$$N_s - N = - \int_O^U (N_s - B_a) \frac{d\tau}{du} du \qquad (3-2)$$

Here B_a is the radiance of a blackbody at air temperature, $\tau(u)$ is the transmittance of a mass of absorbing gas u measured

downward from the sensor, and U is the absorbing mass (mostly water vapor) for the entire column between sensor and surface.

It is possible to calculate the amount of atmospheric absorption if the distribution of absorbing gases in the atmosphere is known. The problem is complicated because the absorption varies with pressure and temperature in a non-linear fashion. The calculations utilize laboratory measurements of absorption by atmospheric gases. However, because environmental conditions in the laboratory experiments are different from those in the atmosphere, theory must be applied. Computations of the outgoing radiation for 106 model atmospheres have been made by Wark et al. [3]. For clear sky conditions, water vapor was the primary variable. A correction for an average ozone distribution was made; the error due to different ozone distributions is likely to be relatively small.

The results for clear sky conditions and nadir angles of 0° and 45° are shown in Fig. III-2 [4]. In this figure, the ordinate is the amount of precipitable water in the atmosphere. Horizontal lines indicate "average" conditions (W=2.25 cm) and "moist" conditions (W=3.9 cm). The nearly vertical lines are labeled T_E, the equivalent blackbody radiation as measured by the satellite. Thus, for a 0° nadir angle with $T_E = 290^{\circ}$, the correction to be added to obtain the temperature of the radiating surface is $6.8^{\circ}C$ for average humidity and $9^{\circ}C$ for moist conditions; at a 45° angle the corrections are 9.5° and $12^{\circ}C$, respectively.

The precipitable water (W) for application in Fig. III-2 can be obtained from radiosonde data in many places. Radiosonde balloons are launched daily throughout the world at 00 and 12 Greenwich Mean Time (GMT or Z). They obtain pressure, temperature, and relative humidity data to altitudes in excess of 50,000 ft. Most of the atmospheric moisture is contained in the troposphere below 30,000 ft. Therefore, these soundings can be used to calculate W for the atmospheric column.
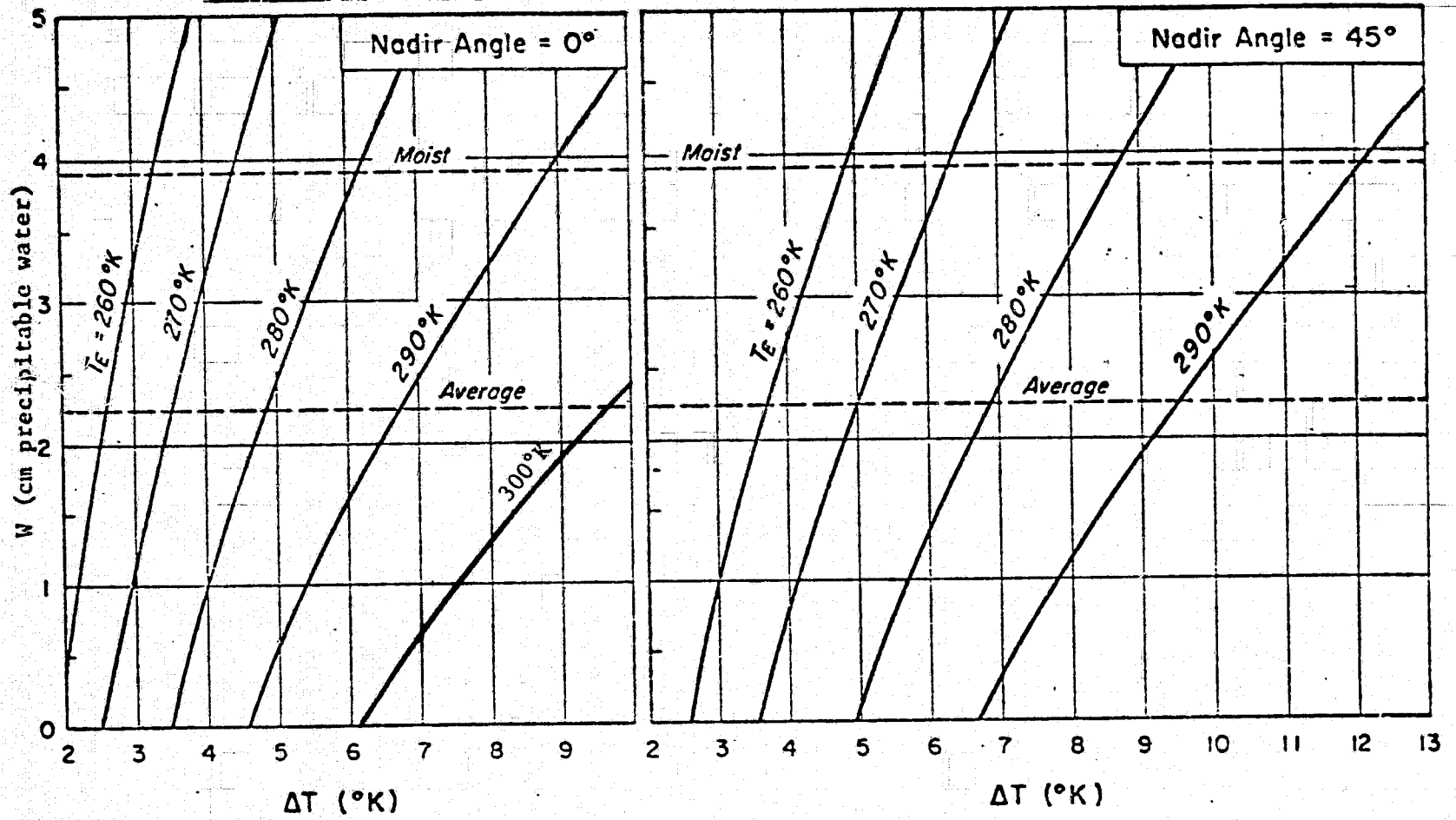
Fig. III-2. Clear-Sky Temperature Corrections

If the sounding is plotted on a Pseudo-Adiabatic chart, the mean vapor pressure (e) in millibars can be determined graphically for atmospheric layers between plotted points on the sounding. The water content for each of these layers can be calculated by using the equation:

$$W \text{ cm} = \frac{0.622}{g} \, e \, \ln P_2/P_1 \qquad (3-3)$$

where g is the acceleration of gravity, P_1 is the pressure at the top of the layer in millibars and P_2 is the pressure at the bottom in millibars [5]. The total W is then obtained by summing these values for all layers of the sounding. Table III-1 gives the precipitable water computed from the Miami airport sounding at 1200Z (0800 EDT) on July 29, 1974. The right hand column gives the accumulated total W from the surface upward. The highest value of W in the top right corner is used to enter the diagram in Fig. III-2. Table III-1 also provides data for lower altitudes that can be used to apply corrections to IR temperature measurements made from aircraft.

B. Aircraft Data, July 29, 1974

Fig. III-3 shows the surface isotherm pattern for a well developed thermal plume in Biscayne Bay from the Cutler Ridge Power Plant at 1230 EDT on July 29, 1974. These isotherms were constructed from the calibrated gray-scale, 70-mm film transparency that was prepared from the magnetic tape used aboard the KSC NASA-6 aircraft to store the analog readout of the Daedalus multispectral scanner. Other data were taken at 0930, 1030, and 1130 EDT, but the pattern at 1230 was most evident because the plume had time to develop as the power plant output increased and the discharge temperature reached a maximum. The aircraft flew at 1500 ft. altitude and made twelve west to east data passes across Biscayne Bay between 0800 EDT (1200Z) and 1300 EDT (1700Z). No ground truth data are available within the plume at the time the aircraft pass was flown.

TABLE III-1. PRECIPITABLE WATER AT MIAMI, 1200 Z (0800 EDT),
July 29, 1974

Approximate Altitude Feet	Layers P_1/P_2	Mean e for Layer	Cumulative W cm for Layers
23,600	400		
		1.38	5.376
21,400	438		
	438		
		2.25	5.299
18,300	500		
	500		
		3.1	5.113
17,400	518		
	518		
		3.7	5.045
16,000	550		
	550		
		4.4	4.907
14,600	580		
	580		
		5.1	4.762
13,800	598		
	598		
		6.2	4.665
11,400	658		
	658		
		.7.0	4.296
9,900	700		
	700		
		9.8	4.027
7,100	780		
	780		
		10.6	3.367
6,700	790		
	790		
		12.4	3.283
4,800	850		
	850		
		17.8	2.718
3,300	895		
	895		
		22.8	2.1479
2,000	940		
	940		
		29.0	1.4516
700	985		
	985		
		28.0	.6081
Surface	1020		

Surface Isotherms
Cutler Ridge Power Plant
1230 EDT, Flt. Alt. 1500 Ft.
July 29, 1974

Ground Truth Measurement, 2.5 NM (4,630m)
South of Canal Mouth at 1200 EDT
was 34.1°C = 93.4°F

240 m.

Water
Tower

Discharge Canal →

79

81

79

91

89

87

85

83

79

81

Cupola

Chicken
Key

Kings Point

Inlet Channel

-28-
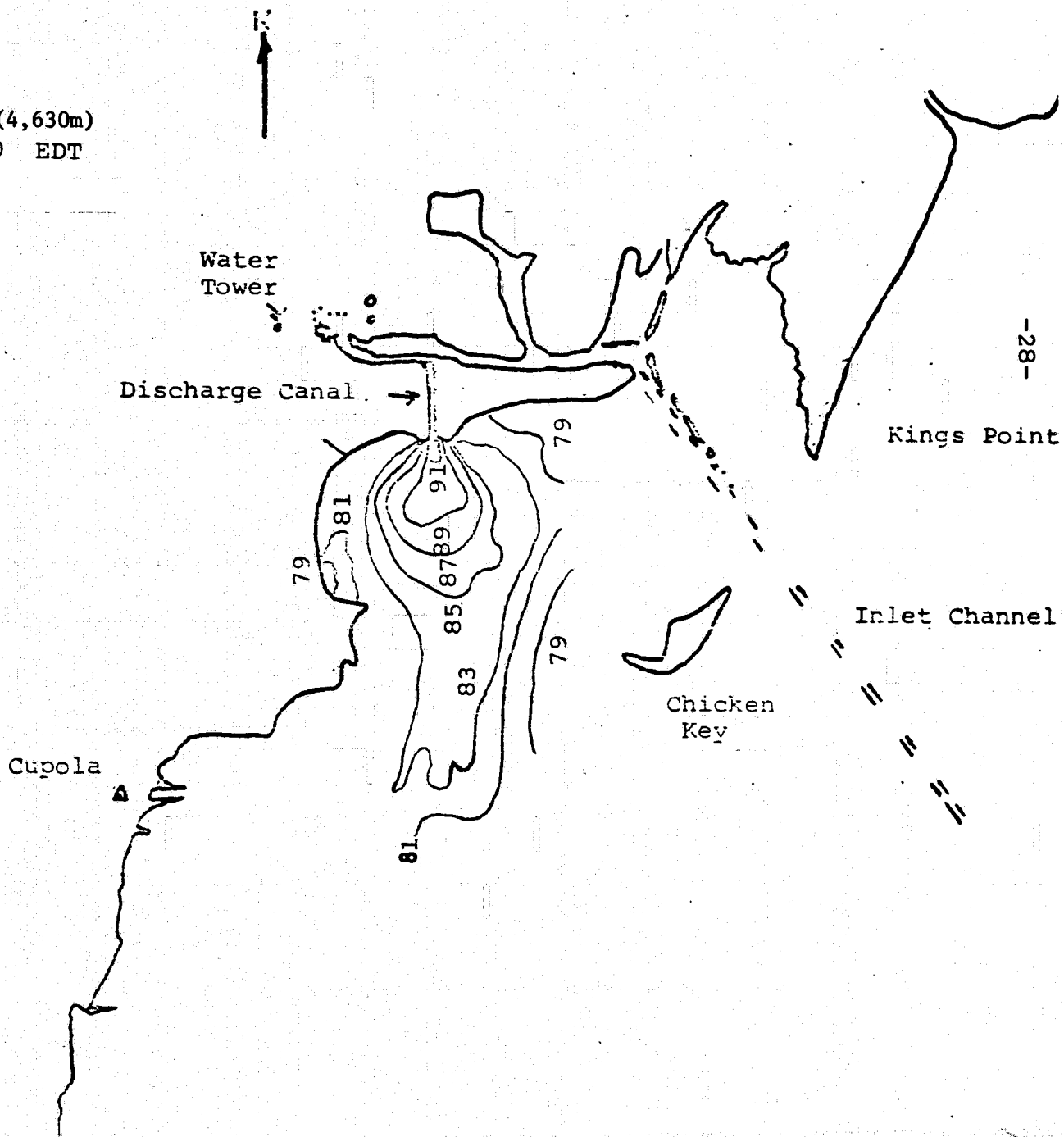
Fig. III-3

C. Satellite Data, October 24, 1974

Temperature measurements of the earth's surface made by IR from satellites must be corrected for water vapor absorption in the atmosphere. The Miami radiosonde data for 0800 EDT on October 24, 1974 has been used to determine the precipitable water in the atmosphere for this study in Biscayne Bay (see Table III-2). The diagram in Fig. III-2 is used to determine the correction (ΔT) to be added to the satellite measurements of sea surface temperature (T_E) in the presence of a given amount of precipitable water (W). This diagram gives values for use near the satellite subpoint (Nadir Angle = 0°) and at 45° from the subpoint (Nadir Angle = 45°). Linear interpolations for intermediate angles are within the limits of accuracy of the measurements.

Figs. III-4 and III-5 are digitized and contoured temperature maps prepared by computer from the NOAA-3 VHRR (10.5 to 12.5 microns) IR data in the vicinity of Miami on October 24, 1974. Fig. III-4 is a 1-km grid based upon the minimum resolution of the satellite and Fig. 3-5 is a 2-km grid with space-averaged data plotted at each grid point. The coldest areas (stippled) are radiation from clouds and can be ignored for our purposes. The satellite-measured isotherms in Fig. III-4 are 20^OC (solid) and 18^OC (Dashed). In Fig. III-5 they are 20^OC (solid) and 24^OC (dashed). The direction of north is shown on each of these illustrations because the NOAA-3 satellite track is inclined 16° from the meridians.

The data in both of these figures are uncorrected for water vapor absorption. The Miami radiosonde at 1200Z (0800 EDT) on October 24, 1974, which was less than two hours before the satellite pass, gave a total liquid water content of 4.09 cm (see Table III-2). Since the satellite measured surface temperatures of interest are near 290^OK and the Nadir Angle is near 0°, the correction to be added is 9^OC (see

Table III-2. Precipitable Water at Miami,
1200 Z (0800 EDT), October 24, 1974.

Approximate Altitude Feet	Layers P_1/P_2	Mean e for Layer	Cumulative W cm for Layers
23,600	400	0.16	4.09
18,300	500		
	500	0.68	4.05
16,900	530		
	530	0.7	4.01
9,900	700		
	700	0.9	3.82
8,100	750		
	750	3.1	3.76
7,800	760		
	760	8.5	3.71
6,400	795		
	795	9.8	3.33
4,800	850		
	850	12.6	2.68
3,000	910		
	910	15.8	1.82
200	1000		
	1000	16.5	0.33
Surface	1020		
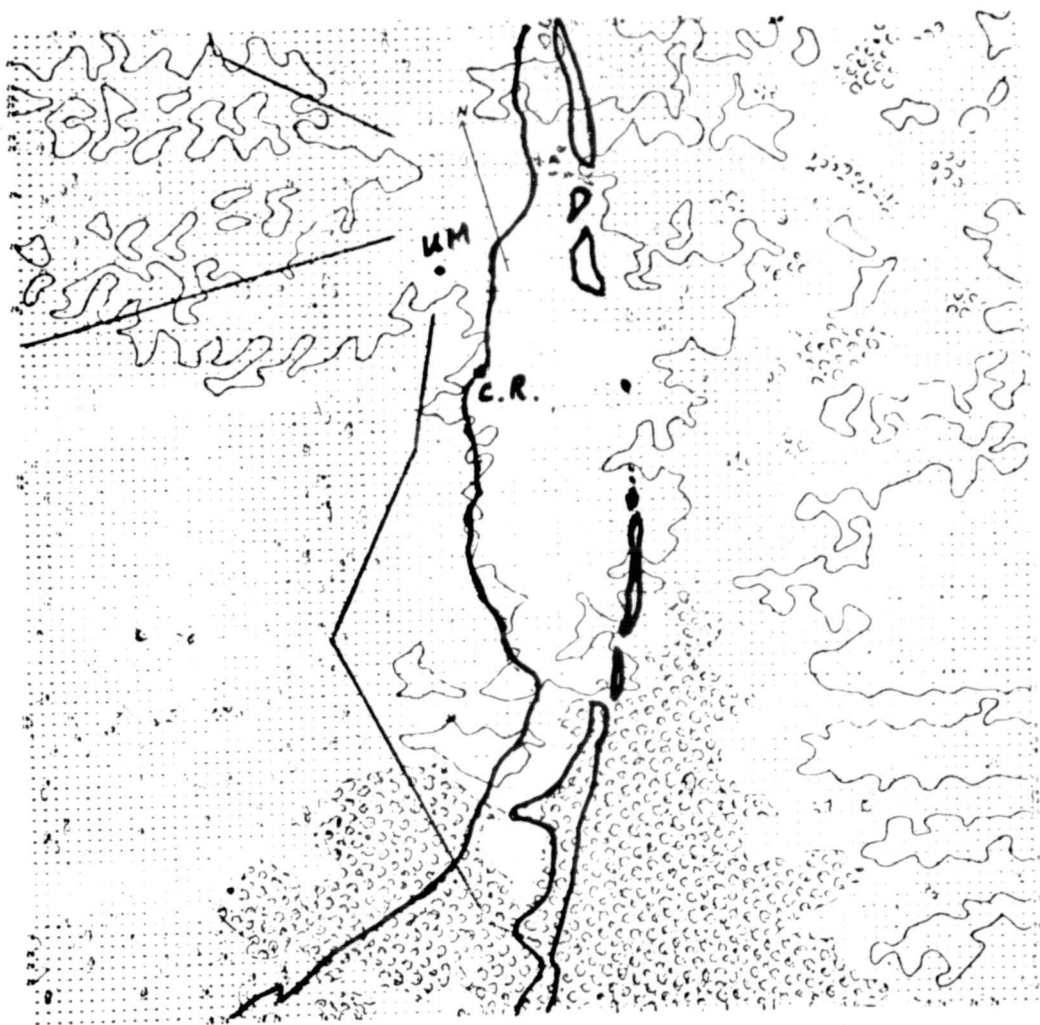
Fig. III-4.   Digitized IR Temperatures from NOAA-3
Satellite, October 24, 1974, 1342 Z
(0942 EDT), 1-km Grid Squares.
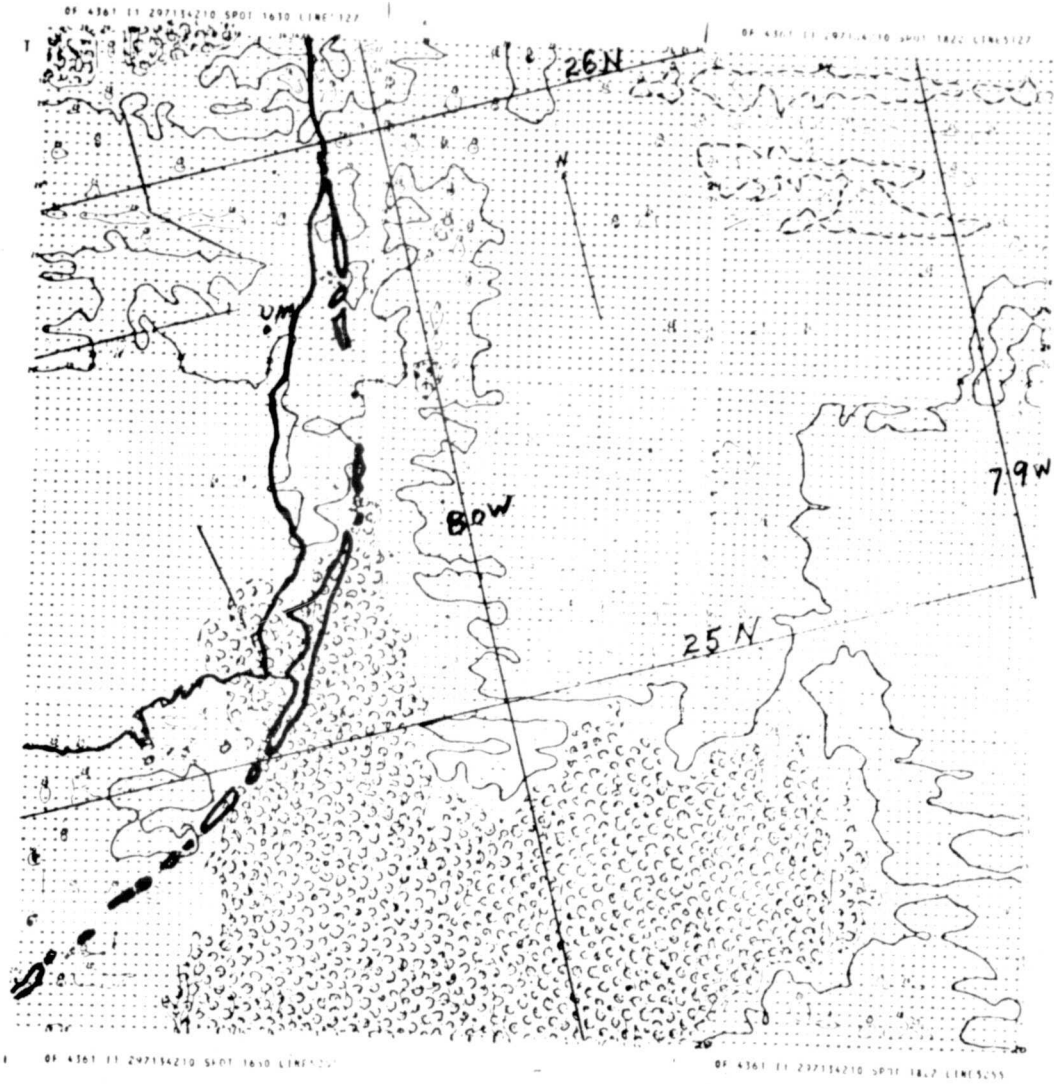
Fig. III-5. Digitized IR Temperatures from NOAA-3
Satellite, October 24, 1974, 1342 Z
(0942 EDT), 2 x 3 km Grid Squares.

Fig. III-2)   In Figs. III-4 and III-5, the solid line is the 20°C indicated (29°C water-vapor corrected) isotherm, and the dashed isotherm in Fig. III-5 is 24°C indicated or 33°C corrected.   The temperature resolution of the VHRR sensor is approximately $\pm$0.5°C for a 300°K scene.   This can cause the computer to produce some small contoured areas that may not be significant.   The area of these is usually one resolution cell of the sensor and they are indicated to be only one degree colder or warmer than their surroundings.   Most of these small contoured areas are not visible in the reproduction of Fig. III-4 and the computer averaging in Fig. III-5 eliminates them.

These computer printouts were prepared by the National Environmental Satellite Service of NOAA in Washington, D. C.   Because of the great enlargement of a small area for mesoscale analysis, a latitude and longitude grid coordinate system was not available in the program for these printouts. They must be located geographically by use of photographs made from the visual band of the multi-spectral scanner aboard the satellite.   Such photographs were provided along with the digital printouts for this purpose.   A best-fit map of Biscayne Bay has been sketched on Fig. III-4, and a map of the southeast Florida coastal area with some latitude and longitude coordinates has been sketched on Fig. III-5.

Both of these illustrations show slightly warmer water in Biscayne Bay than on the continental shelf, and Fig. III-5 shows warmer water in the Gulf Stream than on the shelf. The warmest water is shown in Fig. III-5 in the shallows north of Bimini and east of the Gulf Stream.   The metropolitan area of Miami is shown slightly warmer than the glades and farm land to the south and southwest of the city.   An interesting feature of these illustrations is the cool tongue of water extending into the central part of Biscayne Bay from the shelf area just north of Elliot Key.   Low tide at Government Cut at the south end of Miami Beach occurred at 0950 EDT on this date.   Thus, tidal currents should have been near a minimum at the time of

the satellite pass. More observations are needed to determine the significance of this feature.

D.   Aircraft and Satellite Data, April 15, 1975

Fig. III-6 shows the thermal IR data gathered along flight paths 10 through 16 on the morning of April 15, 1975 by the KSC NASA-6 aircraft. Clouds kept the aircraft at lower than the optimum altitudes for good aerial coverage by the thermal scanner, which has a 76-degree field of view normal to the flight path. Boat measurements of ground truth temperature data were taken at points A, B, C, and D. The isotherms shown are uncorrected for atmospheric water vapor absorption. Since the theoretical corrections for water vapor are too large in some instances, the boat measurements are used to correct the aircraft data before final analysis. This figure illustrates that the aircraft thermal IR data are not synoptic in time and that the aerial coverage is incomplete because of cloud limitations on flight altitude.

Fig. III-7 shows the thermal plume from Cutler Ridge Power Plant at 1546-1547 EDT as measured with the multispectral scanner (8-14 microns) from 2,000 ft. on flight line number 16. The highest indicated temperature in the plume is $89^{\circ}F$. The boat measurement at point A on the 83° isotherm, 31 minutes before flight time, indicates a $+2.5^{\circ}F$ correction to be applied to the IR data. This assumes steady state conditions in the plume for the 30-minute period. Fig. III-2, using 2.07 cm of precipitable water for the flight altitude of 2,000 ft. from Table III-3, gives a much larger correction, which is probably excessive. Therefore, the $+2.5^{\circ}F$ ground truth correction was applied to the aircraft data and the adjusted isotherm values are shown in parentheses.

An interesting feature of this plume can be noted by

BISCAYNE BAY
AND
CARD SOUND
FLORIDA

2.3 km

N

12

KEY
BISCAYNE

CUTLER RIDGE
POWER PLANT

14

15

16

74

75

76

76

74

75

76

74

76

75

75

75

75

75

75

75

75

75

75

75

76

75

10

76

76

TURKEY POINT

75

75

75

75

13

75

75

76

75

75

76

76

76

76

76

ELLIOT KEY

KEY LARGO

11

	Ground Truth Time and Surface Temp. °F	Most Synchro- nous Air- craft Pass Time		Alt. (1000 Ft.)
A.	9:30 AM 78°F	16	0911	2.5
		11	0937	1.0
B.	10:20 AM 78°F	12	10:13	1.0
C.	11:00 AM 78.3°F	13	10:03	1.0
D.	11:30 AM 79°F	14	12:10	2.0
		10	9:51	1.0
		15	12:27	2.0
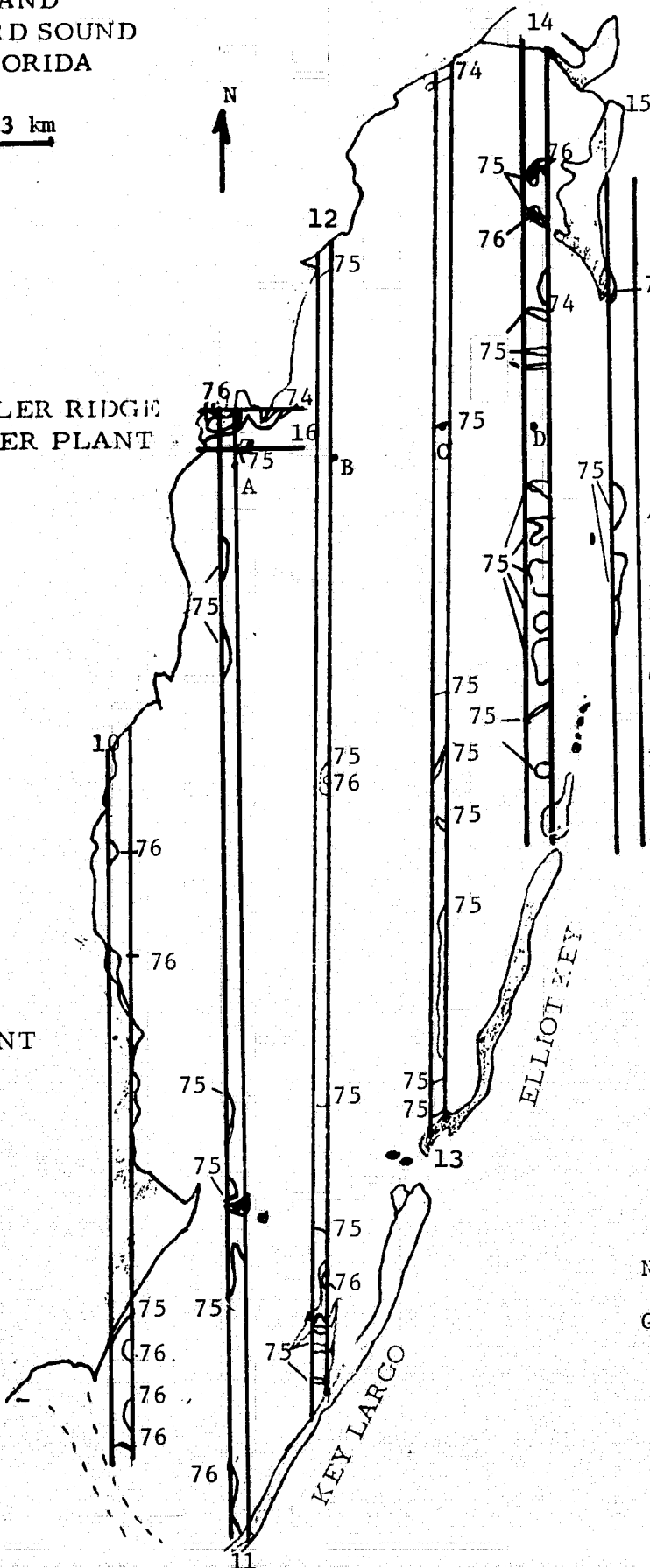
Fig. III-6

SURFACE COVERAGE OF
NASA-6 IR SCANNER DATA
SHOWING LOCATIONS OF
GROUND TRUTH DATA POINTS

APRIL 15, 1975
(MORNING)

Surface Isotherms
Cutler Ridge Power Plant
1546 – 1547 EDT   Flt. Alt. 2000 Ft.
April 15, 1975

Ground Truth (A)
at 1515 EDT
$29.7^{\circ}C = 85.5^{\circ}F$

Isotherm values in parenthesis
have been adjusted +2.5°F to
match ground truth at point A.

Fig. III-7

240 m.

Water
Tower

Discharge Canal
(91.5)
(87.5)
85
89
(83.5)
81
83
(85.5)
79(81.5)
79(81.5)
79(81.5)

Kings Point

Inlet Channel

Chicken
Key

Cupola

-36-
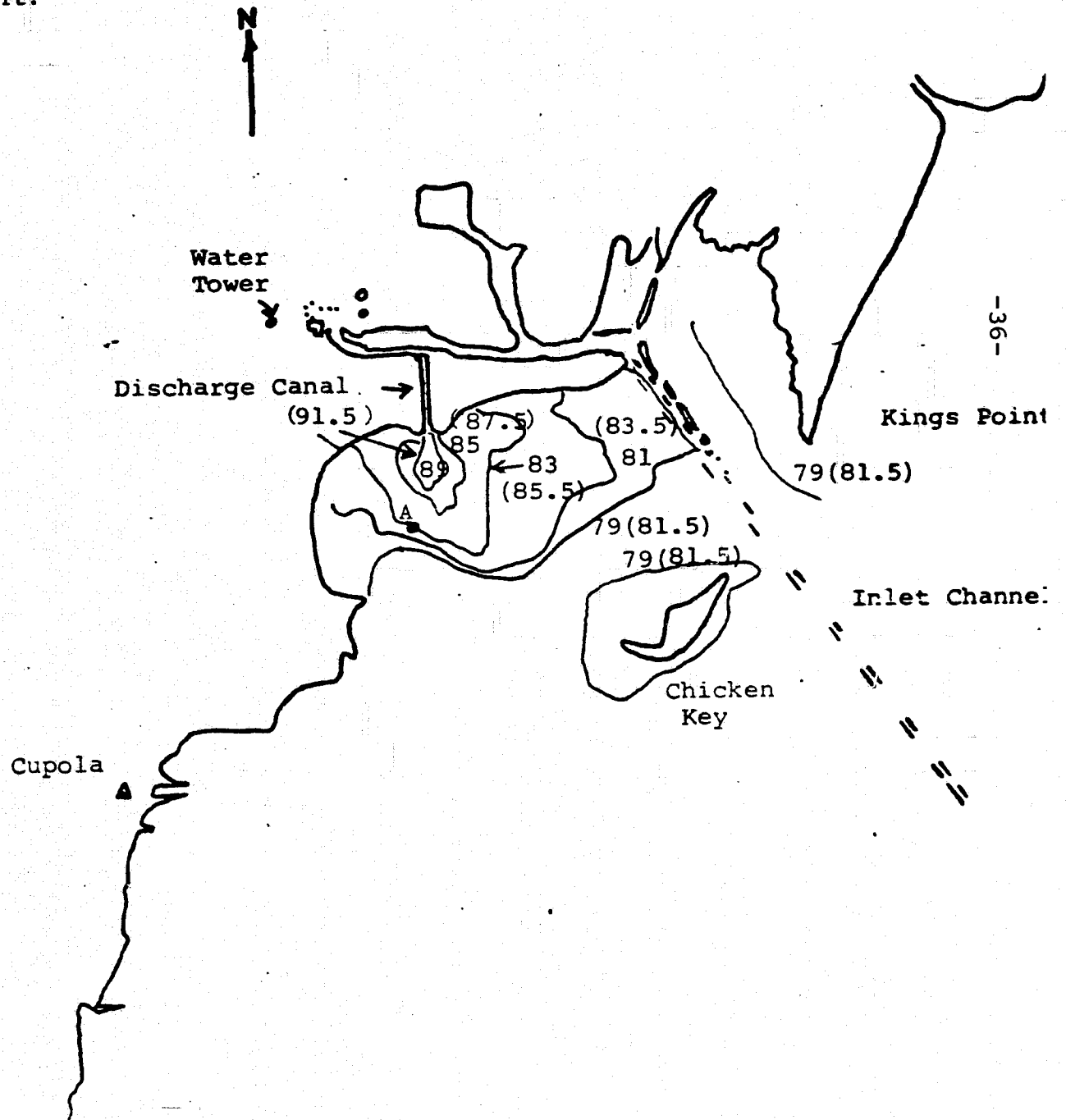
Table III-3. Precipitable Water at Miami,
1200 Z (0800 EDT), April 15, 1975.

Approximate Altitude Feet	Layers P_1/P_2	Mean e for Layer	Cumulative W cm for Layers
23,600	400		
		0.64	5.15
22,200	425		
	425		
		0.95	5.11
20,300	460		
	460		
		1.22	5.03
19,000	485		
	485		
		0.56	4.97
16,600	535		
	535		
		0.60	4.91
9,800	700		
	700		
		1.22	4.75
9,300	715		
	715		
		1.92	4.73
6,900	785		
	785		
		5.6	4.55
6,200	806		
	806		
		11.5	4.40
4,800	850		
	850		
		13.9	3.79
4,500	860		
	860		
		16.8	3.63
2,600	920		
	920		
		19.5	2.49
2,000	940		
	940		
		24.4	2.07
200	1000		
	1000		
		28.5	0.56
Surface	1020		

comparing it with Fig. III-3 for July 29, 1974. The plume on July 29 was elongated north-south while the one on April 15 has its major axis oriented east-west. The difference in wind and tide conditions are believed to be responsible for this. On July 29, 1974, low tide occurred at the Cutler Ridge Plant at approximately 1300 EDT while on April 15, 1975 high tide occurred there at approximately 1230 EDT. The outgoing tide prior to the image on July 29 probably contributed to expansion of the plume away from the shore, while the incoming tide on April 15 contributed to lateral spreading along the coast. Another major contributing factor may have been the surface wind conditions. Around noon on April 15, the winds were from the south at 13-16 knots blowing against the discharge plume. On July 29, 1974, they were much lighter and more variable, south-southeast at 6 knots at noon and west-southwest at 3 knots by 1300 EDT. Such light and variable winds could allow or help the plume to extend away from shore.

Fig. III-8 is similar to Fig. III-6 except that it is for the afternoon aircraft flight on April 15, 1975. The isotherms shown are uncorrected for atmospheric water vapor absorption. The next step in the analysis was to apply a correction based upon boat measurements of ground truth temperatures. These results were then extrapolated to construct an isotherm map (Fig. IV-40 in the Mathematical Model section of this report).

Fig. III-9 is a digitized and contoured temperature map prepared by computer from the NOAA-4 VHRR (10.5 to 12.5 microns) IR data for south Florida on April 15, 1975 at 1335Z (0935 EDT). The data points are on a 2-km grid. Each data point is the average of six pixels or resolution cells of the satellite. The coldest areas (shaded) are radiation from clouds and can be ignored for our purposes. The satellite-measured isotherms in Fig. III-9 are $24^\circ C$, $28^\circ C$, and $32^\circ C$ (solid) and

BISCAYNE BAY
AND
CARD SOUND
FLORIDA

2.3 km

N

KEY
BISCAYNE

CUTLER RIDGE
POWER PLANT

TURKEY POINT

ELLIOT KEY

KEY LARGO

Ground Truth Time and Surface Temp. °F		Most Synchronous Aircraft Pass Time	Alt. (1000 Ft.)
		10 1246	2.0
(A)	1325 90°F	11 1257	2.0
		12 1448	2.0
		13 1500	2.0
		14 1513	2.0
		15 1227	2.0
		16 1438	2.5

Figure III-8

SURFACE COVERAGE OF
NASA-6 IR SCANNER DATA
SHOWING LOCATION OF
GROUND TRUTH DATA POINT

AFTERNOON, April 15, 1975
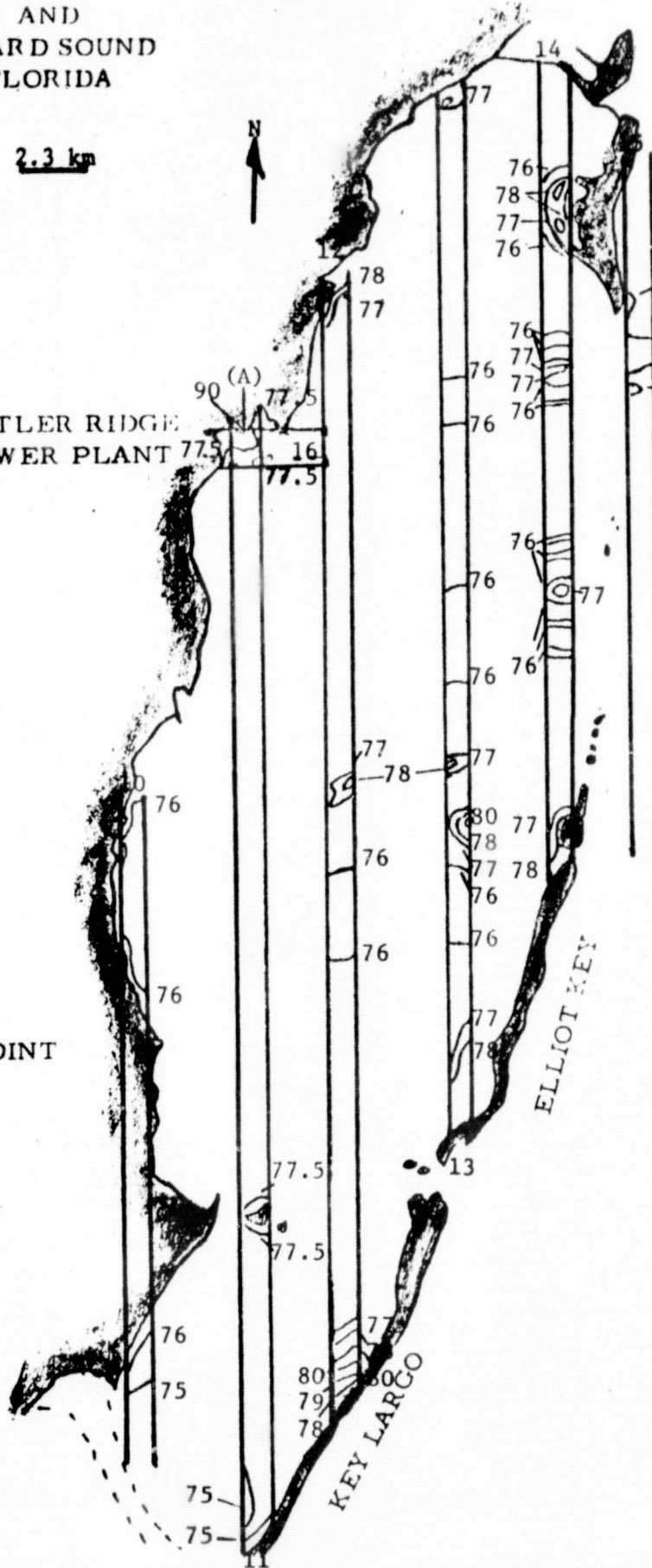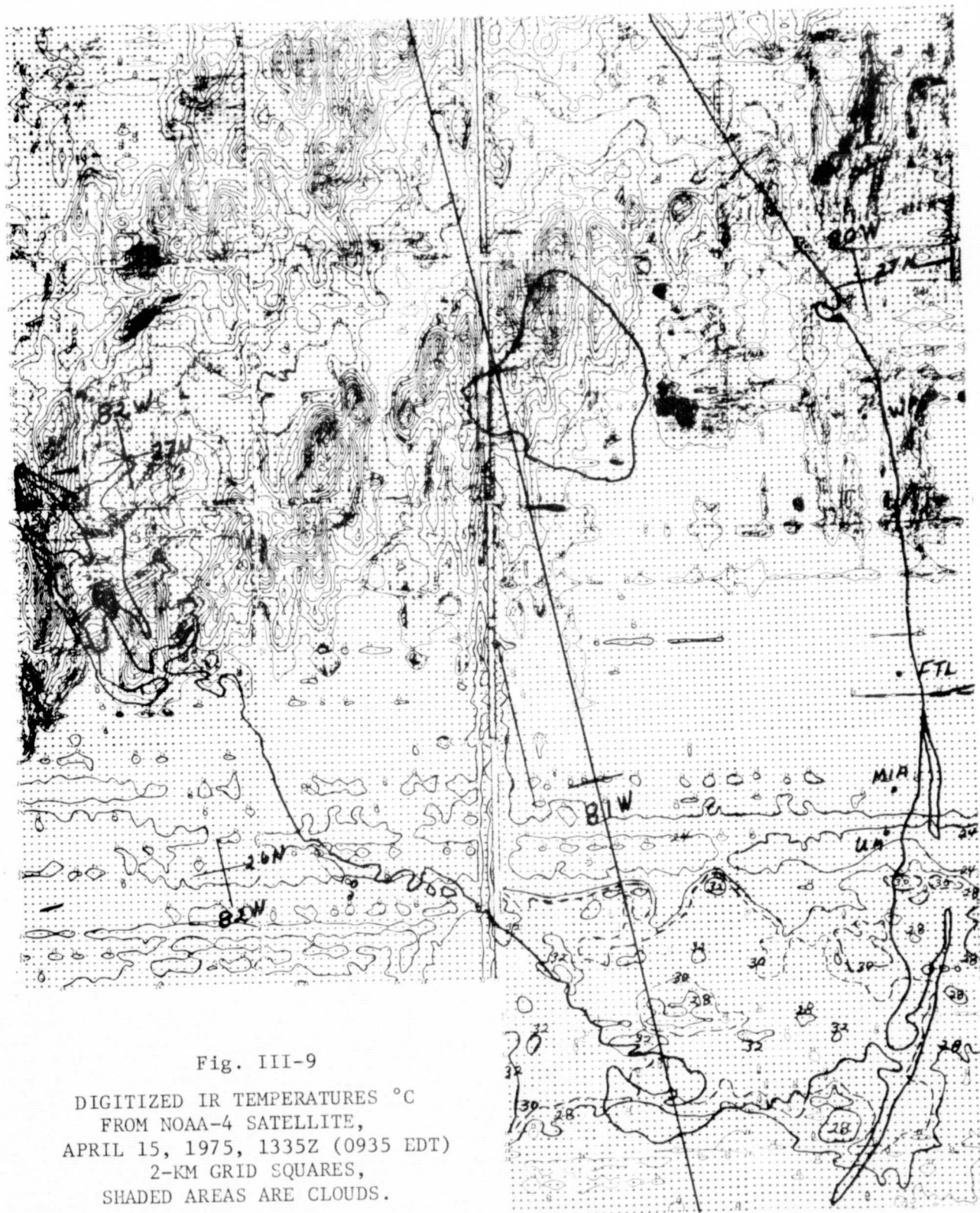
Fig. III-9

DIGITIZED IR TEMPERATURES °C
FROM NOAA-4 SATELLITE,
APRIL 15, 1975, 1335Z (0935 EDT)
2-KM GRID SQUARES,
SHADED AREAS ARE CLOUDS.

30°C (dashed).

This computer printout, which was prepared by the
National Environmental Satellite Service of NOAA in
Washington, D.C., contains a "U. S. Standard Atmosphere"
water vapor correction for IR absorption. The standard at-
mosphere correction is approximately 5°C less than that ob-
tained for conditions at Miami on April 15 as given by Table
III-3 and Fig. III-2. Thus, an additional 5°C should be added
to the temperatures in the Miami area in Fig. III-9 to cor-
rect them for the additional moisture of this climate. Apply-
ing this correction gives some small areas with 35°C water
temperatures in Biscayne Bay. These agree favorably with
some of the highest temperature measurements made by boat on
April 15. However, the spatial resolution and accuracy of
the NOAA-4 (ITOS series) satellite makes these observations
of limited significance for mesoscale thermal mapping, as
has been discussed earlier in this section.

E. Aircraft and Satellite Data, September 4, 1975

Fig. III-10 is an IR temperature measurement of
the Cutler Ridge Power Plant thermal plume made from the
NASA-6 aircraft on September 4, 1975 at 1525 EDT. This was
made from a flight altitude of 1800 ft. The temperatures
are in degrees Fahrenheit and are not corrected for atmos-
pheric water vapor absorption between flight level and the
water surface. The power plant had been in operation for
several hours and the plume was well developed by this time.

Table III-4 gives the precipitable water as
measured by the radio-sonde at Miami airport, 0800 EDT on
September 4, 1975. This information together with Fig. III-2
and ground truth is used to apply water vapor corrections to
the NASA-6 aircraft and NOAA-4 satellite radiometer measure-
ments of water temperatures in Biscayne Bay on September 4, 1975.
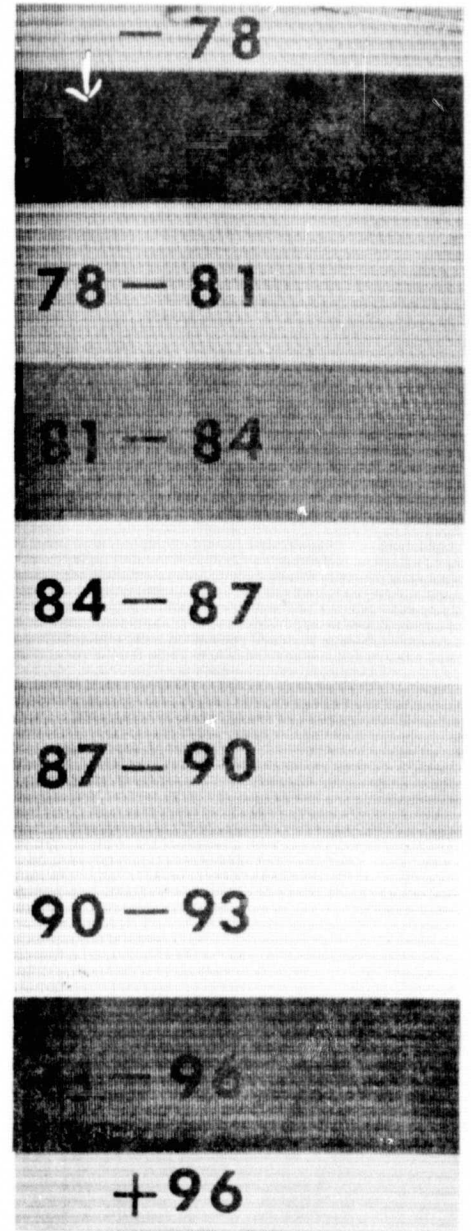
Figure III-10.   Thermal Plume from Cutler Ridge Power Plant,
1525 EDT, September 4, 1975, Flight Line 16A,
Flight Altitude 1800 ft.

Table III-4. Precipitable Water at Miami,
1200 Z (0800 EDT), September 4, 1975

Approximate Altitude Feet	Layers P_1/P_2	Mean e for Layer	Cumulative W cm for Layers
22,400	420	1.24	7.577
18,300	500		
	500	0.42	7.361
16,800	530		
	540	0.72	7.337
15,900	550		
	550	2.9	7.324
14,200	590		
	590	5.7	7.120
9,800	700		
	700	10.6	6.146
4,800	850		
	850	15.8	4.088
3,600	885		
	885	16.2	3.451
3,200	900		
	900	19.0	3.179
2,800	915		
	915	26.0	2.865
200	1000		
	1000	31.2	0.556
Surface	1018		

Fig. III-11 shows the thermal IR data gathered along flight paths on the afternoon of September 4, 1975. Clouds kept the aircraft at lower than optimum altitudes for good aerial coverage by the thermal scanner which has a 76-degree field of view normal to the flight path. The temperatures in Fig. III-11 are uncorrected for atmospheric water vapor absorption. This figure is similar to III-6 and likewise illustrates that the aircraft thermal IR data are not synoptic in time and that the aerial coverage is incomplete because of cloud limitations on flight altitude.

The flight strip data from Fig. III-11 were interpolated and extrapolated to produce the complete isotherm map in Fig. III-12. Boat measurements of ground truth temperature data were taken in the warm water plume near the Cutler Ridge Power Plant. Since the theoretical corrections for water vapor are too large in some instances, the boat measurements were used to adjust the temperatures in Fig. III-11 to obtain those in Fig. III-12.

The NOAA-4 satellite IR temperature data in digital format have not been received for September 4, 1975. An SMS-1/GOES satellite visual image at 1330Z (0930 EDT) shows scattered clouds over the southeast coastal region of Florida at the approximate time of the NOAA-4 satellite pass over this area. Thus it is believed that some NOAA-4 thermal IR water temperature data for Biscayne Bay will be available after processing by NOAA/NESS in Washington, D.C. Later in the day, the cloud cover became more extensive and would have prevented such satellite measurements.

Additional analysis will be performed on the September 4, 1975 data during the next phase of the project.

BISCAYNE BAY
AND
CARD SOUND
FLORIDA

KEY
BISCAYNE

CUTLER RIDGE
POWER PLANT
(16A)

TURKEY POINT

ELLIOT KEY

KEY LARGO
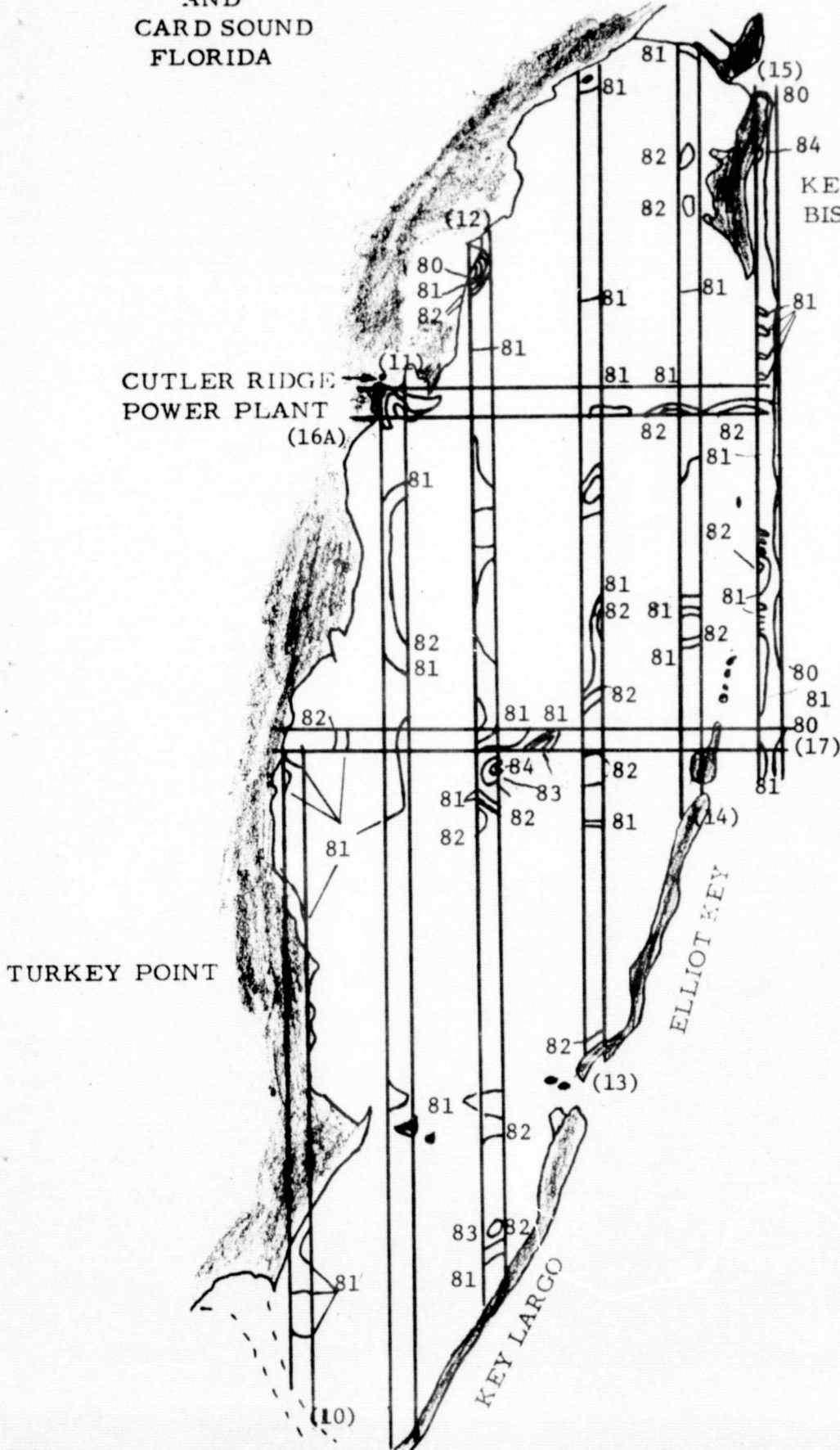
Aircraft Flight Line	Start Time EDT	Alt. (1000 Ft.)
(16A)	1312	2.0
(15)	1320	2.2
(13)	1338	1.8
(11)	1347	1.8
(10)	1420	1.8
(12)	1435	1.8
(14)	1500	1.8
(17)	1513	1.8

Fig. III-11

SURFACE COVERAGE OF
NASA-6 IR SCANNER DATA

September 4, 1975
(Afternoon Flight Lines)
(Uncorrected Temperatures)

BISCAYNE BAY
AND
CARD SOUND
FLORIDA

86.8

90.8

88.8

KEY
BISCAYNE

88.8

86.8

87.8

87.8

87.8

CUTLER RIDGE →
POWER PLANT

87.8

87.8

88.8

88.8

88.8

87.8

87.8

88.8

88.8

88.8

88.8

88.8

89.8
90.8

86.8

87.8

ELLIOT KEY

TURKEY POINT

87.8

87.8

87.8
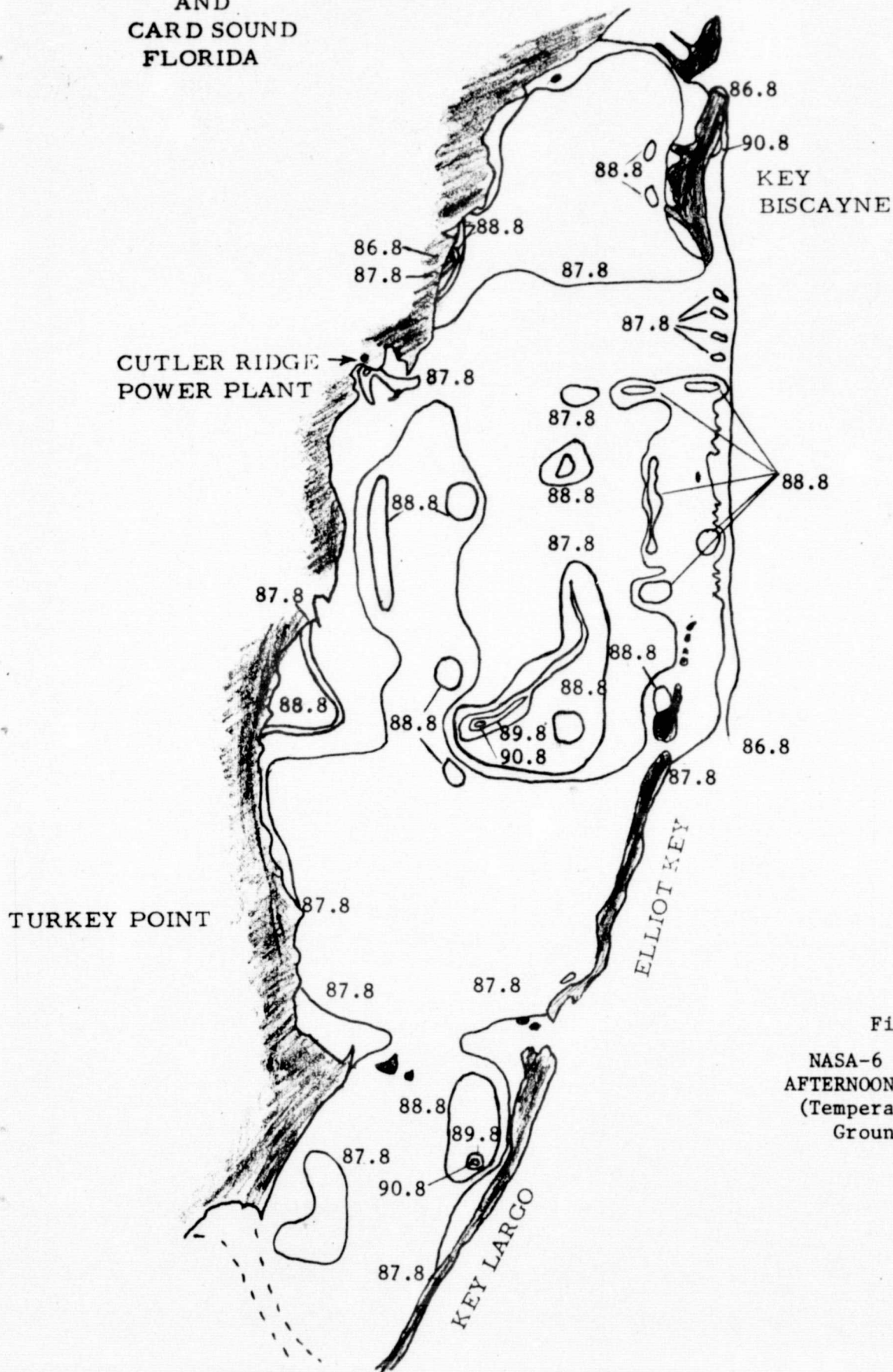
Fig. III-12

NASA-6 IR SCANNER DATA
AFTERNOON SEPTEMBER 4, 1975
(Temperatures Adjusted by
Ground Truth Data)

88.8

89.8

87.8

90.8

KEY LARGO

87.8

REFERENCES

1. Hiser, H. W., S. S. Lee, T. N. Veziroglu, and S. Sengupta, <u>Application of Remote Sensing to Thermal Pollution Analysis</u>, Fourth Annual Remote Sensing or Earth Resources Conference, University of Tennessee Space Institute, Tullahoma, Tennessee, March 24-26, 1975.

2. Saunders, P. M., "Corrections for Airborne Thermometry," <u>Journal Geophysical Research</u>, 75, 7596-7601,1970.

3. Wark, D. Q., G. Yamamoto, and J. H. Lienesch, "Methods of Estimating Infrared Flux and Surface Temperatures from Meteorological Satellites," <u>Journal of the Atmospheric</u> Sciences, 19, pp. 369-384, 1962.

4. Greaves, J. R., R. Wesler, and C. J. Bowley, <u>The Feasibility of Sea Surface Temperature Determination Using Satellite Infrared Data</u>, NASA Contractor Report, Washington, D. C., May 1966.

5. Byers, H. R., <u>General Meteorology</u>, 3rd Edition, McGraw-Hill, New York, P. 164, 1959.

IV. MATHEMATICAL MODEL

A. Introduction

The need for mathematical modelling in predicting
and monitoring thermal pollution was discussed in previous
reports by Veziroglu et al. (1973, 1974). Predictive studies
of ecosystems can only be made by mathematical models. A
priori knowledge of the effects of disturbances is essential
for environmental impact studies. Thus, the mathematical
model is a crucial tool in decisions involving power plant
siting, land development, etc.

The University of Miami team undertook to develop a
methodology using remote sensing and numerical modelling to
study thermal pollution. The need for remotely sensed data in
modelling has been discussed by Sengupta et al (1974). The re-
mote sensing effort has been discussed in detail in a previous
section. In this section the development and verification of
the numerical modelling effort will be presented.

The Biscayne Bay and Hutchinson Island areas in
Florida were chosen as sites for initial development and cali-
bration of the models. Fig. IV-1 shows the general layout for
Biscayne Bay. The Bay is approximately 25 kilometers long and
8 kilometers wide. It has several basins connected by shallow
limestone sills. The Bay is isolated from the Atlantic Ocean
by a series of keys. The major ocean efflux occurs through the
safety valve area between Key Biscayne and Soldier Key. This
is about 5 kilometers long with shallow limestone sills 1 to
3 kilometers wide. There are about 20 channels in this area
with a maximum depth of 5 meters. The lower part of the Bay
has a number of creeks open to the ocean. The maximum depth
in the Bay is 4 meters. The Featherbed Banks effectively di-
vide the Bay into two parts. There are two Florida Power &
Light power plants located on the shoreline. The plant at
Cutler Ridge has an open cycle cooling system discharging into
the Bay. The Turkey Point plant uses a series of cooling canals.

Fig. IV-2 shows the general location of the Hutchinson Island site. Here the open ocean boundary conditions are dominant. The water at this site is considerably deeper than the Biscayne Bay site. The effects of surface height displacements are more significant. A nuclear plant with two units of 850 MW each will discharge heated water at this location.

The hydrodynamics and thermodynamics of an ecosystem are controlled by geometry, meteorological conditions and physical characteristics of the water, such as salinity and turbidity. The governing equations are therefore composed of the Navier-Stokes equations, energy equation, salinity equation, the equation of state and some transport equation for turbidity. Various assumptions can be made for different situations leading to simplification or elimination of equations.

The effects of salinity have been ignored in the models until now although capability to include them exists. A discussion on the equation of state in Appendix I clarifies the relative importance and role of salinity. The individual formulations discussed later in this chapter justify the inclusion or exclusion of salinity more specifically. In general, if the salinity gradients are small enough to give densimetric Froude numbers greater than one, salinity effects can be ignored. Even where salinity does modify circulation, if the convective effects on temperature fields are non-significant, salinity can be ignored since our main concern is thermal pollution.

In the initial feasibility report it was proposed to develop a single model to incorporate the effects of thermal pollution for the whole Bay. However, since the effect of the plume is manifest only in a small domain of the order of a few square miles, it is wasteful in terms of computational time to have a single model. Therefore, separate models are being developed for near field and far field. The near field is the

region affected by the plume. The far field is the whole eco-
system under consideration. The far field affects the near
field significantly but not vice versa. The initially sug-
gested numerical scheme was a marker and cell method. In our
present study it was felt that a stretching suggested by
Phillips and used successfully in studies by Freeman et al.(1972)
and Sengupta and Lick (1974) was more suitable. The method
allows easy adaptation to various bottom topographies, an im-
portant requirement for any general model.

Owing to the aforementioned considerations, the
mathematical modelling effort has been divided into two parts;
the rigid-lid formulation and the free surface formulation.
The rigid-lid formulation artificially forces vertical velocities
to zero thereby eliminating surface gravity waves. This usually
leads to larger integration time steps since the Courant-Levy-
Fredrichs stability condition is relaxed. The effect of sur-
face height variation manifests itself as a lid-pressure. The
free-surface formulation allows surface movement and gravity
waves, the surface pressure being atmospheric. The rigid-lid
formulation is useful for lakes or cases where surface eleva-
tion changes are slow and are small compared to total depth.
The transients are somewhat distorted owing to damping. The
free surface model is more general although usually its full
capacities are utilized in situations where surface height
fluctuations are important.

No rigorous criterion exists for selecting either
the free-surface or rigid-lid model. However, there are some
comparative studies to guide the user's judgment. Crowley
(1969, 1970) compared both free-surface and rigid-lid models
for ocean circulation and found the rigid lid model satisfactory
except for errors in predicting Rossby wave speeds. The rigid-
lid results for Biscayne Bay, when compared with free-surface
results, will indicate the differences, if any, for shallow
bays with tidal flushing. A conservative approach would be

to use the free surface model for all open ocean and tide
dominated flows. Even then a vast majority of thermal
pollution sites would be accurately modelled by the rigid-
lid formulation.

The rigid-lid far field model has been developed
and applied to Biscayne Bay and general agreement with
remote sensing data has been obtained. The free-surface
model has been programmed and preliminary results obtained.

B. Free Surface Model

1) Model Formulation

The set of equations governing the behavior
of the fluid flow are those expressing the conservation of
mass, momentum, and energy in a turbulent flow. The Cartesian
coordinate system is used here, with z-coordinate in the verti-
cal direction as shown in Fig. IV-3. In order to keep the
generalized nature of the model, all the significant terms in
the pertinent conservation equations are retained. Included
are the effects of buoyancy, inertia, coriolis, density and
turbulent mixing. Wind shear and heat flux at the free sur-
face are also considered. Provision is made to include sal-
inity effect by adding a salinity concentration equation and
modifying the equation of state. The equation of state given
in this section is in a general form. As discussed in the
last section, a specified equation of state may be chosen
depending on the local situation of the site where the model
is to be applied.

One major difficulty in the treatment of the
Free Surface Model is at the free surface boundary. The
boundary conditions can be specified but the position of the
free surface is a variable and must be determined. In addition
to this, the shape of the free surface is irregular, making
it very difficult to apply any grid system at this boundary

for numerical solution. The approach used in this study
is to follow a vertical stretching transformation suggested
by Philips (1957). Using this transformation, the free surface
becomes a fixed flat surface and the variable surface height
remains constant.

Another scheme used in this study is to adapt
a horizontal stretching of coordinates similar to that of
Waldrop and Farmer (1974). In this way, a variable size
grid system may be used to give more detailed description
of the flow in the thermal discharge area, while larger grid
sizes may be used for farther points to cover a large area.

It is obvious that closed-form analytical
solution of this set of complicated, coupled, unsteady,
three-dimensional non-linear partial differential equations
is impossible to get. The finite difference method is used
to obtain numerical solutions. The central difference
approximation is used for the space differential. For the
time differential, forward difference and central difference
are used alternately to insure stability. The formulation
of the free surface model is completed and has been pro-
grammed for the UNIVAC 1106 computer system at the University
of Miami Computer Center. The computer program is being
debugged and some preliminary results have been obtained.

2) <u>Governing Equations</u>

The following partial differential equations, written in
Cartesian coordinates, describe the three-dimensional unsteady
fluid flow:

CONTINUITY EQUATION:

$$\frac{\partial u}{\partial x} + \frac{\partial v}{\partial y} + \frac{\partial w}{\partial z} = 0 \tag{4-1}$$

MOMENTUM EQUATIONS:

$$\frac{\partial u}{\partial t} + u\frac{\partial u}{\partial x} + v\frac{\partial u}{\partial y} + w\frac{\partial u}{\partial z} = -\frac{1}{\rho}\frac{\partial P}{\partial x} - fv + K_H\frac{\partial^2 u}{\partial x^2}$$

$$+ K_H\frac{\partial^2 u}{\partial y^2} + K_v\frac{\partial^2 u}{\partial z^2} \tag{4-2}$$

$$\frac{\partial v}{\partial t} + u\frac{\partial v}{\partial x} + v\frac{\partial v}{\partial y} + w\frac{\partial v}{\partial z} = -\frac{1}{\rho}\frac{\partial P}{\partial y} + fu + K_H\frac{\partial^2 v}{\partial x^2}$$

$$+ K_H\frac{\partial^2 v}{\partial y^2} + K_v\frac{\partial^2 v}{\partial z^2} \tag{4-3}$$

$$\frac{\partial w}{\partial t} + u\frac{\partial w}{\partial x} + v\frac{\partial w}{\partial y} + w\frac{\partial w}{\partial z} = -\frac{1}{\rho}\frac{\partial P}{\partial z} + K_H\frac{\partial^2 w}{\partial x^2} + K_H\frac{\partial^2 w}{\partial y^2}$$

$$+ K_v\frac{\partial^2 w}{\partial z^2} - g \tag{4-4}$$

ENERGY EQUATION:

$$\frac{\partial T}{\partial t} + u\frac{\partial T}{\partial x} + v\frac{\partial T}{\partial y} + w\frac{\partial T}{\partial z} = B_H\frac{\partial^2 T}{\partial x^2} + B_H\frac{\partial^2 T}{\partial y^2} + B_v\frac{\partial^2 T}{\partial z^2} \tag{4-5}$$

SALINITY EQUATION:

$$\frac{\partial S}{\partial t} + u\frac{\partial S}{\partial x} + v\frac{\partial S}{\partial y} + w\frac{\partial S}{\partial z} = D_H\frac{\partial^2 S}{\partial x^2} + D_H\frac{\partial^2 S}{\partial y^2} + D_v\frac{\partial^2 S}{\partial z^2} \tag{4-6}$$

EQUATION OF STATE

$$\rho = \rho(T,S) \tag{4-7}$$

Here

u, v, w are scalar components of the velocity vector
in the x, y, z directions, respectively;

p is the pressure;

ρ is the density;

f is the coriolis parameter;

g is the gravity

T is the temperature;

S is the salinity concentration;

K_H and K_V are the eddy viscosity in the horizontal and
vertical directions;

B_H and B_V are the eddy thermal diffusivity in the
horizontal and vertical directions; and

D_H and D_V are the eddy diffusion coefficient in the
horizontal and vertical directions.

For the type of flows under consideration, transient response
is gradual and the inertia and viscous terms in Equation (4-4)
are negligible when compared with the pressure and the gravity
terms. Equation (4-4) may then be simplified to give the
hydrostatic approximation for pressure by

$$0 = \frac{1}{\rho} \frac{\partial P}{\partial z} + g \qquad (4-8)$$

3) Transformation of the Vertical Coordinate

In the present study, both the free surface and
the realistic bottom topography are considered, and to apply
finite difference equations at these irregular boundaries for
numerical solutions is quite difficult. To solve this problem,
a transformation of the vertical coordinate is used to give a
constant height for the free surface and a flat bottom boundary
in the new coordinate system by letting

$\alpha = x$

$\beta = y$

$$\sigma = \frac{Z(x,y,z,t)}{H(x,y,t)} = \frac{z + \eta(x,y,t)}{H(x,y,t)} \qquad (4-9)$$

where $Z = Z(x,y,z,t)$ is the position of the fluid
element relative to the free surface and

H = H(x,y,t) is the depth contour also relative
to the free surface.

The Z variable decomposes into the two components Z = z +
$\eta(x,y,t)$, where z represents the vertical position relative
to the mean water level (MWL) and η gives the free surface
elevation measured positively upward from this mean water level.
The H variable separates into the components H = h(x,y) +
$\eta(x,y,t)$, where h represents the depth relative to the mean
water level. The value of σ ranges monotonically from zero
at the free surface to unity at the bottom of the lake. The
relationship between these two coordinate systems is shown in
Fig. IV-4. Fig. IV-5 gives the transformed vertical topography
in the (α,β,σ) coordinate system.

Substituting transformations (4-9) into Equations (4-1) to
(4-8), the governing equations in the (α,β,σ) coordinates may
be obtained as follows:

Continuity Equation:

$$\frac{\partial H}{\partial t} + \frac{\partial (Hu)}{\partial \alpha} + \frac{\partial (Hv)}{\partial \beta} + H\frac{\partial \Omega}{\partial \sigma} = 0 \tag{4-10}$$

Momentum Equations

$$\frac{\partial (Hu)}{\partial t} + \frac{\partial (Huu)}{\partial \alpha} + \frac{\partial (Huv)}{\partial \beta} + H\frac{\partial (u\Omega)}{\partial \sigma}$$

$$= H \left[-\frac{1}{\rho} \left(\frac{\partial p}{\partial \alpha}\right) + g\left(\sigma\frac{\partial H}{\partial \alpha} - \frac{\partial \eta}{\partial \alpha}\right) - fv \right]$$

$$+ K_H \left[\frac{\partial}{\partial \alpha} \left(H\frac{\partial u}{\partial \alpha}\right) \right] + K_H \left[\frac{\partial}{\partial \beta} \left(H\frac{\partial u}{\partial \beta}\right) \right]$$

$$+ \frac{1}{\rho} \left[\frac{\partial}{H\partial \sigma} \left(\rho K_v \frac{\partial u}{\partial \sigma}\right) \right] \tag{4-11}$$

$$\frac{\partial (Hv)}{\partial t} + \frac{\partial (Huv)}{\partial \alpha} + \frac{\partial (Hvv)}{\partial \beta} + H\frac{\partial (v\Omega)}{\partial \sigma}$$

$$= H \left[-\frac{1}{\rho} \left(\frac{\partial p}{\partial \beta}\right) + g\left(\sigma\frac{\partial H}{\partial \beta} - \frac{\partial \eta}{\partial \beta}\right) + fu \right]$$

$$+ K_H \left[\frac{\partial}{\partial \alpha} \left(H\frac{\partial v}{\partial \alpha}\right) \right] + K_H \left[\frac{\partial}{\partial \beta}\left(H\frac{\partial v}{\partial \beta}\right) \right]$$

$$+ \frac{1}{\rho} \left[\frac{\partial}{H\partial \sigma} \left(\rho K_v \frac{\partial v}{\partial \sigma}\right) \right] \tag{4-12}$$

Energy Equation :

$$\frac{\partial(HT)}{\partial t} + \frac{\partial(HuT)}{\partial x} + \frac{\partial(HvT)}{\partial y} + H\frac{\partial(\Omega T)}{\partial \sigma}$$

$$= B_H \left[\frac{\partial}{\partial \alpha} (H\frac{\partial T}{\partial \alpha}) \right] + B_H \left[\frac{\partial}{\partial \beta} (H\frac{\partial T}{\partial \beta}) \right]$$

$$+ \frac{1}{\rho} \left[\frac{\partial}{H\partial \sigma} (\rho B_v \frac{\partial T}{\partial \sigma}) \right] \qquad\qquad (4-13)$$

Salinity Equation

$$\frac{\partial(HS)}{\partial t} + \frac{\partial(HuS)}{\partial \alpha} + \frac{\partial(HvS)}{\partial \beta} + H\frac{\partial(\Omega S)}{\partial \sigma}$$

$$= D_H \left[\frac{\partial}{\partial \alpha} (H\frac{\partial S}{\partial \alpha}) \right] + D_H \left[\frac{\partial}{\partial \beta} (H\frac{\partial S}{\partial \beta}) \right]$$

$$+ \frac{1}{\rho} \left[\frac{\partial}{H\partial \sigma} (\rho D_v \frac{\partial S}{\partial \sigma}) \right] \qquad\qquad (4-14)$$

The hydrostatic approximation for pressure:

$$P(\sigma) = P(0) + gH \int_0^\sigma \rho(\sigma) \, d\sigma \qquad\qquad (4-15)$$

Here $\Omega = \frac{d\sigma}{dt}$ is the vertical velocity in the (α, β, σ) coordinates. It should be noted that Ω is zero at both the free surface and the bottom boundary.

4) Horizontal stretching of the Coordinate System

It is desirable to obtain a more detailed description of the flow near the discharge point while larger grid size may be used in the further points to save computation time. A horizontal stretching of the coordinate system is used here to create a more efficient use of the grid points by letting

$$X = \frac{1}{C_1} \tan^{-1} (\frac{\alpha}{C_2}) \qquad\qquad (4-16)$$

$$Y = \frac{1}{C_3} \tan^{-1} (\frac{\beta}{C_4}) ; \text{ and} \qquad\qquad (4-17)$$

$$X' = \frac{dX}{d\alpha}; \quad Y' = \frac{\partial Y}{\partial \beta}; \quad X'' = \frac{d^2X}{d\alpha^2}; \quad Y'' = \frac{d^2Y}{d\beta^2}$$

Here C_1, C_2, C_3, and C_4 are arbitrary constants. Using this transformation, even increments of ΔX and ΔY will produce a closer spacing of grid points in the original physical coordinates near the plume discharge where better resolution is needed. This transformation will also produce ever-increasing increments of the physical grid size away from the plume discharge, thus extending the region of computation as shown in Figs. IV-6 and IV-7.

The transformed governing equations in the stretching (X,Y) coordinates are then given below:

Continuity Equation:

$$\frac{\partial H}{\partial t} + X'\frac{\partial(Hu)}{\partial X} + Y'\frac{\partial(Hv)}{\partial Y} + H\frac{\partial \Omega}{\partial \sigma} = 0 \qquad (4-18)$$

U - Momentum Equation

$$\frac{\partial(Hu)}{\partial t} + X'\frac{\partial(Huu)}{\partial X} + Y'\frac{\partial(Huv)}{\partial Y} + H\frac{\partial(u\Omega)}{\partial \sigma}$$

$$= H\left[-\frac{X'}{\rho}\left(\frac{\partial p}{\partial X}\right) + gX'\left(\sigma\frac{\partial H}{\partial X} - \frac{\partial \eta}{\partial X}\right) - fv \right]$$

$$+ K_H\left[(X')^2\frac{\partial H}{\partial X}\frac{\partial u}{\partial X} + H(X')^2\frac{\partial^2 u}{\partial X^2} + HX''\frac{\partial u}{\partial X} \right]$$

$$+ K_H\left[(Y')^2\frac{\partial H}{\partial Y}\frac{\partial u}{\partial Y} + H(Y')^2\frac{\partial^2 u}{\partial Y^2} + HY''\frac{\partial u}{\partial Y} \right]$$

$$+ \frac{1}{\rho}\left[\frac{1}{H}\frac{\partial}{\partial \sigma}\left(\rho K_v\frac{\partial u}{\partial \sigma}\right) \right] \qquad (4-19)$$

V - Momentum Equation

$$\frac{\partial(Hv)}{\partial t} + X'\frac{\partial(Huv)}{\partial X} + Y'\frac{\partial(Hvv)}{\partial Y} + H\frac{\partial(v\Omega)}{\partial \sigma}$$

$$= H\left[-\frac{Y'}{\rho}\left(\frac{\partial p}{\partial Y}\right) + gY'\left(\sigma\frac{\partial H}{\partial Y} - \frac{\partial \eta}{\partial Y}\right) + fu \right]$$

$$+ K_H \left[(X')^2 \frac{\partial H}{\partial X} \frac{\partial v}{\partial X} + H(X')^2 \frac{\partial^2 v}{\partial X^2} + HX'' \frac{\partial v}{\partial X} \right]$$

$$+ K_H \left[(Y')^2 \frac{\partial H}{\partial Y} \frac{\partial v}{\partial Y} + H(X')^2 \frac{\partial^2 v}{\partial Y^2} + HY'' \frac{\partial v}{\partial Y} \right.$$

$$+ \frac{1}{\rho} \left[\frac{1}{H} \frac{\partial}{\partial \sigma} \left(\rho K_v \frac{\partial v}{\partial \sigma} \right) \right] \qquad (4\text{-}20)$$

Energy Equation

$$\frac{\partial (HT)}{\partial t} + X' \frac{\partial (HuT)}{\partial X} + Y' \frac{\partial (HvT)}{\partial Y} + H \frac{\partial (\Omega T)}{\partial \sigma}$$

$$= B_H \left[(X')^2 \frac{\partial H}{\partial X} \frac{\partial T}{\partial X} + H(X')^2 \frac{\partial^2 T}{\partial X^2} + HX'' \frac{\partial T}{\partial X} \right]$$

$$+ B_H \left[(Y')^2 \frac{\partial H}{\partial Y} \frac{\partial T}{\partial Y} + H(Y')^2 \frac{\partial^2 T}{\partial Y^2} + HY'' \frac{\partial T}{\partial Y} \right]$$

$$+ \frac{1}{\rho} \left[\frac{1}{H} \frac{\partial}{\partial \sigma} \left(\rho B_v \frac{\partial T}{\partial \sigma} \right) \right] \qquad (4\text{-}21)$$

Salinity Equation

$$\frac{\partial (HS)}{\partial t} + X' \frac{\partial (HuS)}{\partial X} + Y' \frac{\partial (HvS)}{\partial Y} + H \frac{\partial (\Omega S)}{\partial \sigma}$$

$$= D_H \left[(X')^2 \frac{\partial H}{\partial X} \frac{\partial S}{\partial X} + H(X')^2 \frac{\partial^2 S}{\partial X^2} + HX'' \frac{\partial S}{\partial X} \right]$$

$$+ D_H \left[(X')^2 \frac{\partial H}{\partial Y} \frac{\partial S}{\partial Y} + H(Y')^2 \frac{\partial^2 S}{\partial Y^2} + HY'' \frac{\partial S}{\partial Y} \right]$$

$$+ \frac{1}{\rho} \left[\frac{1}{H} \frac{\partial}{\partial \sigma} \left(\rho D_v \frac{\partial S}{\partial \sigma} \right) \right] \qquad (4\text{-}22)$$

The hydrostatic pressure approximation will remain the same:

$$P(\sigma) = P(0) + gH \int_0^\sigma \rho(\sigma) d\sigma \qquad (4\text{-}23)$$

5) Initial and Boundary Conditions

To start the calculation, initial conditions
are needed. Initial velocity, temperature, density and
salinity concentration should be specified throughout the
domain. This information may be obtained from remote sen-
sing, in-situ measurement and other sources. Boundary con-
ditions are to be specified at the lateral boundaries of the
domain, at the air-water interface and at the bottom of the
basin. Also needed are boundary conditions at the efflux
points and at the thermal discharges. At all solid boundaries,
no-slip and non-normal velocity conditions are applied.
Adiabatic conditions are assumed at these boundaries for the
energy equation. At the air-water interface, the pressure is
set equal to the atmospheric pressure. Also, wind stress and
a heat transfer coefficient are to be specified at this boun-
dary. At points of thermal discharge, both velocity and
temperature are to be specified.

6) Numerical Scheme and Solution Technique

The finite difference equations for the set
of governing equations are obtained by using finite difference
approximations for the differentials. The central difference
is used for space while the forward difference and central
difference are used alternately for time to insure stability.
The grid point system used in the calculation is shown in Fig.
IV-9. A flow chart is given in Fig. IV-10 to show the pro-
cedures used in the numerical calculation. The computer
program is run on the UNIVAC 1106 Computer System at the
University of Miami Computer Center. It is arranged to have
each part of the calculation carried out by a subroutine. All
of these subroutines are called in by the main program. To
apply this model to a specific site, only those subroutines
that involve the boundary and initial conditions need to be
modified. All other subroutines are quite general. The
programming for the free surface has been completed.

C. Rigid Lid Model

One of the major model development tasks proposed for the project was the development of a rigid-lid model that can predict the hydrodynamics and thermodynamics of basin wide phenomena. Specifically, the capabilities of such a model are:

(i) Predict the wind driven circulation,

(ii) Predict the circulation caused by inflows and outflows to the domain,

(iii) Predict the thermal effects in the domain, and

(iv) Combine the aforementioned processes.

To this end a rigid-lid model has been developed and applied to Biscayne Bay. The calibration procedure consists of comparing ground-truth corrected airborne radiometer data with surface isotherms predicted by the mathematical model. This procedure is complete and the model is ready to be tested at other sites. Lake Belews in North Caroline, which Duke Power Company uses as a cooling lake, is a prospective site.

Some of the results presented here have been previously discussed in contract reports by Veziroglu et al. (1974, 1975) to NASA-KSC. This section attempts to present a comprehensive summary of the application of the rigid-lid model to Biscayne Bay. This subsection will deal with the formulation and justification of a rigid-lid model, its solution, the results, and their verification with NASA-6 thermal scanner data.

1) Rigid-Lid Formulation

The governing equations for fluid flow and heat transfer in a domain are a system of coupled non-linear second-order three-dimensional partial differential equations, which satisfy the local conservation laws for mass, momentum and energy. An equation of state completes the set of equations. For laminar flows molecular transport properties can be used to describe heat and momentum transfer. However, most geophysical flows are turbulent, so the time averaged Navier-Stokes equations and the turbulent closure condition are used,

in which the Reynolds stress terms are replaced by eddy
transport coefficients. The governing equations under
these assumptions for an incompressible fluid have been
derived by Sengupta and Lick (1974) and have been presented
in a report by Veziroglu et al. (1974). The hydrostatic
assumption has been made. The fluid is considered to be an
incompressible Boussinesq fluid. These assumptions are well
accepted and invoking them does not require further explanation.

The significant assumption made here is the
rigid-lid assumption. This assumption effectively eliminates
surface-gravity waves by imposing a zero vertical velocity
at the surface. This essentially means that the surface allows
slip conditions without any normal velocity. The surface
pressure is no longer atmospheric but represents a "lid-
pressure", which under some special steady state conditions
can be related to the surface elevation that would occur if
no lid were present. Transient time scales are distorted by
this assumption but circulation patterns are not affected
greatly. This has been demonstrated by Berdahl (1970),
Crowley (1969, 1970), Hag and Lick (1973) and other investi-
gators. For many environmental investigations, including the
study of thermal pollution, the rigid-lid assumption is
adequate. Considerable savings in computing time result from
eliminating the necessity to reproduce surface gravity waves.
The assumption is particularly applicable for cooling lake
studies, where surface elevation changes are not large and do
not occur rapidly.

The salinity equation has been dropped since
its effect in lakes is negligible and the rigid-lid model is
particularly designed for lakes. Even for Biscayne Bay the
effect of salinity on temperature fields is negligible, as is
shown in the Appendix on the equation of state. However,
salinity can be included in the model without too much difficulty.

For computational simplicity vertical stretching
is applied to the domain to convert it to constant depth basin.
This has been used by Freeman et al. (1972) and modified for
rigid-lid applications by Sengupta and Lick (1974). The stretch-
ing makes the model easily applicable to various bottom topographies.

Governing Equations

The programming difficulties for a three dimensional basin suggest a stretching of the vertical coordinate of the form.

$$\gamma = \tilde{z} / \tilde{h} \ (x,y)$$

This converts the basin to a constant depth one. Now the same number of grid points in the vertical direction may be used at the shallow or deep parts of the basin, without using variable grid sizes. The details of derivation are presented by Sengupta and Lick (1974). The non-dimensional governing equations in the new coordinate system α, β, γ (instead of $\tilde{x}, \tilde{y}, \tilde{z}$) are:

Continuity
Equation:
$$\frac{\partial (hu)}{\partial \alpha} + \frac{\partial (hv)}{\partial \beta} + h\frac{\partial \Omega}{\partial \gamma} = 0 \qquad (4\text{-}24)$$

Momentum
Equation:
$$\frac{\partial (hu)}{\partial t} + \frac{\partial (huu)}{\partial \alpha} + \frac{\partial (huv)}{\partial \beta} + h\frac{\partial (\Omega u)}{\partial \gamma} - \frac{h}{R_B} v$$

$$= - h \frac{\partial P_s}{\partial \alpha} - h B_x + \frac{1}{R_e} \frac{\partial}{\partial \alpha}(h\frac{\partial u}{\partial \alpha}) + \frac{1}{R_e} \frac{\partial}{\partial \beta}(h\frac{\partial u}{\partial \beta})$$

$$+ \frac{1}{\epsilon^2 R_e} \frac{1}{h} \frac{\partial}{\partial \gamma}(A_V^* \frac{\partial u}{\partial \gamma}) \qquad (4\text{-}25)$$

$$\frac{\partial (hv)}{\partial t} + \frac{\partial (huv)}{\partial \alpha} + \frac{\partial (hvv)}{\partial \beta} + h\frac{\partial (\Omega v)}{\partial \gamma} + \frac{h}{R_B} u$$

$$= - h\frac{\partial P_s}{\partial \beta} - hB_y + \frac{1}{R_e} \frac{\partial}{\partial \alpha}(h\frac{\partial v}{\partial \alpha}) + \frac{1}{R_e} \frac{\partial}{\partial \beta}(h\frac{\partial v}{\partial \beta})$$

$$+ \frac{1}{\epsilon^2 R_e} \frac{1}{h} \frac{\partial}{\partial \gamma}(A_V^* \frac{\partial v}{\partial \gamma}) \qquad (4\text{-}26)$$

Hydrostatic Equation:
$$\frac{\partial p}{\partial \gamma} = E_u(1 + \rho)h \qquad (4\text{-}27)$$

Energy Equation:

$$\frac{\partial (hT)}{\partial t} + \frac{\partial (huT)}{\partial \alpha} + \frac{\partial (hvT)}{\partial \beta} + h\frac{\partial (\Omega T)}{\partial \gamma}$$

$$= \frac{1}{P_e} \frac{\partial}{\partial \alpha}(h\frac{\partial T}{\partial \alpha}) + \frac{1}{P_e} \frac{\partial}{\partial \beta}(h\frac{\partial T}{\partial \beta}) + \frac{1}{P_e \epsilon^2} \frac{1}{h} \frac{\partial}{\partial \gamma}(B_V^* \frac{\partial T}{\partial \gamma})$$

$$(4\text{-}28)$$

Equation of State

$$\tilde{\rho} = 1.029431 - .000020\tilde{T} - .0000048\tilde{T}^2 \qquad (4-29)$$

where T is in degree celsius

and

$$\tilde{\omega} = \gamma \left(u\frac{\partial \tilde{h}}{\partial \tilde{x}} + \tilde{v}\frac{\partial \tilde{h}}{\partial \tilde{y}} \right) + \tilde{h}\tilde{\Omega}$$

where $\quad \tilde{\Omega} = \dfrac{\partial \tilde{y}}{\partial \tilde{t}}$

and $\tilde{w}(\tilde{z}=0) = 0 \quad$ (rigid-lid)

where
$$u = \tilde{u}/U_{ref}; \quad v = \tilde{v}/U_{ref}; \quad w = \tilde{w}/\epsilon U_{ref}; \quad t = \tilde{t}/t_{ref}$$

$$x = \tilde{x}/L; \quad y = \tilde{y}/L; \quad z = \tilde{z}/H; \quad \epsilon = H/L$$

$$P = \tilde{P}/\rho_{ref}U_{ref}^2; \quad T = \frac{\tilde{T}-T_{ref}}{T_{ref}}; \quad \rho = \frac{\tilde{\rho}-\rho_{ref}}{\rho_{ref}}$$

$$A_H^* = A_H/A_{ref}; \quad A_V^* = A_V/A_{ref}; \quad B_H^* = B_H/B_{ref}; \quad B_V^* = B_V/B_{ref}$$

$$t_{ref} = L/U_{ref}$$

Quantities with subscript 'ref' are reference quantities, H and L
are vertical and horizontal length scales. The variables with
wavy lines on top are dimensional quantities.

If $A_H = A_{ref}$ and $B_H = B_{ref}$

then $A_H^* = 1$ and $B_H^* = 1$.

$$Re = \frac{U_{ref}L}{A_{ref}}; \quad R_B = \frac{U_{ref}}{fL}; \quad P_r = \frac{A_{ref}}{B_{ref}}$$

$$Pe = Re \cdot Pr = \frac{U_{ref}L}{B_{ref}}; \quad Eu = \frac{qH}{U_{ref}^2}$$

If Prandtl number is equal to 1, then $A_{ref} = B_{ref}$.

A_H and A_V are the eddy viscosities in horizontal and vertical
directions.

B_H and B_V are the eddy diffusivities in horizontal and vertical
directions.

To obtain a predictive equation for pressure the horizontal momentum equations are integrated from z=0 to z=h where h is the non-dimensional depth $\tilde{h}/H$. The integrated equations are then differentiated with respect to α and β and summed.

The Poisson equation for surface pressure becomes:

$$\frac{\partial^2 P_s}{\partial \alpha^2} + \frac{\partial^2 P_s}{\partial \beta^2} = \frac{1}{h} \frac{\partial}{\partial \alpha} (-A_{x_1} + A_{x_2} + C_x - X_p)$$

$$+ \frac{1}{h} \frac{\partial}{\partial \beta} (-A_{y_1} - A_{y_2} + C_y - Y_p)$$

$$- \frac{1}{h} \left\{ \frac{\partial h}{\partial \alpha} \cdot \frac{\partial P_s}{\partial \alpha} + \frac{\partial h}{\partial \beta} \frac{\partial P_s}{\partial \beta} \right\} - \frac{\partial (\Omega)}{\partial t} (z = 0)$$

$$(4-30)$$

The last term is the Hirt and Harlow (1964) correction term which accounts for non-zero vertical velocities at the rigid lid. The variables (B_x, B_y, and A_{x_1}, A_{x_2} etc.) are given below.

$$A_{x_1} = \int_0^1 \left\{ \frac{\partial}{\partial \alpha} (huu) + \frac{\partial}{\partial \beta} (huv) + h \frac{\partial}{\partial \gamma} (\Omega u) \right\} d\gamma$$

$$A_{x_2} = \frac{h}{R_B} \int_0^1 v d\gamma$$

$$C_x = \frac{1}{R_e} \int_0^1 \left\{ \frac{\partial}{\partial \alpha} (h\frac{\partial u}{\partial \alpha}) + \frac{\partial}{\partial \beta} (h\frac{\partial u}{\partial \beta}) + \frac{1}{\epsilon^2} \frac{1}{h} \frac{\partial}{\partial \gamma} (A_V^* \frac{\partial u}{\partial \gamma}) \right\} d\gamma$$

$$X_p = E_u \int_0^1 h \left\{ \frac{\partial h}{\partial X} \int_0^\gamma \rho d\gamma + h\frac{\partial}{\partial \alpha} \int_0^\gamma \rho d\gamma - \gamma \frac{\partial h}{\partial \alpha} \rho \right\} d\gamma$$

$$A_{y_1} = \int_0^1 \left\{ \frac{\partial}{\partial \alpha} (huv) + \frac{\partial}{\partial \beta} (huv) + h\frac{\partial (\Omega v)}{\partial \gamma} \right\} d\gamma$$

$$A_{y_2} = \frac{h}{R_B} \int_0^1 u d\gamma$$

$$C_y = \frac{1}{R_e} \int_0^1 \left\{ \frac{\partial}{\partial \alpha} (h\frac{\partial u}{\partial \alpha}) + \frac{\partial}{\partial \beta} (h\frac{\partial u}{\partial \beta}) + \frac{1}{\epsilon^2} \frac{1}{h} \frac{\partial}{\partial \gamma} (A_V^* \frac{\partial u}{\partial \gamma}) \right\} d\gamma$$

$$Y_p = E_u \int_0^1 h \left\{ \frac{\partial h}{\partial \beta} \int_0^\gamma \rho \, d\gamma + h \frac{\partial}{\partial \beta} \int_0^\gamma \rho \, d\gamma - \gamma \frac{\partial h}{\partial \beta} \rho \right\} d\gamma$$

$$B_x = E_u \frac{\partial h}{\partial \alpha} \int_0^\gamma \rho \, d\gamma + E_u h \frac{\partial}{\partial \alpha} \int_0^\gamma \rho \, d\gamma - E_u \gamma \frac{\partial h}{\partial \alpha} \rho$$

$$B_y = E_u \frac{\partial h}{\partial \beta} \int_0^\gamma \rho \, d\gamma + E_u h \frac{\partial}{\partial \beta} \int_0^\gamma \rho \, d\gamma - E_u \gamma \frac{\partial h}{\partial \beta} \rho$$

The set of equations (24-30) together with the appropriate boundary conditions constitute the mathematical model.

Initial and Boundary Conditions

The nature of the equations require initial and boundary conditions to be specified. As the initial condition the velocities, temperature and density are specified throughout the domain. Boundary conditions are specified at the air-water interface, geographical boundaries of the domain, the bottom of the basin and at efflux points. At the air water interface a wind-stress and a heat transfer coefficient are specified. The conditions on the lateral walls are no slip and no normal velocity for the momentum equations. These walls are assumed to be adiabatic. At the floor of the basin, the conditions of no slip and no-normal velocity are applicable. The energy equation has a heat flux boundary condition, considered adiabatic for the present study. At points of efflux the velocities are specified and gradient of temperature normal to domain boundary is considered zero. These open boundary conditions are most difficult to specify.

Therefore, the boundary conditions are in summary:

At the surface

$\gamma = 0$

$\Omega = 0$ Rigid-Lid

$$\frac{\partial u}{\partial \gamma} = \left(\frac{hH}{U_{ref}} A_v\right) \tau_{zx} ; \quad \frac{\partial T}{\partial z} = \left(\frac{hHK_s}{B_z}\right) (T_E - T_S) ;$$

$$\frac{\partial v}{\partial \gamma} = \left(\frac{hH}{U_{ref}} A_v\right) \tau_{zy} ;$$

where τ_{zx} and τ_{zy} are wind stresses in the x and y - directions respectively

At the bottom of the basin:

$$\gamma = 1$$

$$\omega = 0$$

$$u = 0$$

$$v = 0$$

$$\frac{\partial T}{\partial \gamma} = 0$$

On lateral walls:

$$u = 0$$

$$v = 0$$

$$\Omega = 0$$

$$\frac{\partial T}{\partial x} = \frac{\partial T}{\partial \alpha} - \frac{\gamma}{h} \frac{\partial h}{\partial \alpha} \frac{\partial T}{\partial \gamma} = 0$$

$$\frac{\partial T}{\partial y} = \frac{\partial T}{\partial \beta} - \frac{\gamma}{h} \frac{\partial h}{\partial \beta} \frac{\partial T}{\partial \gamma} = 0$$

Method of Solution

The solution technique involves explicit numerical solution of the governing equations. The predictive equations which predict velocities are the momentum equations. The energy equation is explicitly solved for temperature. The Poisson equation, derived from the vertically integrated horizontal momentum equations for surface or lid pressure, is the predictive equation for pressure.

The finite difference equations for momentum and energy are obtained by using a forward time central space scheme with Dufort-Frankel differencing on the diffusion terms.

The finite difference equation for the u momentum equation may be written as:

$$\frac{u^{n+1}-u^n}{\Delta t} = (\text{Inertia})^n + (\text{Pressure})^n + (\text{Viscous})^{n,\ n+1,\ n-1}$$

The convective stability criterion is still effective with some relaxation of the diffusive stability criterion. The pressure equation is approximated by a five point scheme and solved by successive over relaxation (Liebmann method).

A staggered mesh is produced in which horizontal velocities and temperatures are calculated at integral nodes and vertical velocity and pressure are calculated at half grid points.

Solutions have been obtained for Biscayne Bay in three stages. First, a closed basin approximation was made and wind driven circulation was obtained. In the second step circulation in the Bay was obtained with an ocean efflux specified; the simultaneous effects of wind and ocean efflux were also investigated. The third and final stage obtained the temperature field for various ambient conditions and parameters. The results were compared with airborne thermal scanner data to calibrate the model. Some of the results have already been discussed in reports by Veziroglu et al. (1974). This procedure was followed in order to check the performance of the model for as wide a range of environmental situations as possible.

2) Wind Driven Circulation

Wind driven circulations for a sustained wind of about 5 mph for various directions (with a corresponding wind stress of .1 dynes/cm^2) have been obtained. Two cases, in which the wind is from the southeast and the north, are discussed in detail.

Fig. IV-10 shows the surface velocities for winds at 5 mph. The velocities vary significantly in the basin. The variation of velocity direction and magnitude results from a number of factors. The outline of the Bay guides the current near the shoreline. The bottom slopes tend to influence the velocity, and the local depth of the Bay is also significant. The shallower regions like shoals and near shore areas have smaller velocities. The reduction of velocity near the shore is caused mainly by the smaller depth rather than by shore boundary layers. Estimates by Sengupta and Lick (1974) have indicated that the sidewall boundary layers are thin for similar situations and do not extend as far as the nearest interior node (0.8 kilometers from the shore). Fig. IV-11 shows the velocities at a depth of two meters below the surface. There are no velocity vectors in large parts of the domain since the Bay is less than two meters deep in most places. The return flow can be clearly seen.

A cross-sectional view of the velocity field indicates a cell-like structure. Fig. IV-13 shows a section through J=7 (refer to Fig. IV-12). It can be seen that the surface velocities are in the direction of the wind stress and sharp upwelling occurs in the near shore region. Wherever there is a sharp change in bottom depth, horizontal gradients of velocity become significant and require vertical velocities to satisfy the continuity equations.

Fig. IV-13 shows the Featherbed regions (at point A) which divides the bay. In this area upwelling and downwelling regions are in close proximity. Due to this barrier (shallows) interchange between the different basins of the Bay may be greatly retarded.

Wind from Southeast

The prevailing winds during spring and summer are from the southeast. The surface velocities for a 5 mph wind from the southeast are shown in Fig. IV-14. Most of the surface currents are in the direction of the wind. It is important to note the effect of the shoreline and bottom topography on the flow. The magnitude of the velocities varies with depth and is smaller near shore and in the shallow shoal regions. In some parts near the mainland, the velocities are almost parallel to the shore. Near Cutler Ridge (I=11, J=4) the velocities are towards northwest indicating that with a southeast wind the plume will be pushed back towards the discharge mouth; thus shortening its longitudinal extent. The return flow at a depth of 2 meters is seen in Fig. IV-15. A cell like flow pattern is evident in Fig. IV-16. The Featherbed Banks tend to divide the two regions quite effectively.

3) Tidal Currents

The rigid-lid model does not reproduce level variations due to the tidal cycle. However, the tidal driving mechanism can be modelled by specifying the inflow and outflow velocities at ocean inlets during various phases of the tidal cycle.

The current measurements available for Biscayne Bay are very sparse and not systematic. Some measurements for Angelfish Creek, Broad Creek and Caesar Creek do exist. From these measurements and an average estimate for the shoal area, an order of magnitude value for tidal efflux velocity has been obtained.

A 10 cm/sec velocity for both the incoming and outgoing tidal phases is assumed. The program is executed with an incoming tide, and then the ocean-bay velocity pattern is gradually reversed to obtain a 10 cm/sec outgoing velocity. Though the details of phase relations, level changes and time dependence cannot be precisely modelled, the results should give a meaningful qualitative picture of the circulation.

Fig. IV-17 shows the surface velocities with an incoming tide. The major portion of the tidal mass influx

travels into the South Bay while the flow towards Ricken-
backer Causeway is minimal. The currents near the shoals
follow the influx direction but turn southward near the
shore. The water flow through the creeks causes local
modification of this southward flow. The velocities are
reduced around Featherbed Bank, causing relatively high
velocities in the deeper regions around the Bank. The
velocities also increase to the south as the Bay narrows.
The current near Cutler Ridge is from east to west indica-
ting that the plume (which issues north south) will be
turned towards the west shore of Biscayne Bay. Fig. IV-18
shows the velocities at a depth of 1 meter with an incoming
tide. The flow is unidirectional at most points. The re-
verse current seen in wind-driven circulation does not occur.
The reason for this is that in the case of wind driven current,
the driving mechanism is at the surface, resulting in a pres-
sure gradient that causes reverse flow; whereas, in the case
of tidal currents the driving mechanism is a flow at all
depths in the ocean inlets.

The incoming flow was gradually reversed.
Fig. IV-19 shows the surface velocities at an intermediate
state. The currents have reversed in some places but not in
others. In Fig. IV-20, the currents at a depth of two meters
are almost completely reversed. This phase lag between sur-
face currents to currents at lower depths is expected; the
surface currents are larger and so take longer to reverse.

With outgoing tide from Biscayne Bay into the
ocean the flows are as expected. Fig. IV-21 shows that the
bulk of the outflow comes from south bay. At Cutler Ridge
the current is now from west to east, therefore with outgoing
tide the plume is expected to turn towards the east. Fig.
IV-21a shows that the currents at a depth of one meter are
completely reversed compared to the inflowing currents.

4) Currents with Wind and Tide

To investigate the circulation pattern with wind and tide acting simultaneously, a combination of 10 mph southeast and an incoming tide was considered. Fig. IV-22 shows the corresponding surface velocities for comparison with Fig. IV-17 (incoming tidal current only). The effect of the southeast wind is to turn the current vectors toward the northwest. This results in more water flow towards the northern part of the Bay. The velocities in the south bay are still essentially southward but are of a smaller magnitude due to the southeast wind. Figs. IV-23 and IV-24 show similar circulations at 1 and 2 meters depth, respectively. From Fig. IV-22 it can be seen that the current near Cutler Ridge is in a north-west-west direction indicating that the plume will be pushed toward the shore and broadened.

5) Temperature Fields

The energy equation is coupled to the momentum equations through the bouyancy term. Temperature gradients in the domain cause density gradients and consequently density currents. The circulation modification due to density currents causes changes in the temperature field. It is of interest to investigate the role of density currents in modifying temperature distribution. This is also important from a computational point of view since weak coupling would justify solving the energy equation with an invariant velocity field calculated a priori.

The temperature solutions for various combinations of parameters have been obtained for comparison to the remote sensing data from the April 14, 1974 NASA-6 flight over Biscayne Bay. It should be noted that the remote sensing data is not synoptic. Table IV-I shows a list of some of the cases for which solutions were obtained. At first a number of cases were run to obtain an estimate of the surface heat, transfer

coefficient, the effect of wind direction, wind magnitude, tidal flow and air temperature. The Bay was assumed to be initially isothermal and results were obtained for heating during the mid morning hours.

Cases 1 and 2 were run to investigate the effect of the surface heat transfer coefficient. The values for heat transfer coefficients are taken from Edinger and Geyer (1971) and suitably increased for daytime heating only. (The Edinger and Geyer values are averaged over the entire day.) A wind of 10 mph from the southeast is also assumed. Figs. IV-25 and IV-26 show the surface isotherms after 3 hours of heating for Cases 1 and 2, respectively. The shallow near-shore regions are warmer. The Card Sound area appears as a somewhat separate basin with closed isotherms. Featherbed Bank shows up as a developing warmer region. The warm spot over these banks is more pronounced for Case 1 which has a higher heat transfer coefficient.

Fig. IV-27 shows surface isotherms for Case 3, which are almost identical to those of Case 2. Increased convective effects due to higher wind shears has had little effect.

Cases 4 and 5 were executed to investigate the effects of density variation. Figs.IV-28 and IV-29 show sur-face and sectional (vertical) isotherms for Case 4, where density effects are excluded. Fig. IV-30 shows the surface isotherms after 3 hours for the same case. Case 5 is identi-cal to Case 4 except it includes the effects of density. Sur-face and vertical isotherms for Case 5 are shown in Fig. IV-31 and Fig. IV-32. Comparing Figs. IV-31 with IV-28 and IV-32 with IV-29, the effects of density can be seen. Since warmer fluid tends to rise and spread, the warm spot over Featherbed Banks is larger for Case 5 than for Case 4. Also comparing vertical sections, some of the sharp isotherm gradients near boundaries have been reduced by density currents; i.e., the isotherms have been made more horizontal.

Cases 6 through 10 were executed to investigate the effects of tidal flow. A combination of surface and initial temperatures and heat transfer coefficients were used to match the results with surface isotherms from remote sensing data. Figs. IV-33 through IV-39 show surface isotherms and vertical sections for some of these cases. Case 8 agreed most closely with the remote sensing data. Fig. IV-40, the surface isotherms obtained from IR data corrected with ground truth data, shows extremely good agreement with Fig. IV-35, the surface isotherms for Case 8. It should be pointed out, however, that the IR data is not truly synoptic. There is a time lag of almost three hours between the near shore flights and the flight over the keys. Considering this factor and the assumption of isothermal conditions in the early morning, the agreement is satisfactory.

By considering the cases mentioned above a choice of parameters which might agree with IR data can be made. The measured quantities cannot be altered; namely, wind speed (10 mph southeast), incoming tide and ambient temperature (30°C). To minimize the effect of initial temperature conditions, the run should be executed with as early a starting time as possible. Case 11 shows the selected parameters.

At 9 AM near location (I=11, J=3) the measured temperature was 25.6°C with no vertical stratification. Since this is a near shore location the "average" temperature in the Bay can be assumed to be lower. Since the detailed temperature field was not known as an initial condition it was assumed that that Bay is isothermal at a temperature of 24.5°C at 8 AM. This approximation in initial condition becomes less important with time. Therefore, comparisons with ground-truth or IR data were made only after the program had been executed for a few hours. The comparison with mid-afternoon IR data was after 6 hours.

Case 12 uses the same set of parameters but
includes effects of density. Figs. IV-41 and IV-42 show
isotherms for Case 11 after 3 hours. Fig. IV-43 shows the
surface isotherms after 6 hours, which may be compared with
Fig. IV-40. The qualitative and quantitative agreement with
the remotely sensed data is quite remarkable considering its
non-synoptic nature and the difficulty in specifying the
initial conditions for the Bay. Fig. IV-44 shows a transect
for Case 11 after 6 hours. Figs. IV-45 and IV-46 show the
isotherms after 3 hours with density effects included.
Since they are only slightly different from Figs. IV-41 and
IV-42, density currents are not significant in changing the
temperature distribution during this period.

The temperature distribution after 6 hours for
Case 12 is shown in Figs. IV-47 and IV-48. It is evident
from the surface isotherms that the hot spot over the shoals
has increased in area. This is expected since warmer fluid
rises and spreads at the surface when density effects are
included. The colder region in the Card Sound area has de-
creased in size as warmer fluid from the shallower shores
has spread at the surface. The agreement with remote sensing
data is very good, as a comparison with Fig.IV-40 indicates.

The ground truth data were obtained only in
the morning on April 15, 1975 field experiment.

Results for the model for Case 12 after 3 hours
of heating were compared with ground truth measurements at
location (I=11, J=7) at 11 AM. Fig. IV-49 shows a transect
of the bay along J=7. The calculated isotherms are shown with
ground truth data at location marked by asterisks. It can be
seen that the agreement is to within $0.7^{\circ}C$. This is satis-
factory for most environmental models.

6) <u>Conclusions</u>

A three-dimensional rigid-lid model has been used to study the general circulation and natural temperature distribution in Biscayne Bay. Remote sensing data has been used to calibrate and verify the model. The relevant conclusions from this study about transport of heat and mass in the bay are:

a) The tidal flow is the dominant driving mechanism for general circulation in the bay. The tide flows primarily into and out of the southern part of the bay. The wind modifies the circulation to some extent though not significantly.

b) The boundaries guide the tidal currents with velocities increasing as the bay narrows.

c) The bottom topography affects the circulation by reducing velocities near the shallows. The Featherbed Bank significantly affects velocities around it. Water flow tends to go around the Featherbed Bank resulting in relatively high velocities in deeper regions adjacent to the banks.

d) The tidal flow through the creeks produces only localized effects.

e) The temperature distribution is predominantly determined by the bottom topography and is warmer in shallower regions. The Featherbed Banks shows up as a warm spot. Vertical diffusion is the dominant heat transfer mechanism.

f) The effects of density change the temperature field over several hours.

g) The model has predicted within $1^{\circ}C$ the
3-D isotherms as compared to ground-truth
data.

It should be noted that these conclusions are
for Biscayne Bay only, with its rather unique shallow and
slowly varying depths, and not generalized conclusions for
all basins. The aspect ratio, the sharpness of bottom slopes,
and other factors, play a significant role. However, the
model is general enough to accommodate a wide range of geo-
graphical and meteorological conditions.

D. Near-Field Rigid-Lid Application

A thermal plume discharging into a body of water is at first dominated by a jet like behavior. The jet then spreads with turbulent mixing at the edges. Depending on the densimetric Froude number, the bouyancy effect manifests itself by causing the plume to rise and spread at the surface. Beyond this region the jet spreads by the action of general "far field" circulation and diffusion.

Fig. IV-50 shows the configuration of the surface discharge problem being formulated. The rigid-lid formulation described in previous sections still holds except that the boundary conditions are quite different. At the jet mouth the velocity, temperature and density profiles have to be specified. These are obtained from discharge measurements regularly recorded by power plant operating personnel. At the shoreline and bottom the same conditions as for far-field calculations apply, namely no slip, no normal velocity and adiabatic conditions. The outer boundary conditions are more difficult to specify.

The domain outer boundaries are chosen such that the thermal anomalies caused by the plume are in the domain. The procedure for this is to first choose an outer boundary and then run the program; if no significant changes are observed at these boundaries the plume is considered enclosed in the domain. However, if the changes at the boundaries are significant, a larger domain is selected. The procedure is repeated until the thermal anomaly region is completely en-closed in the domain.

At the outer boundaries the boundary conditions specified are zero gradients for velocity and temperature normal to the boundaries. This represents an approximation

that the boundaries are far enough so that gradients caused by the plume are non-significant.

The method of solution is essentially the same as that for the far field.

Preliminary results

The Cutler Ridge plume has been approximated to a rectangular discharge 15 meters wide and 1.8 meters deep. The domain has a lateral extent of 300 meters and longitudinal extent of 600 meters as a first approximation. This is divided in 20 grid spacings in both horizontal coordinates. The vertical extent is divided into 4 spacings. The domain is assumed to be of a constant depth of 1.8 meters (same as discharge depth).

The discharge is taken to be at 25 cm/sec. The vertical and horizontal eddy viscosities are 1 cm^2/sec. and 1000 cm^2/sec. respectively. The basin is initially considered still. These conditions are chosen to test the program since the behavior of the jet is expected to be a symmetrical lateral spreading with the bottom boundary layer thickening with axial distance.

Fig. IV- 51 shows the surface velocities for the discharge. The symmetrical spreading of the jet is clearly visible. The velocity decays away from the jet mouth as expected.

Fig. IV- 52 shows the centerline velocity decay with axial distance. It can be seen that the decay is relatively small initially owing to inertial dominance of the jet. Then the lateral mixing causes faster decay. Finally, the jet velocity asymtotically approaches zero since velocity gradients are small far away from the jet mouth.

The model results for the simple case considered
indicate physically reasonable behavior. Effects of bottom
topography, wind, temperature and currents are being in-
corporated. The program already has the capability to in-
clude effects of variable depth, wind, temperature and
currents. Execution of more realistic cases has been
initiated.

REFERENCES

1. Berdahl, P., Oceanic Rossby Waves: "A Numerical Rigid-Lid Model," ITD-4500, UC-34, Lawrence Radiation Laboratory, University of California Livermore.

2. Crowley, W.P., "A Numerical Model for Viscons Free Surface Barotropic, Wind-Driven Ocean Circulation," J. COMP. PHYS. 5, 1969.

3. Crowley, W.P., "A Numerical Model for Viscons Non-divergent Barotropic, Wind-Driven, Ocean Circulations," J. COMP. PHYS., 6, 1970.

4. Dittmar, W., 1884, "Report on Researches into the Composition of Ocean Water Collected by H.M.S. Challenger 1873-76. Sci. Res. Voyage "Challenger", 1873-76,"CHEM PHYS., 1, 1-211.

5. Edinger, J.E., Geyer, J.C., "Heat Exchange in the Environment," E.E.I. Publication, No. 65-902, Edison Electric Institute, 1971.

6. Forsch, C., Knudsen, M., and Sorensen, S.P.L., 1902, "Berichte uber die Konstantenkestimonungen fur Aufstellung der Hydrographischen Tabellen." Kgl. Danske Videnskab. Selskabs, Skifter, Naturvidenskab Math., Afdel XII 1, 1-151.

7. Freeman, N.G., Hale, A.M., Danard, M.B., "A Modified Sigma Equations Approach to the Numerical Modelling of Great Lakes Hydrodynamics." J. GEO. RES., Vol. 77, No. 6, 1972.

8. Haq, A., Lick, W., " The Time-Dependent Flow in Large Lakes with Applications to Lake Erie." Department of Earth Sciences,Case Western Reserve University, July, 1974.

9. Knudsen, M., 1901, "Hydrographical Tables, G.E.C. Gad, Copenhagen," Williams and Norgate, London.

10. Lyman, J., and Fleming, R.H., 1940, "Composition of Sea Water." J. MAR RES. 3, 134-148.

11. Phillips, N.A., "A Co-ordinate System Having Some Special Advantages for Numerical Forcastin~ ' J. METEOROL., 14, 1957.

12. Sengupta, S., and Lick, W., "A Nu   al Model ror Wind Driven Circulation and Temperature ields in Lakes and Ponds," FTAS/TR-74-99, Case Western Reserve University, 1974.

13. Sengupta, S., Lee, S.S., Veziroglu, T.N., Bland, T., "Application of Remote Sensing to Numerical Modelling," Proceedings of the Symposium on Remote Sensing Applied to Energy-Related Problems, 1974.

14. Veziroglu, T.N., Lee, S.S., Weinberg, N.L., Sengupta, S., "Application of Remote Sensing for Prediction and Detection of Thermal Pollution," NASA-CR-139182, 1974.

15. Veziroglu, T.N., Lee, S.S., Weinberg, N.L., Sengupta, S., "The Application of Remote Sensing to Detecting Thermal Pollution." NAS-10-8470, mid term report, May 1975.

16. Waldrop, W.R., Farmer, R.C., "Three-Dimensional Computation of Buoyant Plumes." J.G.R. Vol. 79, No. 9, 1974.

17. Weast, R.C. ed, "Handbook of Chemistry and Physic ," 52 edition, Published by the Chemical Rubber Co., Cleveland, ohio, 1968.

		TABLE IV-I				
CASE	WIND SPEED & DIRECTION (MPH)	HEAT TRANS-FER COEFFICIENT BTU/$^\circ$F-FT^2-day	EQUILI-BRUM TEMP. ($^\circ$C)	INITIAL TEMP	TOTAL ELAPSED TIME(HRS)	REMARKS
1	10, SE	1000	26	20	3	
2	10, SE	500	26	20	3	
3	20, SE	500	26	20	3	
4	10, SE	1000	29	20	3	
5	10, SE	1000	29	20	1	density effects included
6	10, SE	750	26	20	3	Incoming tide
7	10, SE	750	29	23	3	Incoming tide
8	10, SE	750	30	23	6	Incoming tide
9	10, SE	750	30	25.5	3	Incoming tide
10	10, SE	1000	30	25.5	3	Incoming tide
11	10, SE	750	30	24.5	6	Incoming tide
12	10, SE	750	30	24.5	3	Incoming tide density effects included
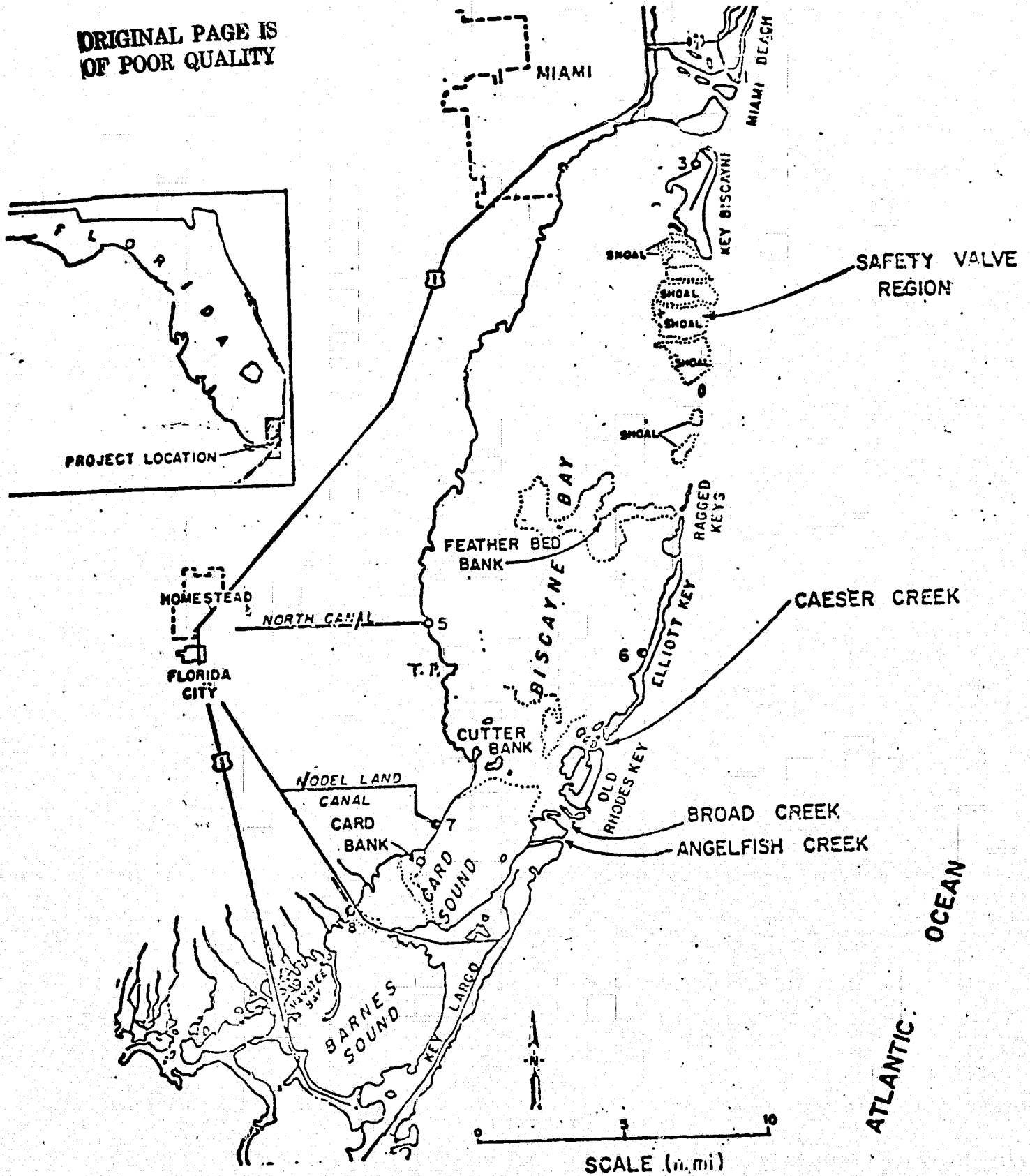
Fig. IV-1. Map Showing the General Area of Biscayne Bay
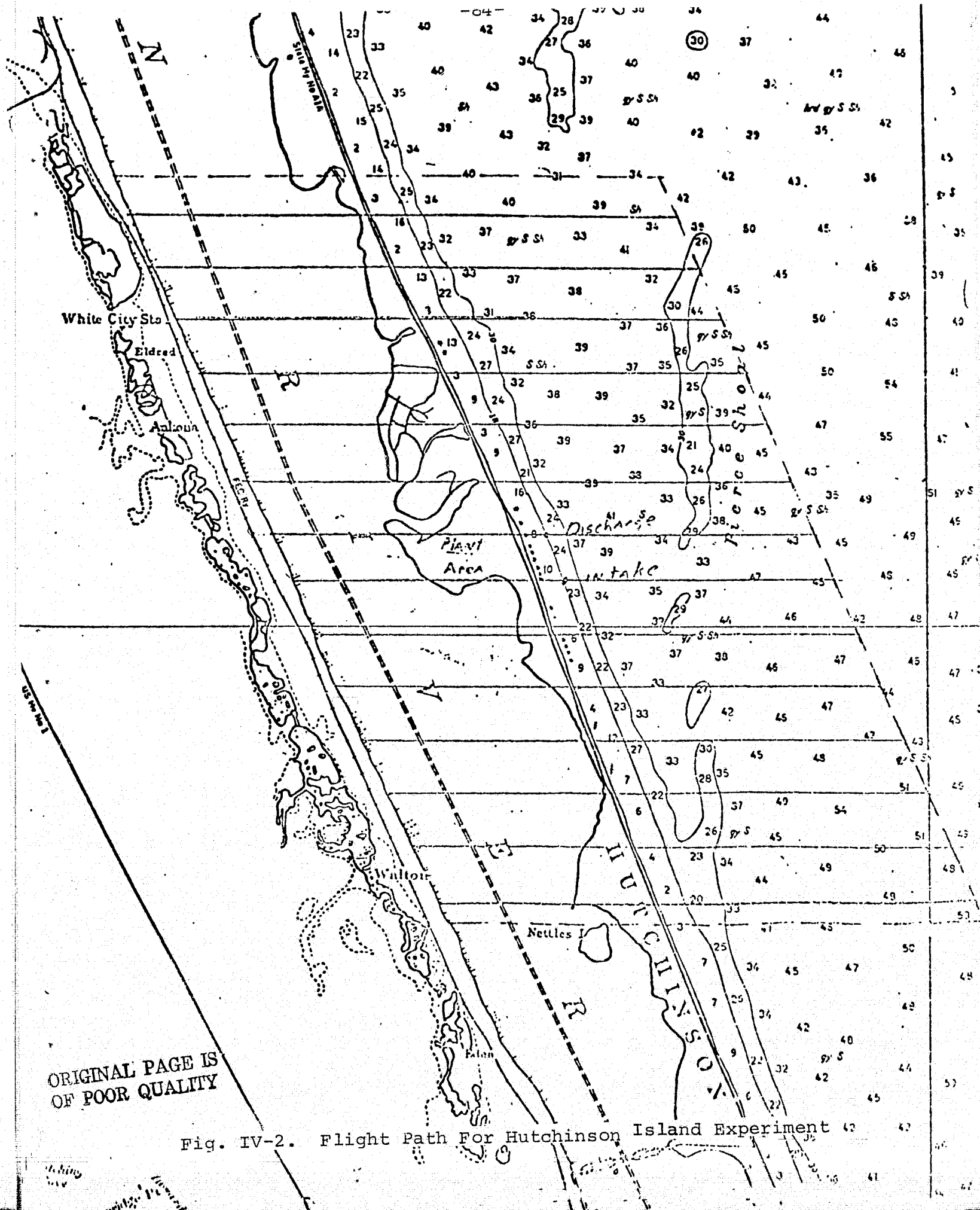
Fig. IV-2. Flight Path For Hutchinson Island Experiment
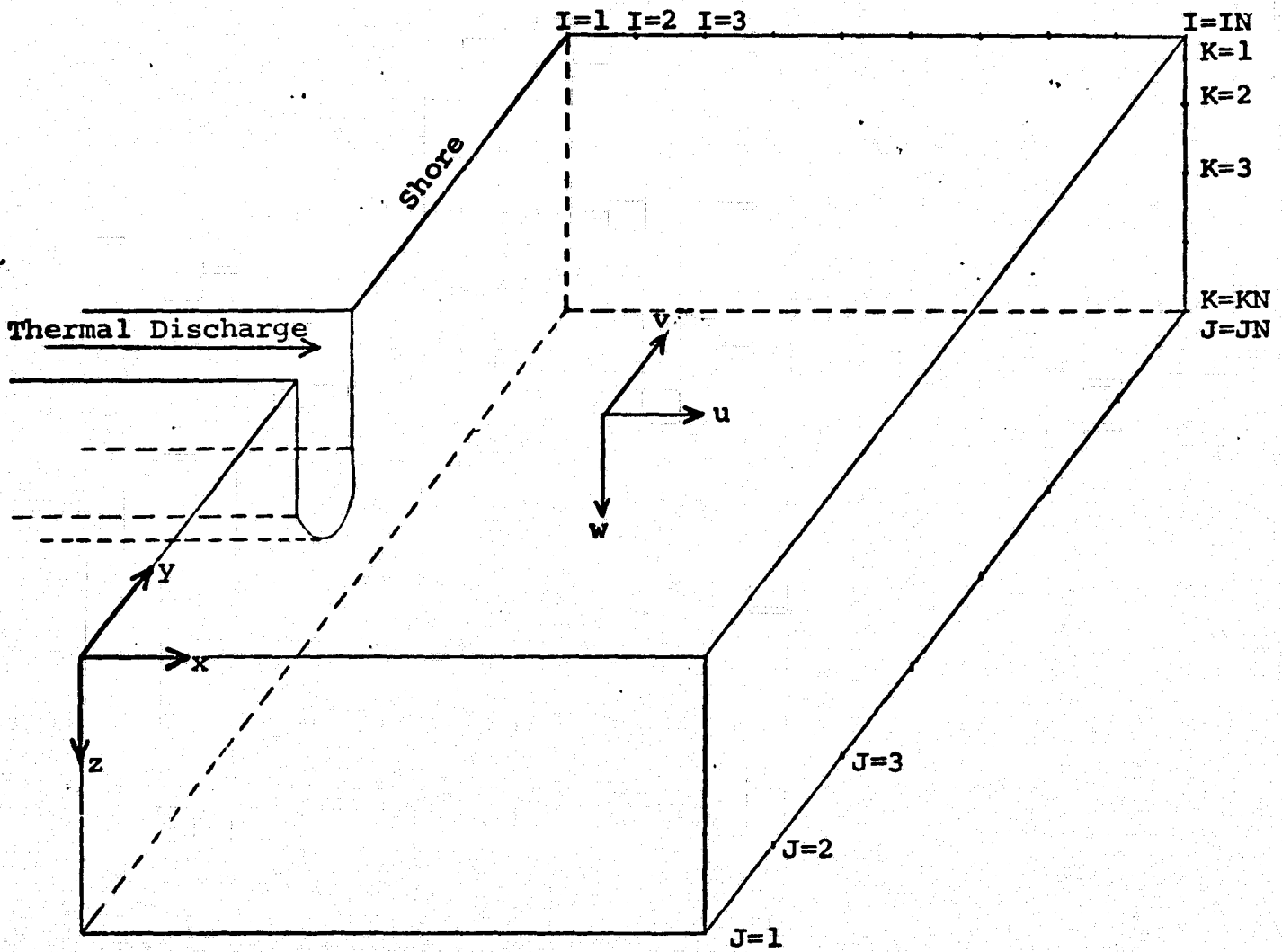
Fig. IV-3, COORDINATE AND GRID SYSTEMS
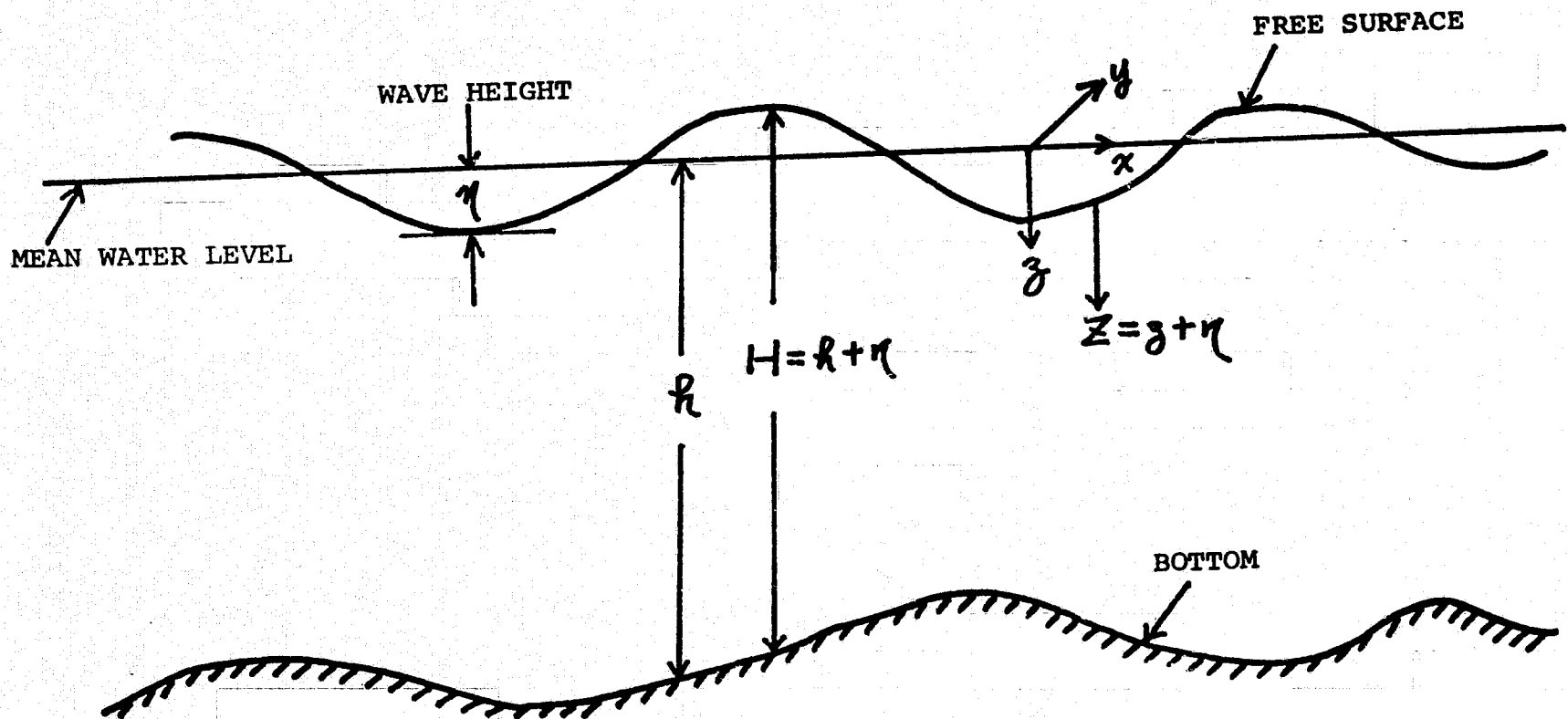
Figure IV-4. The xyz Coordinate System for the Free-Surface Model

The diagram shows the coordinate system with:

$\tau = 0$ at the FREE SURFACE, where $\omega = \dfrac{d\tau}{dt} = 0$

$\tau = 1$ at the BOTTOM, where $\omega = \dfrac{d\tau}{dt} = 0$

$$\alpha = x$$
$$\beta = y$$
$$\tau = \frac{z}{H}$$
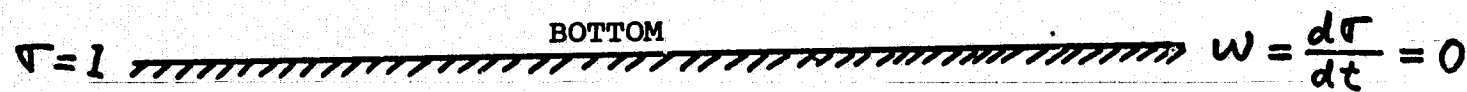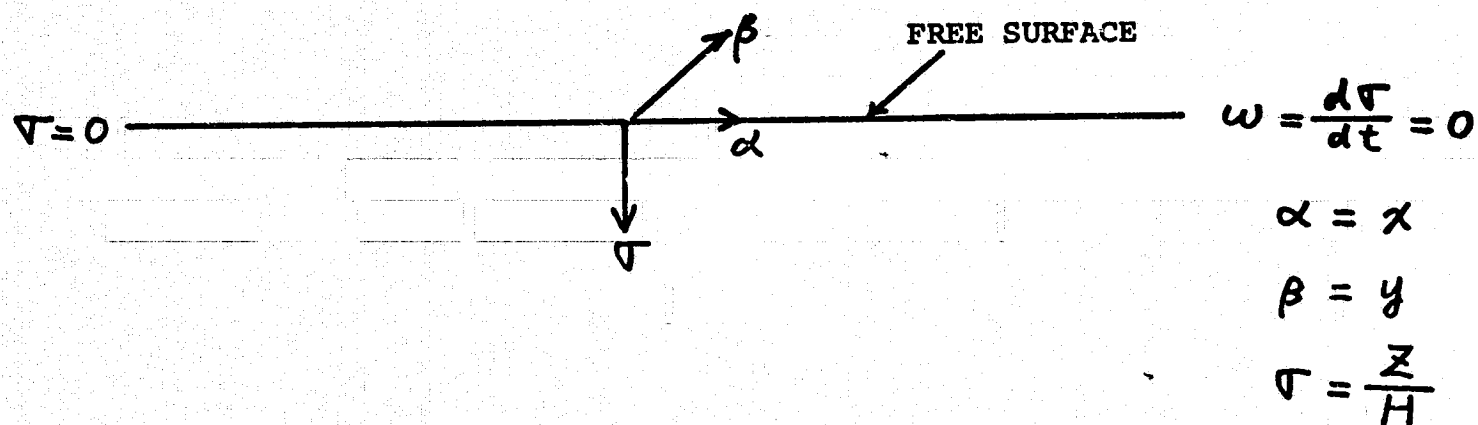
Fig. IV-5. The $\alpha\beta\sigma$ Coordinate System for the Free-Surface Model

FREE SURFACE

$$X = \frac{1}{C_1} \tan\left(\frac{\alpha}{C_2}\right)$$

$$Y = \frac{1}{C_3} \tan\left(\frac{\beta}{C_4}\right)$$

$$\sigma = \frac{Z}{H}$$

BOTTOM
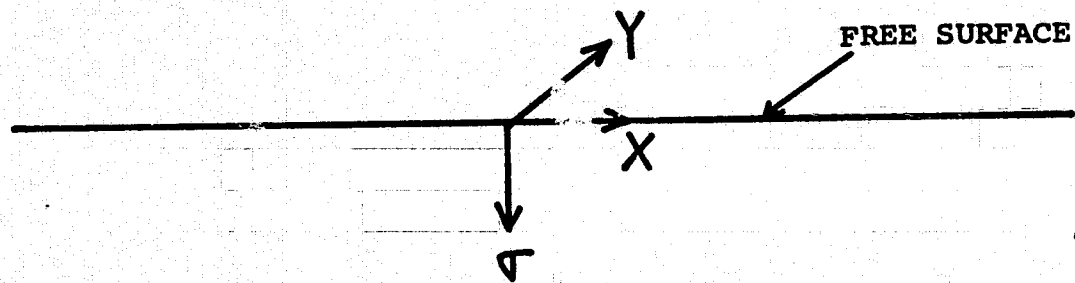
Figure IV-6. The $XY\sigma$ Coordinate System for the Free-Surface Model
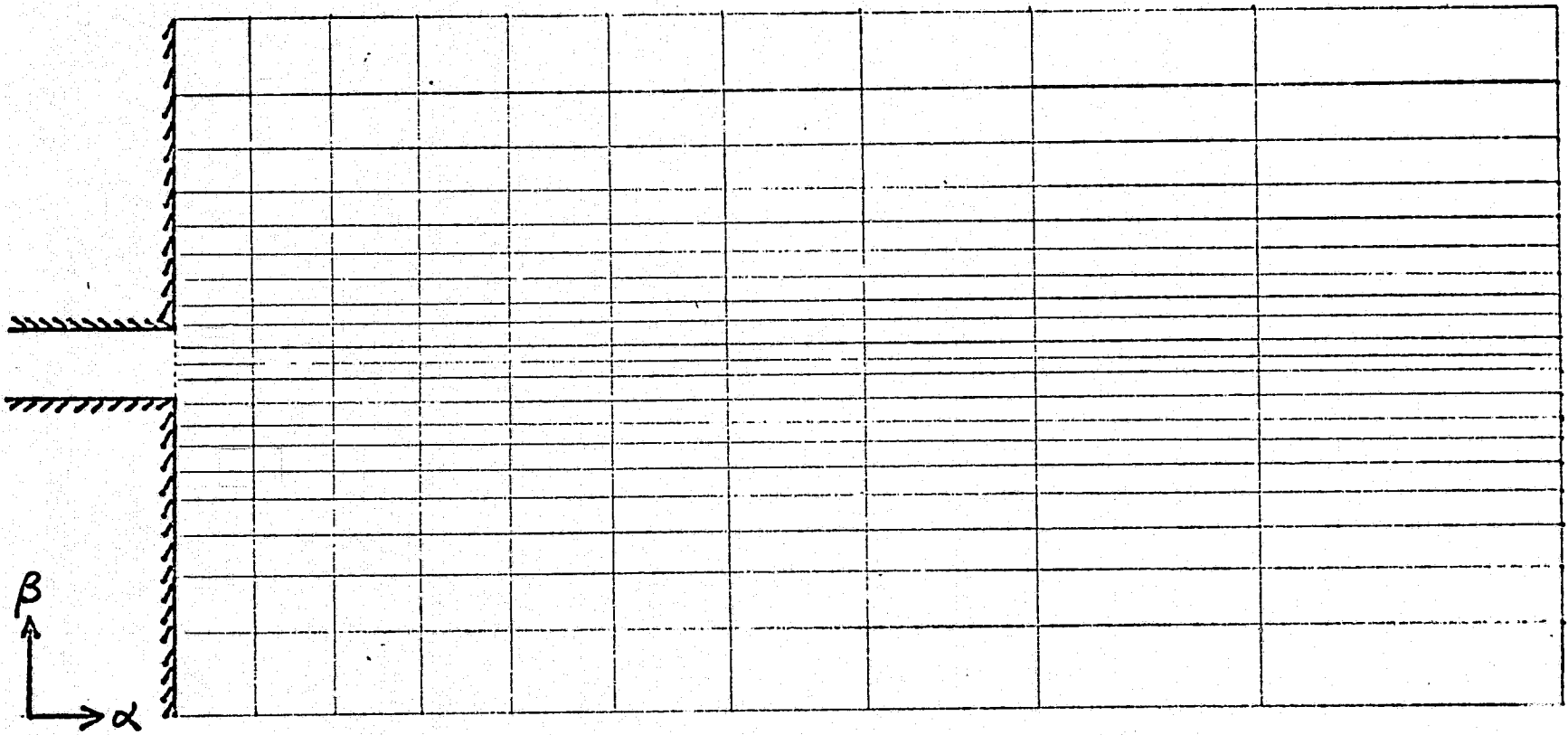
Figure IV-7.   Variable Grid Size System in α - β Coordinates
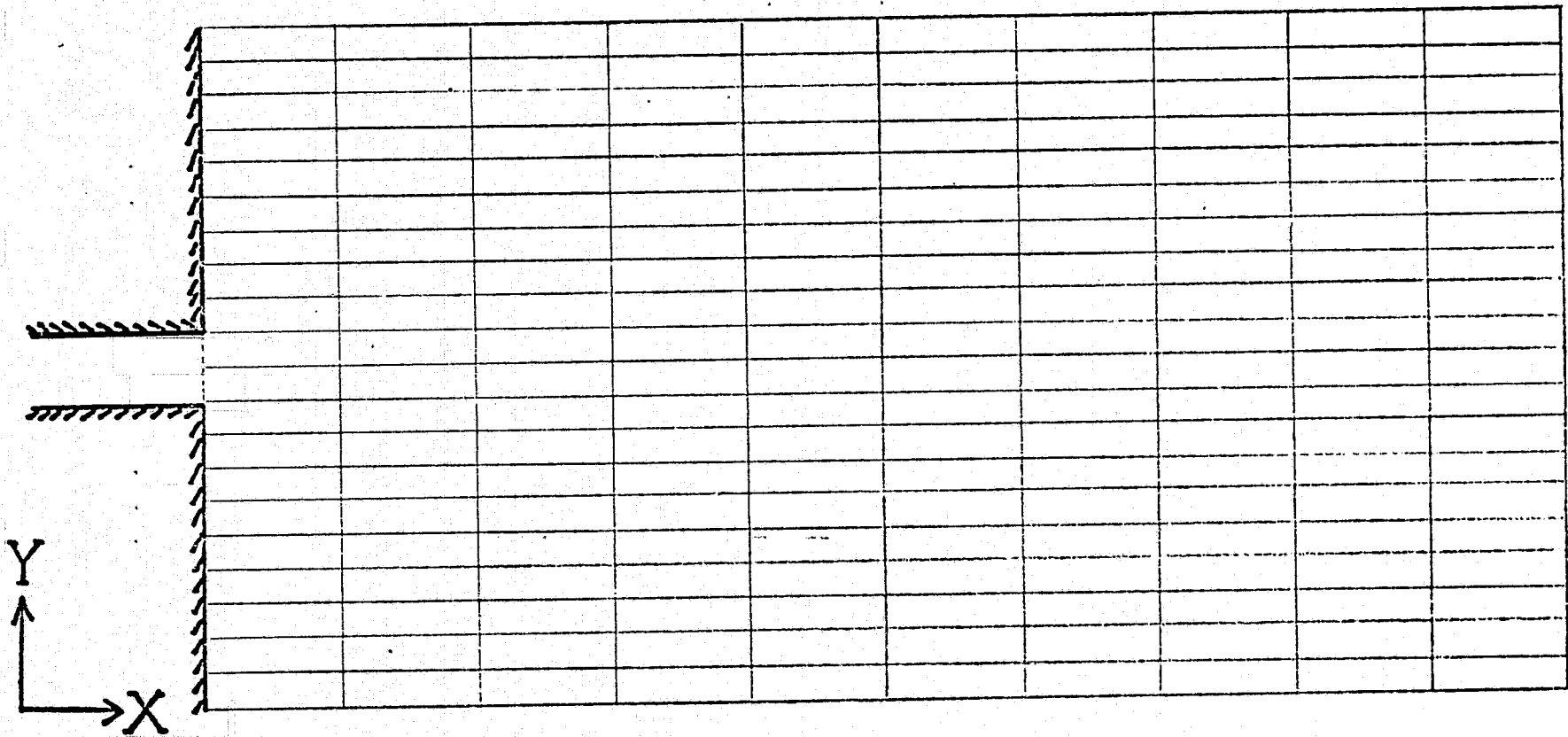
Figure IV-8   Constant Grid Size System in Transformed X - Y coordinates
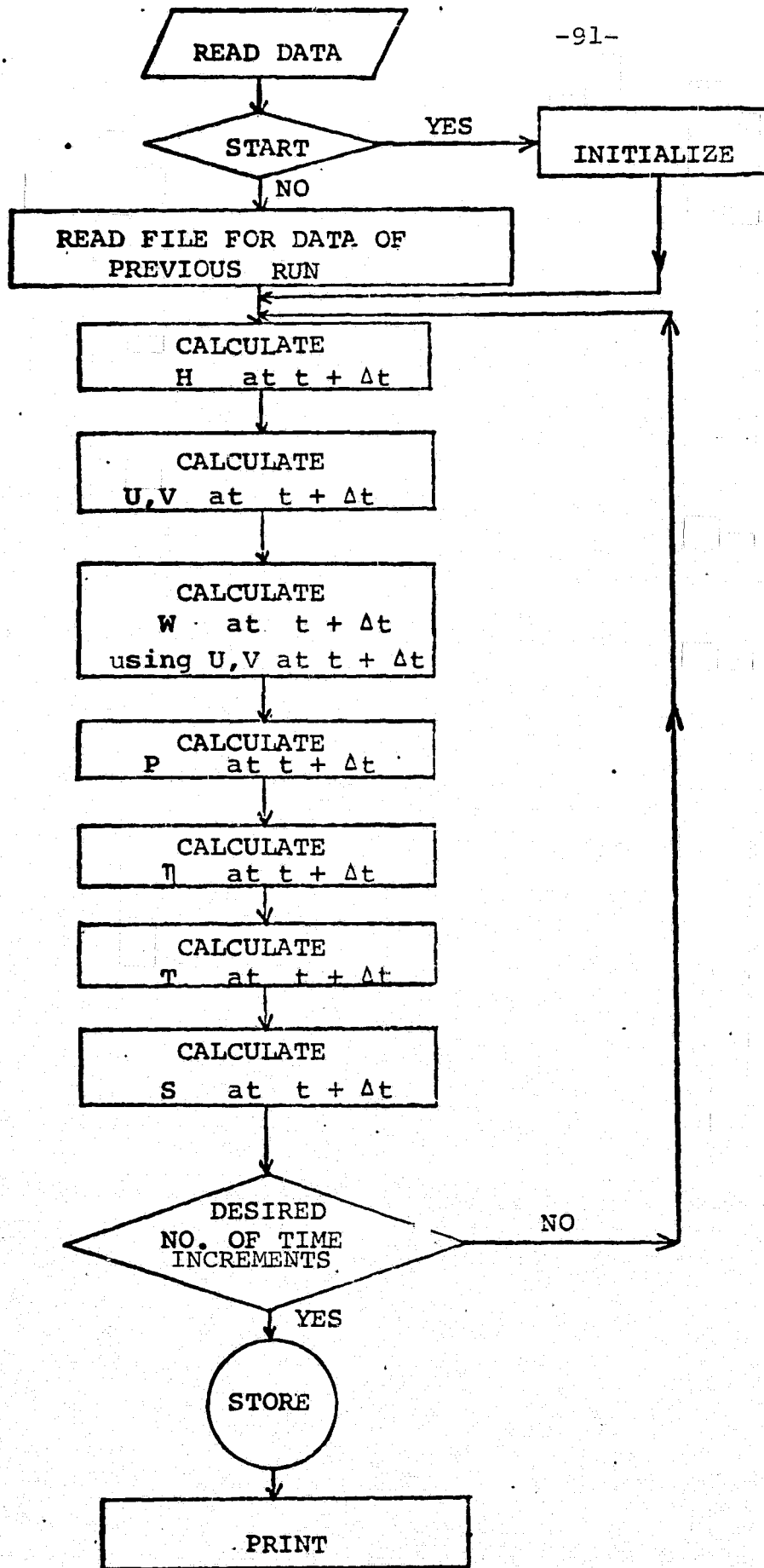
Fig. IV-9. Flow Chart for Free-Surface Model

Wind Stress = .1 dynes/cm^2

.8 kilometers

2 cm/sec
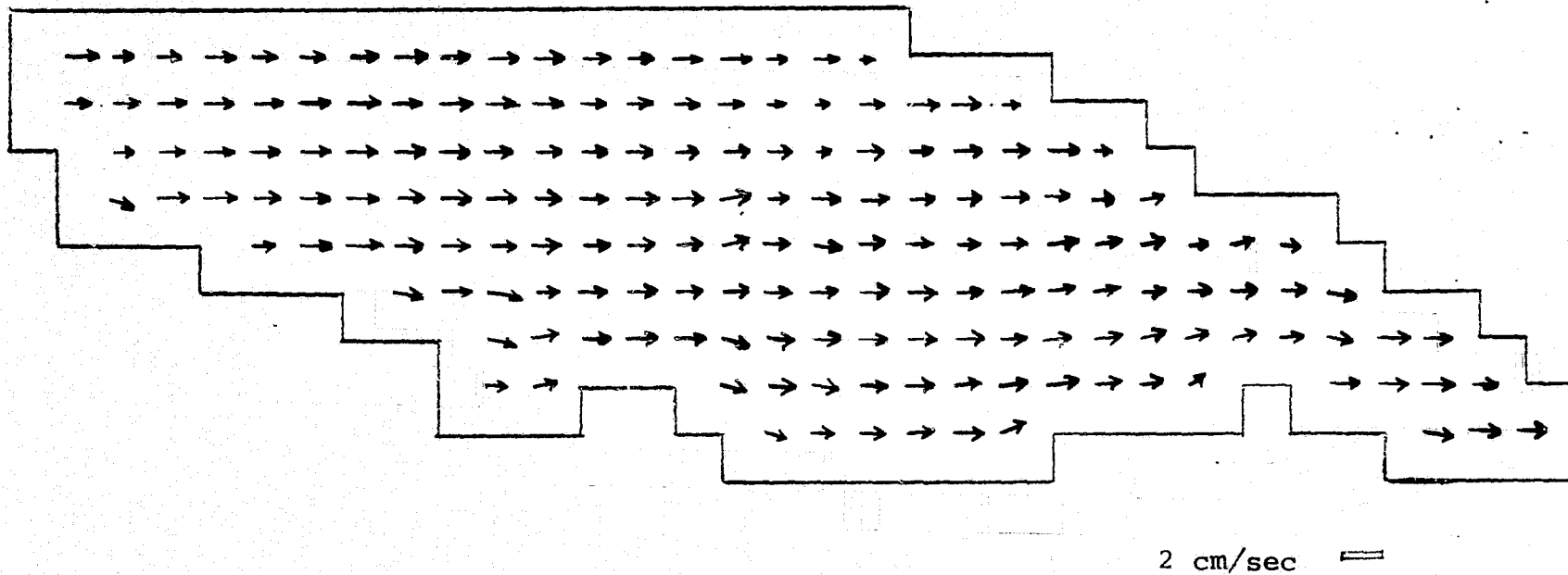
Fig. IV-10. Surface Velocities in Biscayne Bay With Wind From the North

.8 Kilometers

Wind Stress .1 dynes/cm^2

2 cm/sec
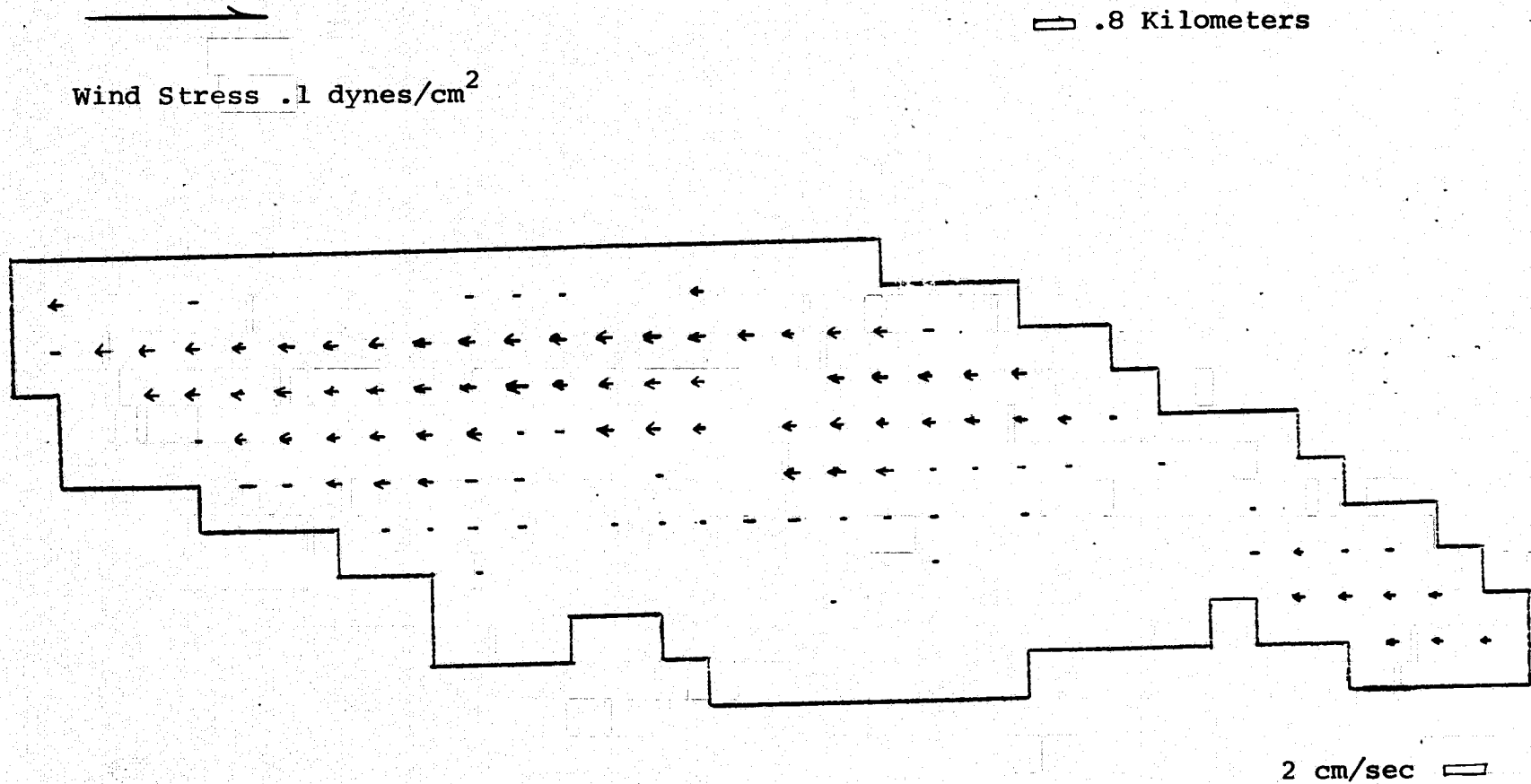
Fig. IV-11. Velocities at a Depth of 2 Meters With Wind From the North
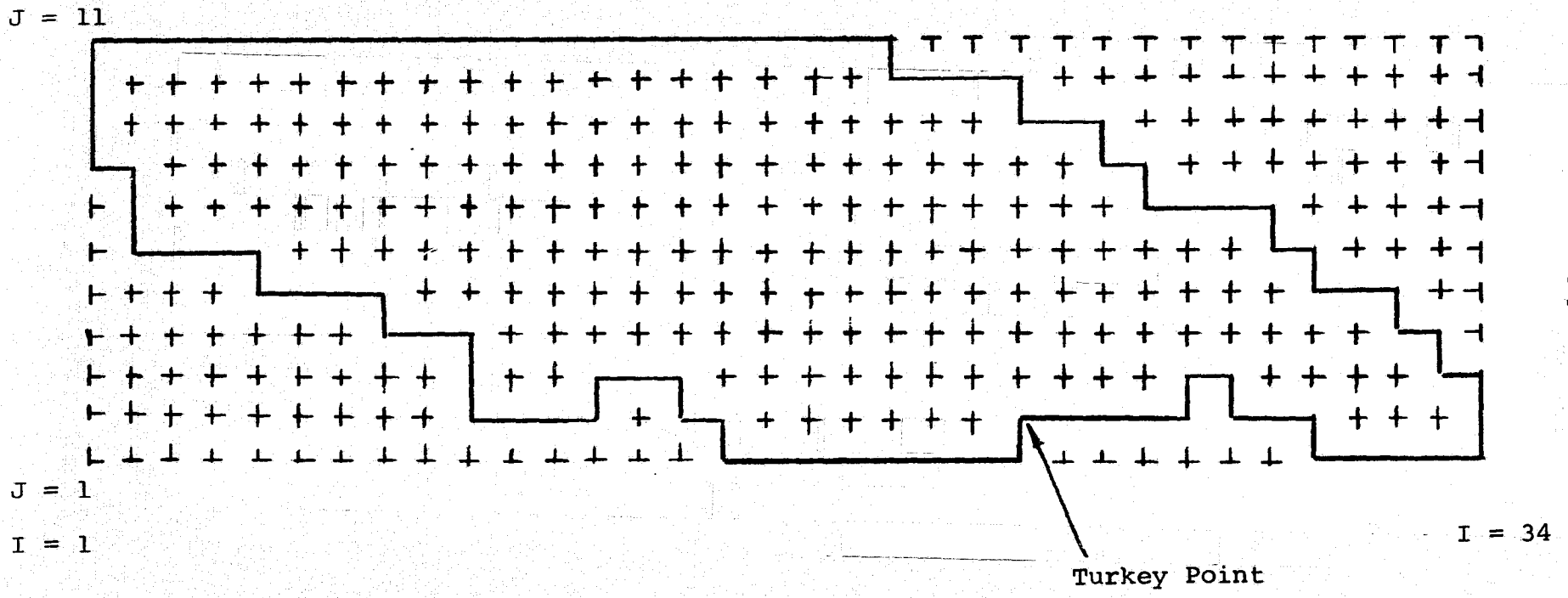
Fig. IV-12. Horizontal Grid System for Biscayne Bay

Wind Stress = .1 dynes/cm^2

.8 kilometers horizontal scale

3 ft. vertical scale

2 cm/sec

A
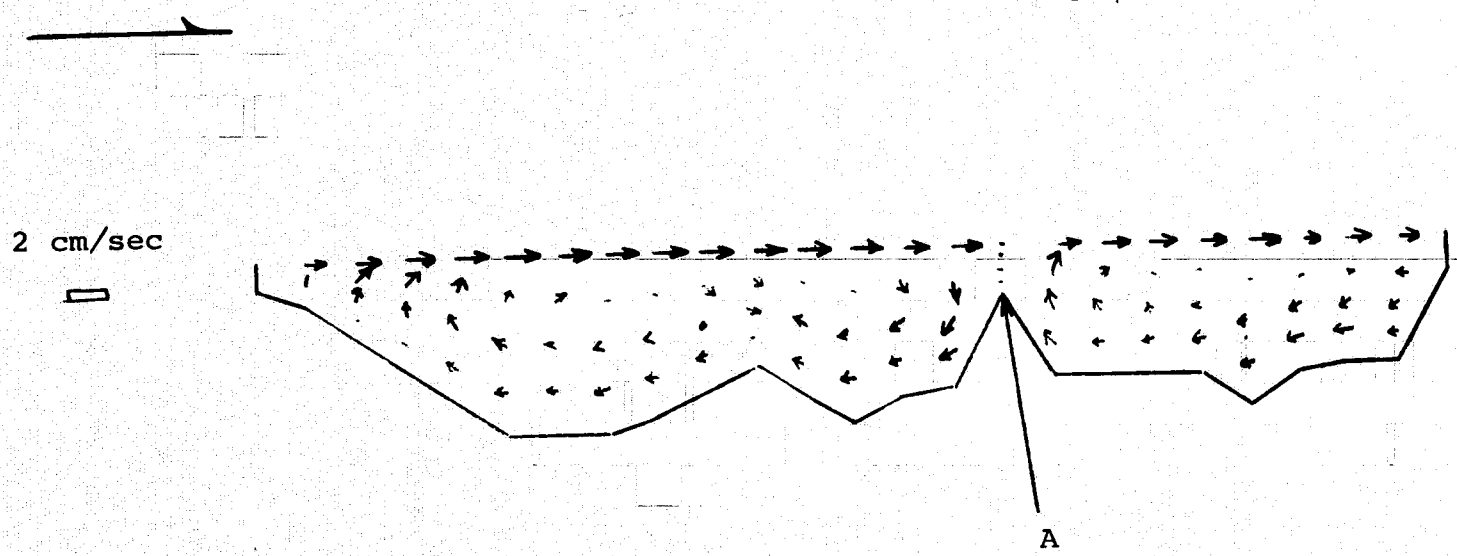
Fig. IV-13. Velocities for Section J = 7 With Wind From the North

Wind Stress = .1 dynes/cm^2

.8 kilometers

2 cm/sec
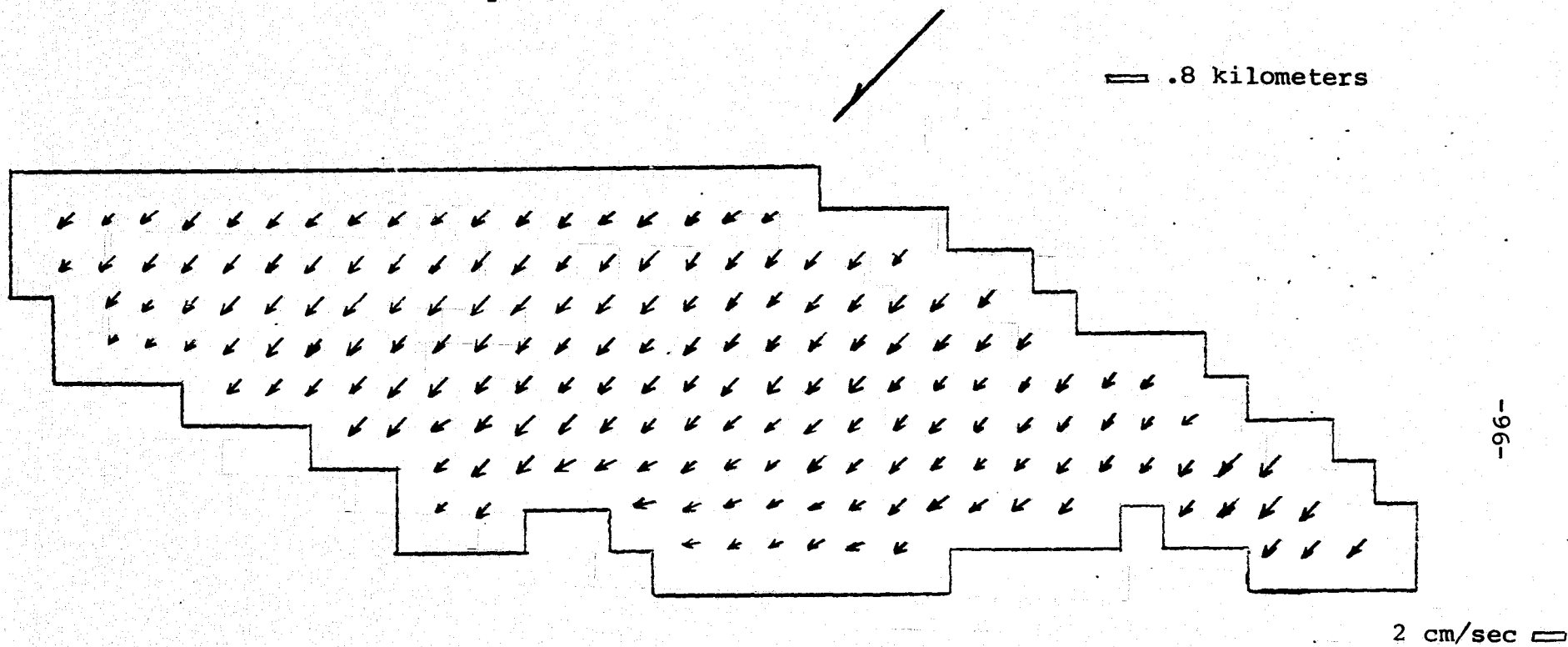
Fig. IV-14.   Surface Velocities With Wind From the Southeast

Fig. IV-15. Velocities at a Depth of 2 Meters With Wind From the Southeast

Wind Stress .0707 dynes/cm^2

.8 kilometers horizontal scale

3 ft. vertical scale

A
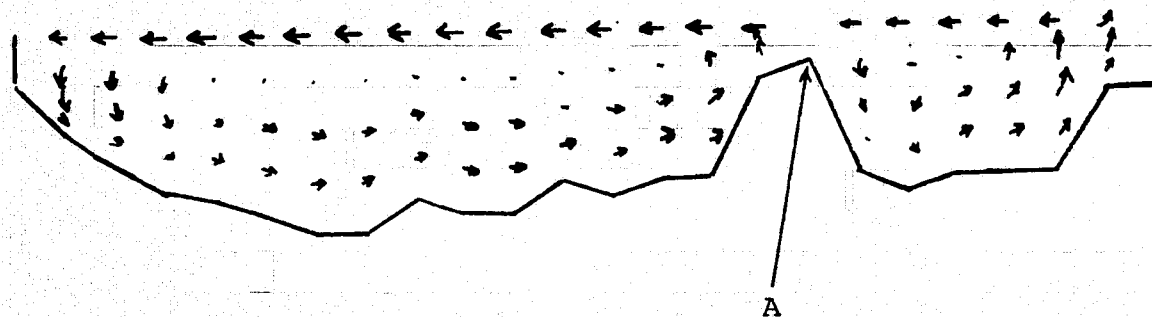
Horizontal scale 2 cm/sec

Vertical Scale .001 cm/sec

Fig. IV-16. Velocities for Section J = 8 With Wind From the Southeast

.8 kilometers

-99-

2 cm/sec
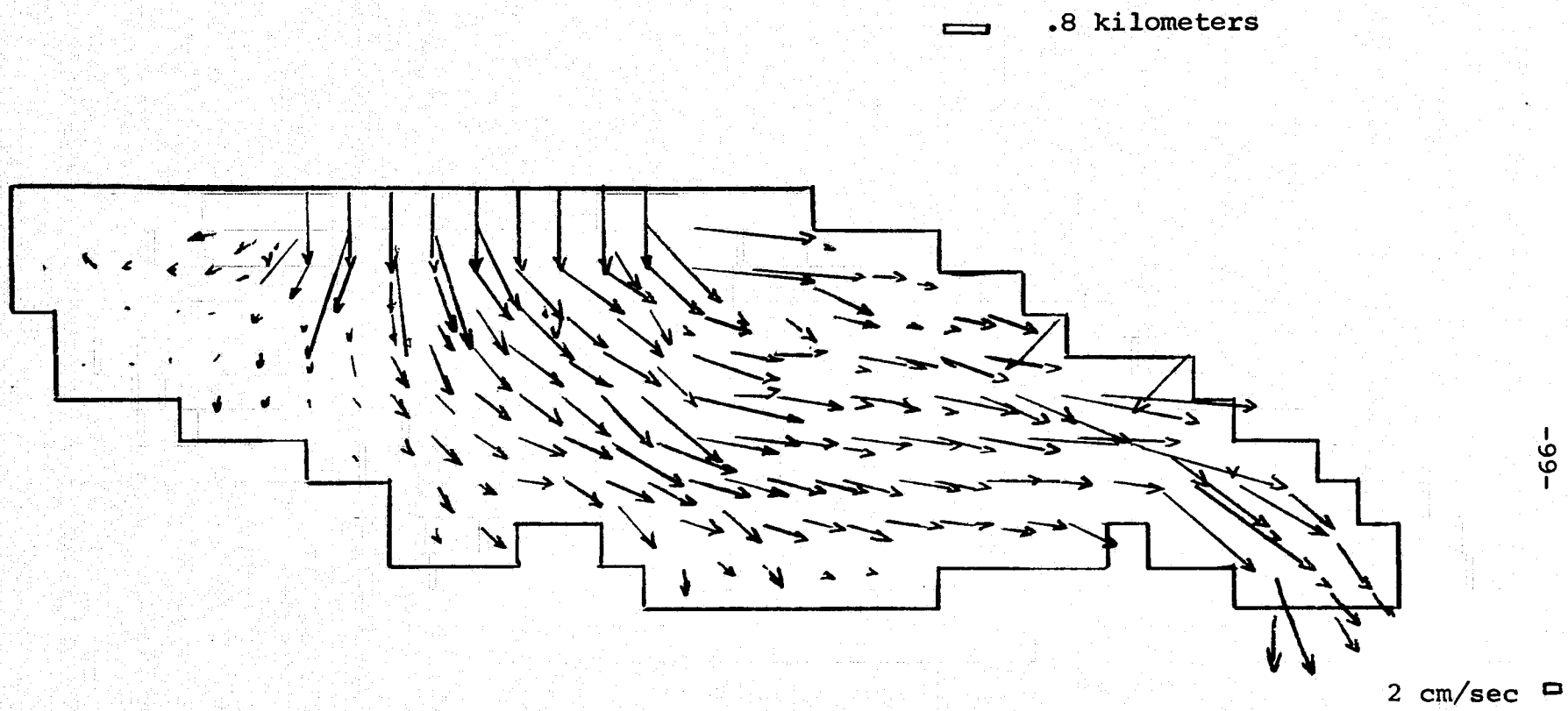
Fig. IV-17. Surface Currents with Incoming Tide

in Biscayne Bay

.8 kilometers

2 cm/sec
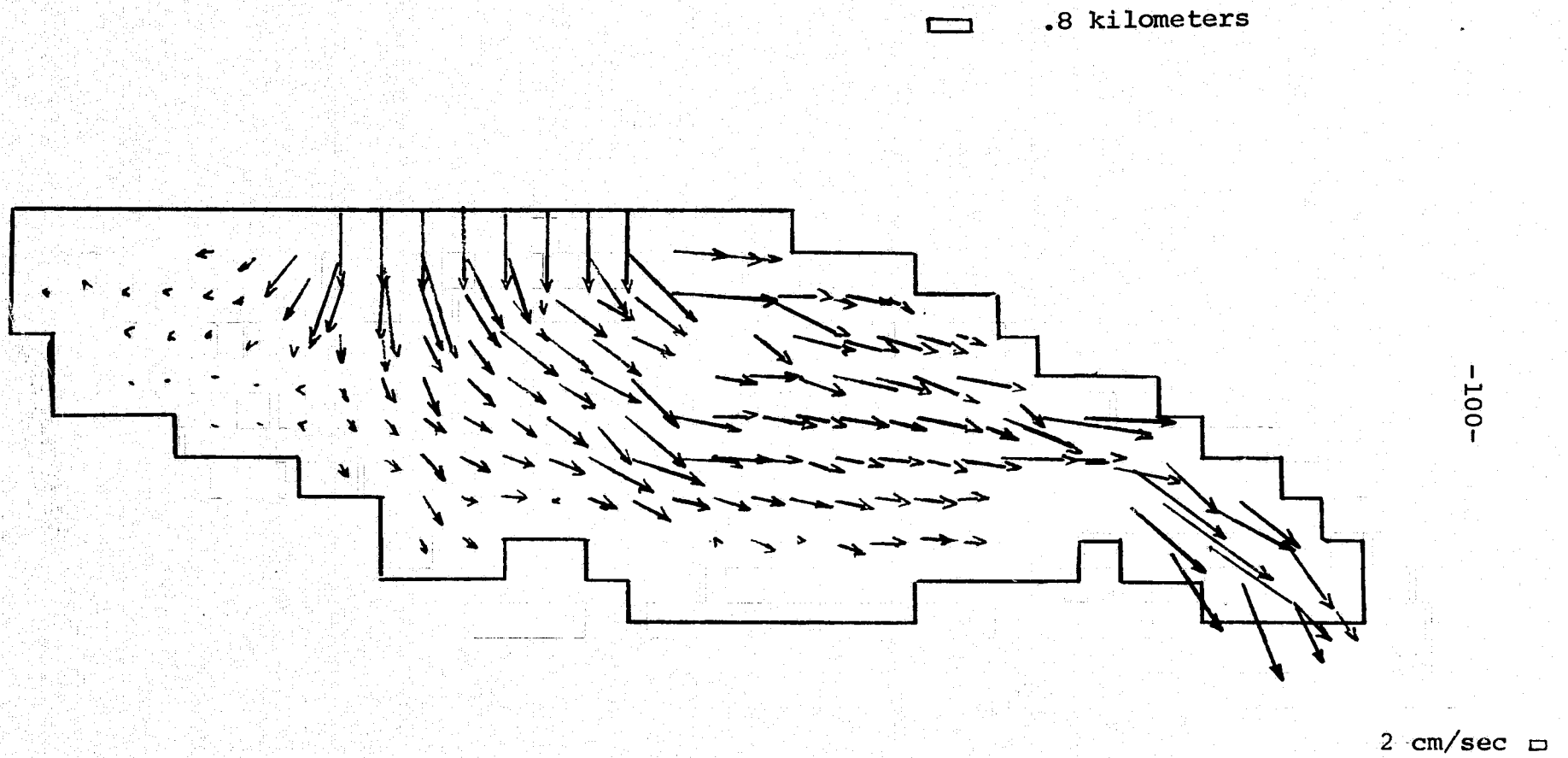
Fig. IV-18. Currents at 1 Meter Depth With Incoming Tide
into Biscayne Bay.

.8 kilometers

2 cm/sec
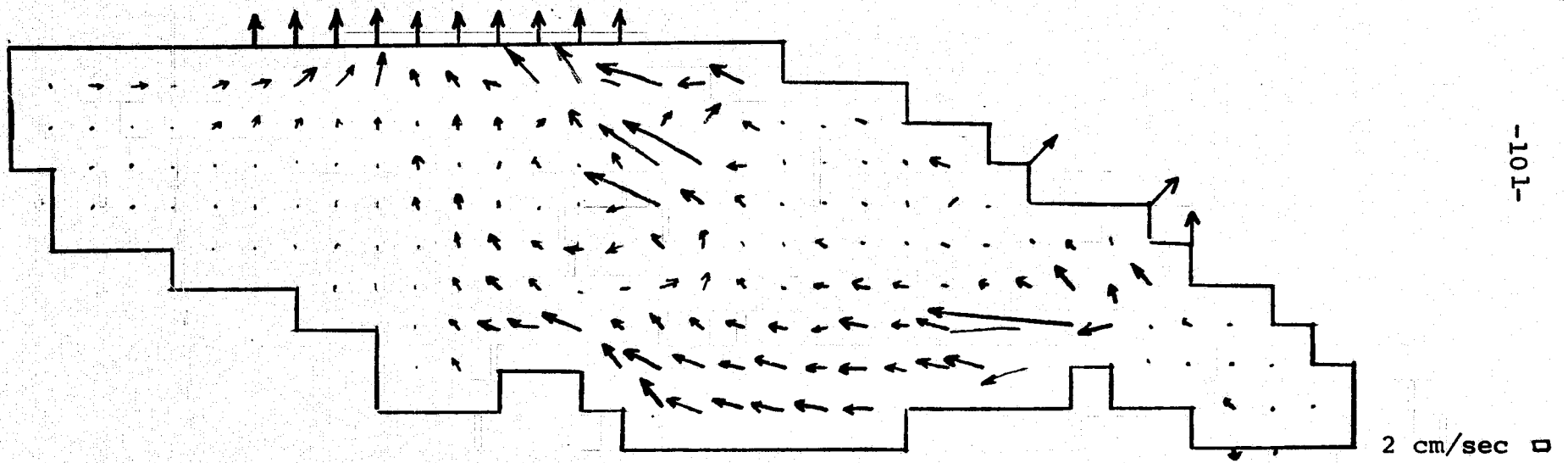
Fig. IV-19. Surface Currents During Tidal Flow Reversal in Biscayne Bay

.8 kilometers

2 cm/sec
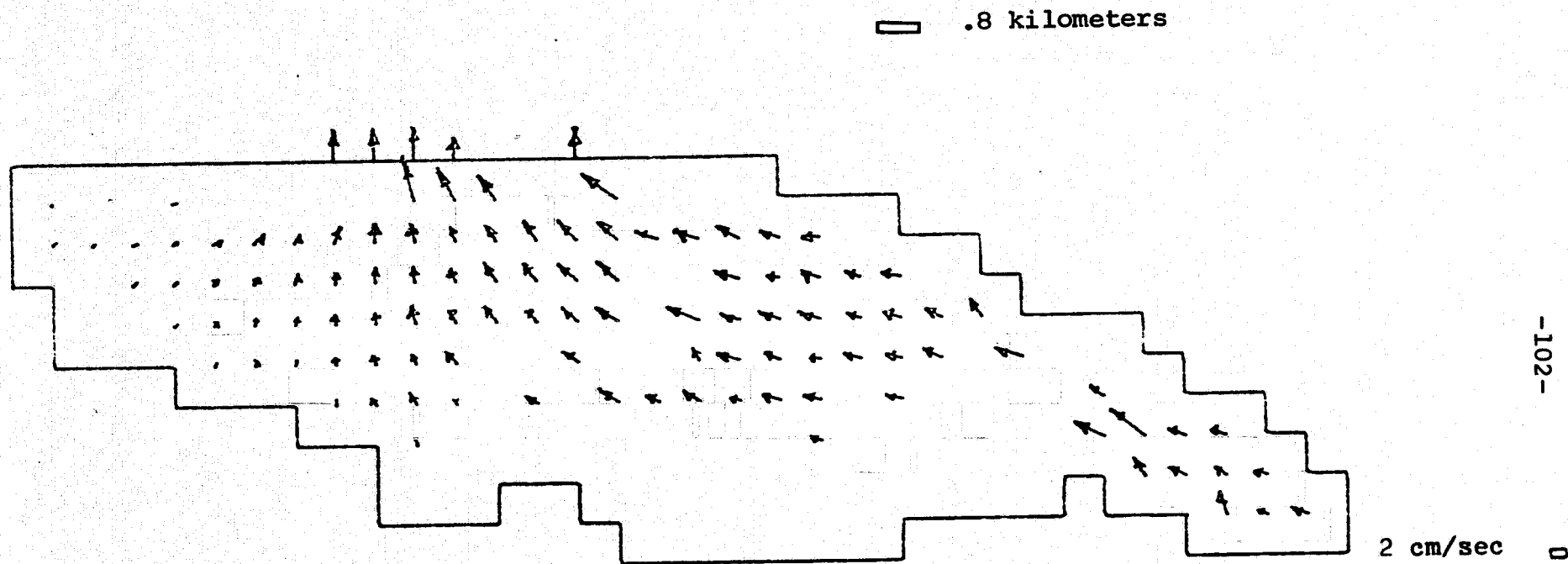
Fig. IV-20. Currents at 2 Meters Depth During Tidal Flow Reversal in Biscayne Bay
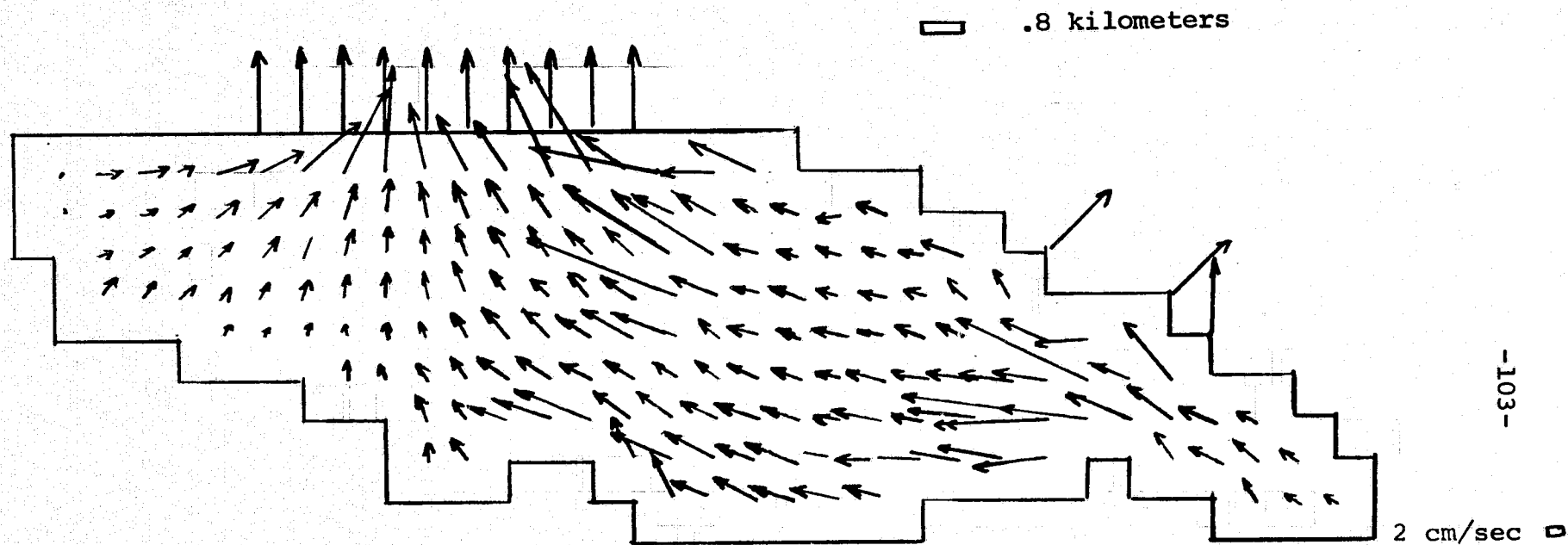
Fig. IV-21. Surface Currents for Ebb Tide in Biscayne Bay to Ocean
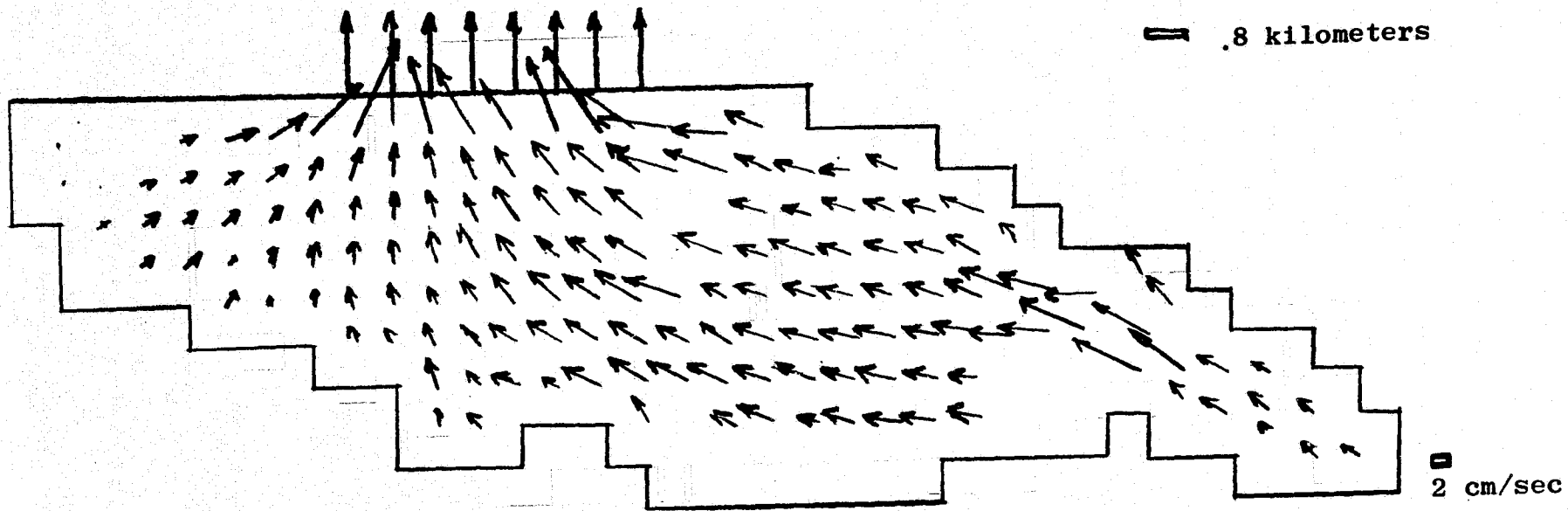
Fig. IV-21a. Currents at a Depth of 1 meter for Ebbtide from Biscayne Bay to the ocean.

.8 kilometers

WIND: 10 MPH Southeast

Incoming Tide With a Velocity of 10 cm/sec.

2 cm/sec.
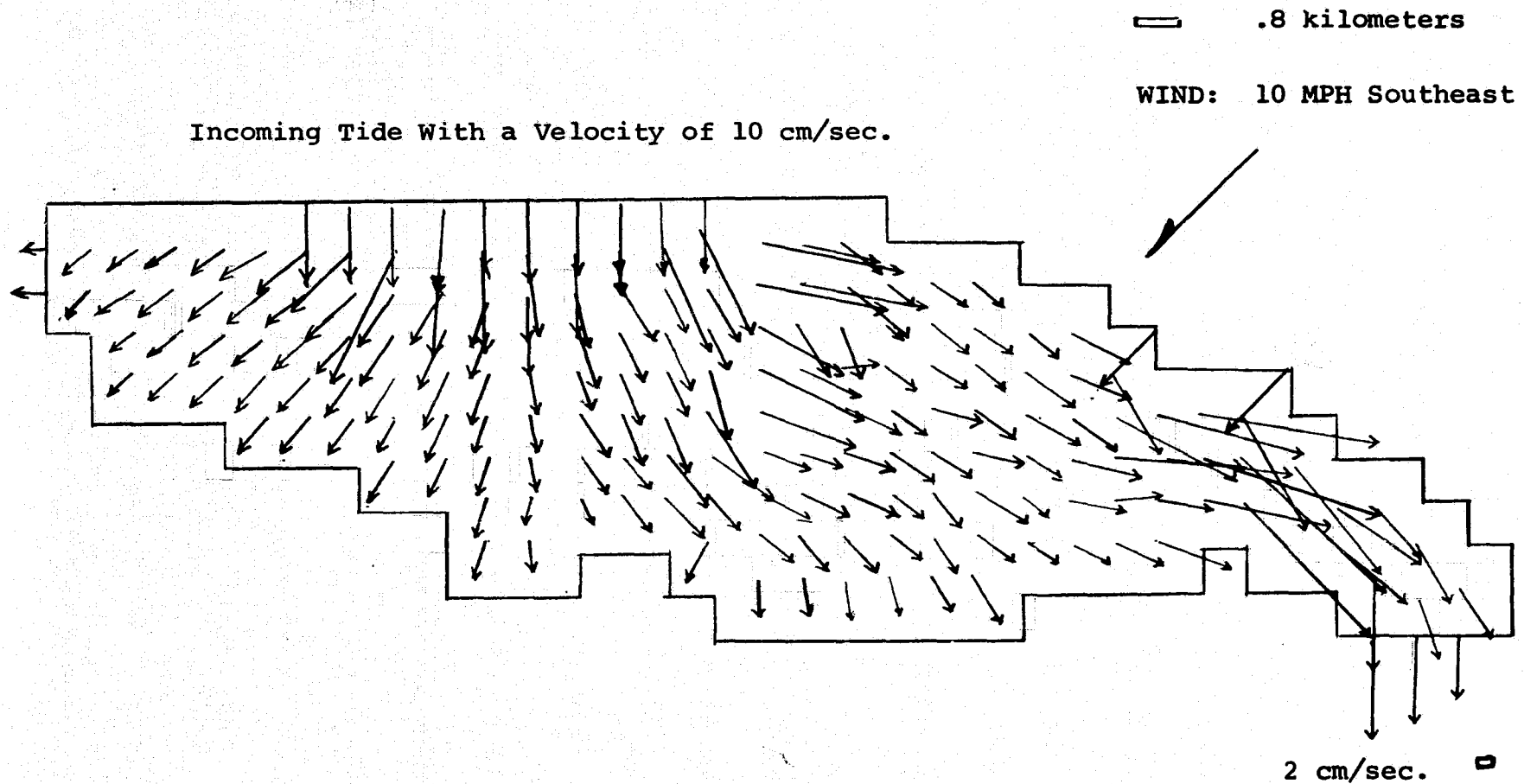
Fig. IV-22. Surface Velocities
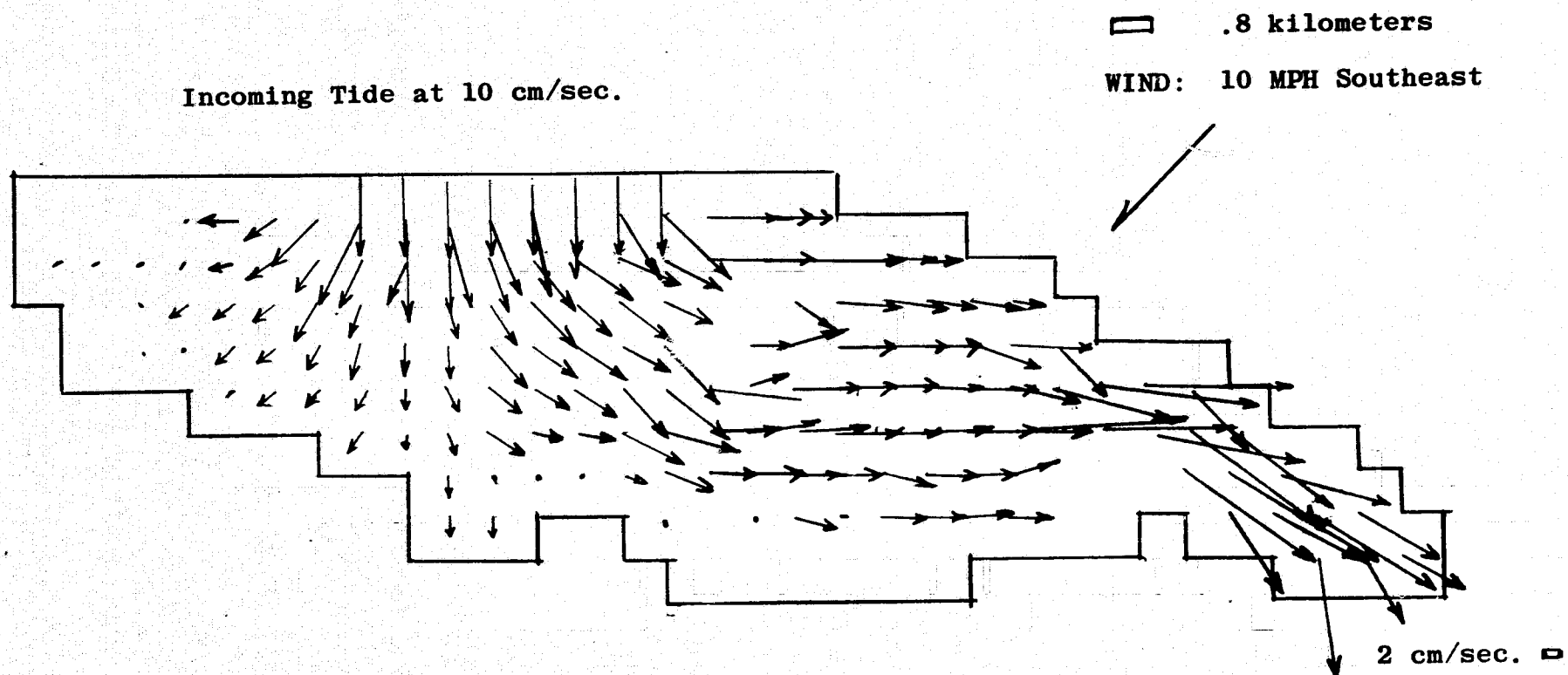
Fig. IV-23. Velocities at a Depth of 1 Meter

.8 Kilometers

Incoming Tide at 10 m/ sec.

WIND: 10 MPH Southeast

2 cm/sec.
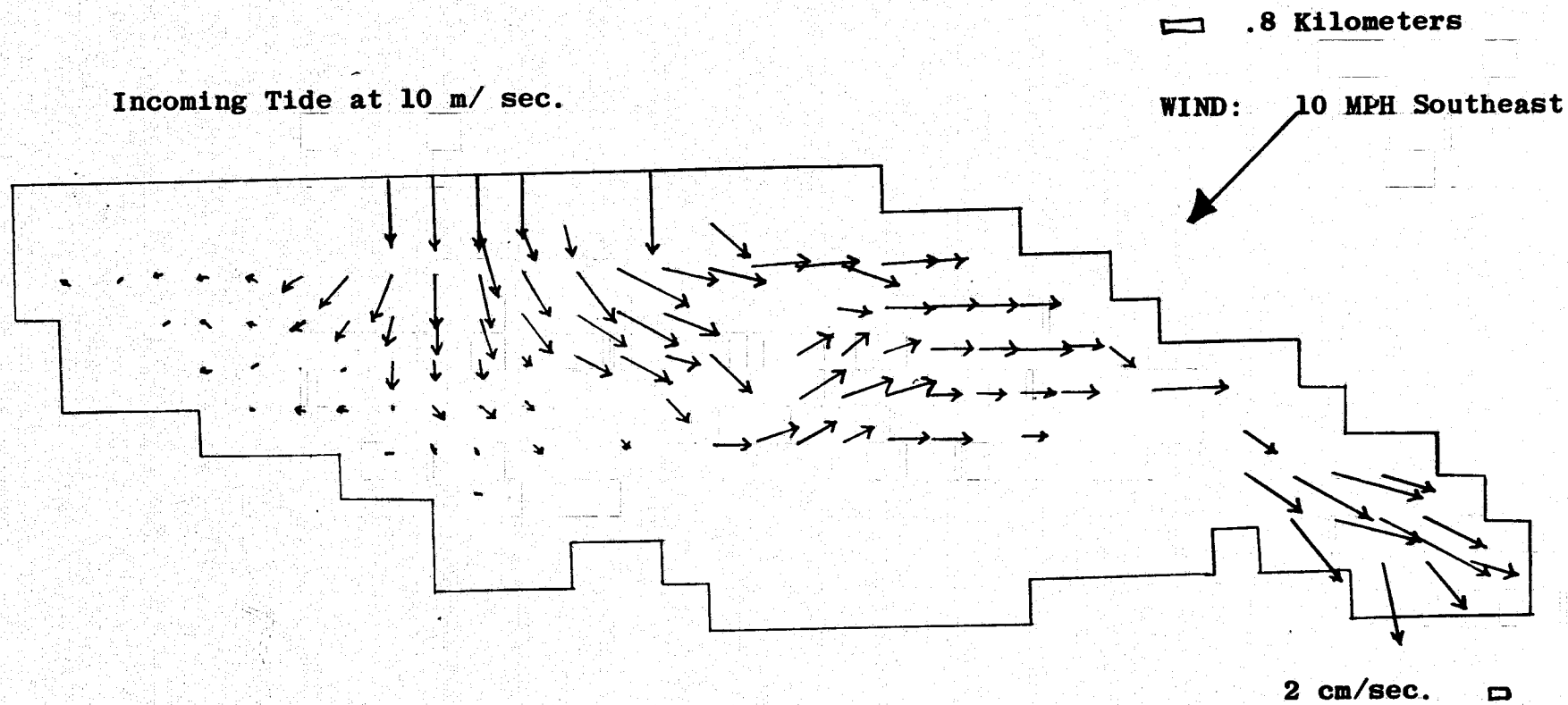
Fig. IV-24.   Velocities at a Depth of 2 Meters
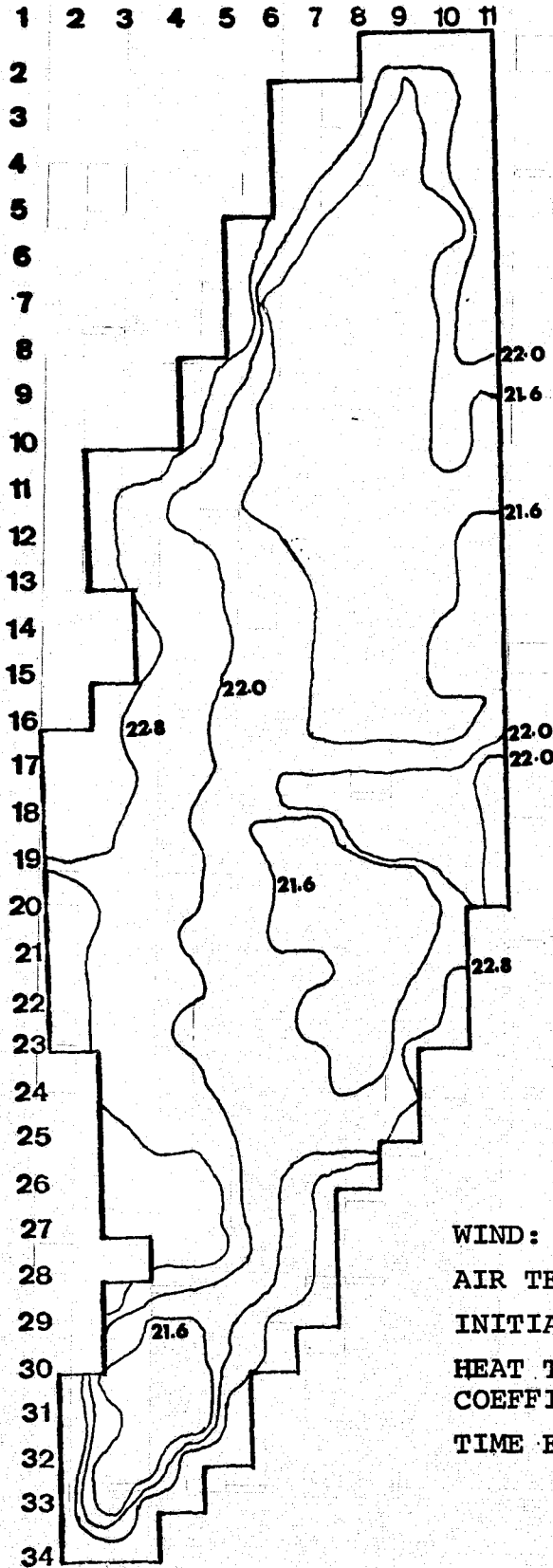
Surface Isotherms For Biscayne Bay
(Rigid-Lid Model)

Fig. IV-25.
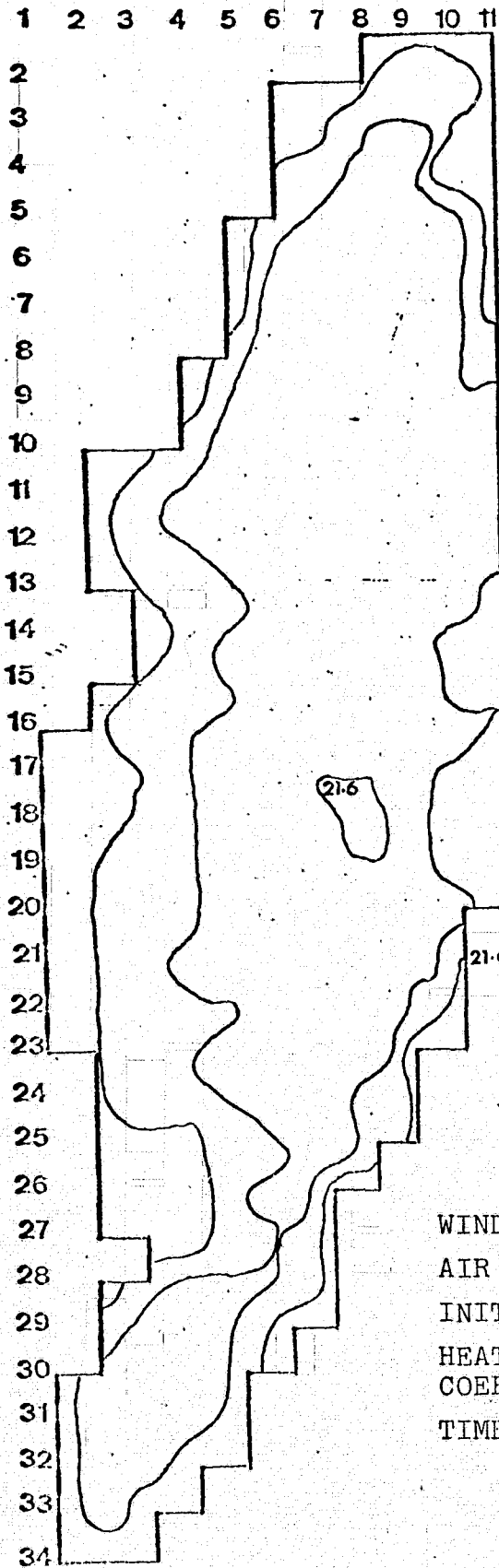
Surface Isotherms for Biscayne Bay
(Rigid-Lid Model)
Fig. IV-26

Surface Isotherms for Biscayne Bay
(Rigid-Lid Model)

Fig. IV-27.

Surface Isotherms for Biscayne Bay
(Rigid-Lid Model)
Fig. IV-28.

WIND: 10 MPH Southeast

AIR TEMP: 29°C

INITIAL TEMP: 20°C
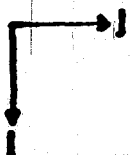
⊏⊐ .8 kilometers horizontal scale

⊏⊐ 3 ft. vertical scale
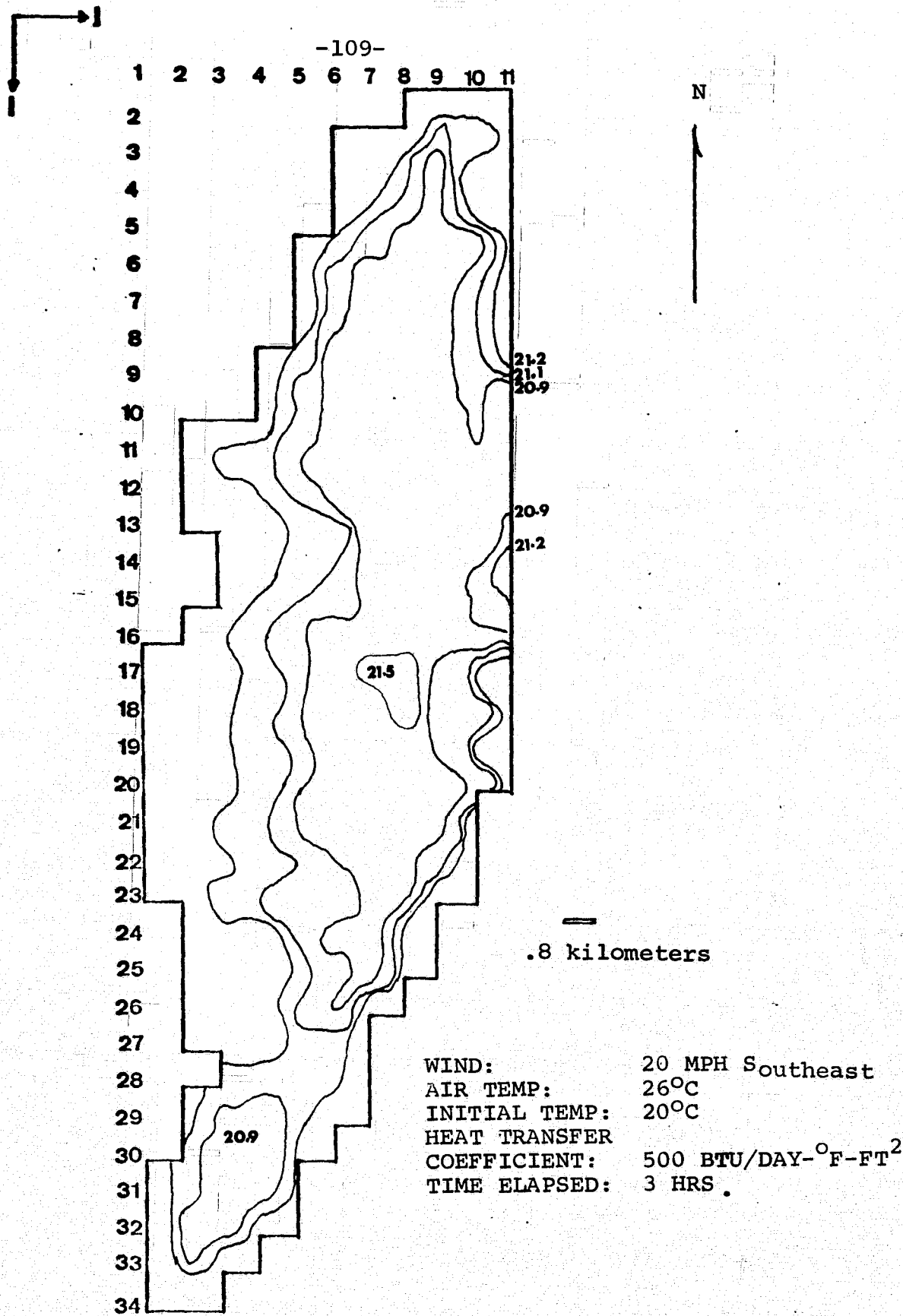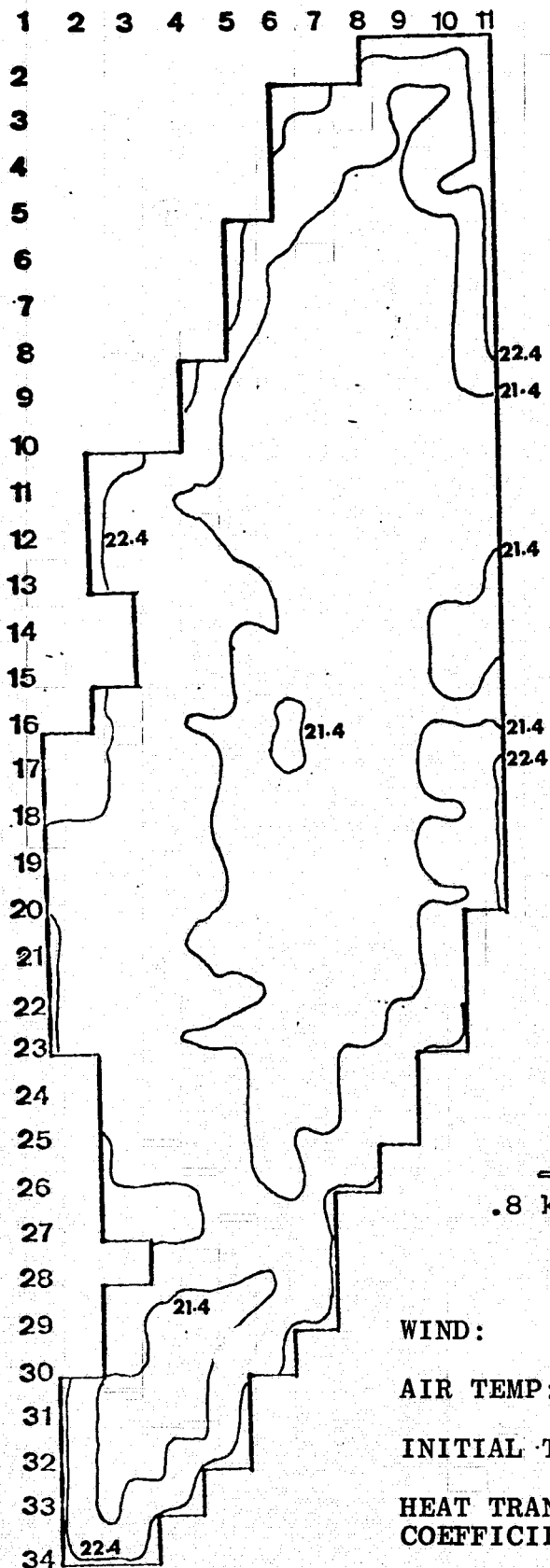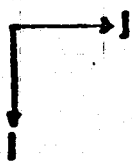
HEAT TRANSFER
COEFFICIENT: 1000 BTU/DAY-^{O}F-FT^{2}

TIME ELAPSED: 1 HR.
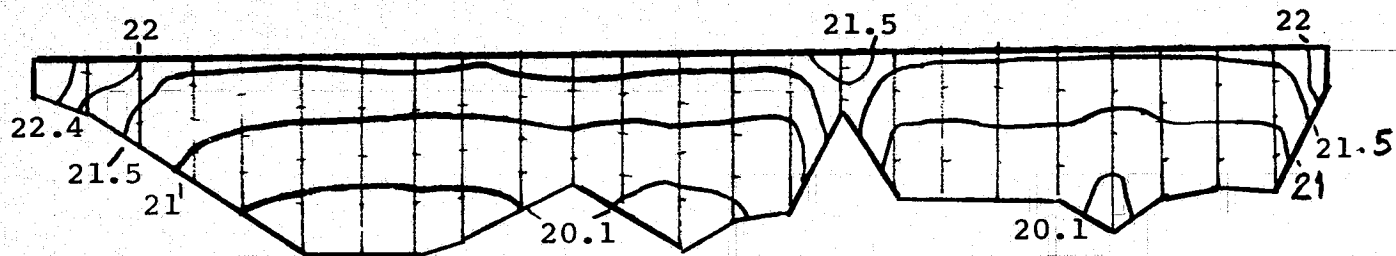
Isotherms For Vertical Section J=7

Fig. IV-29.
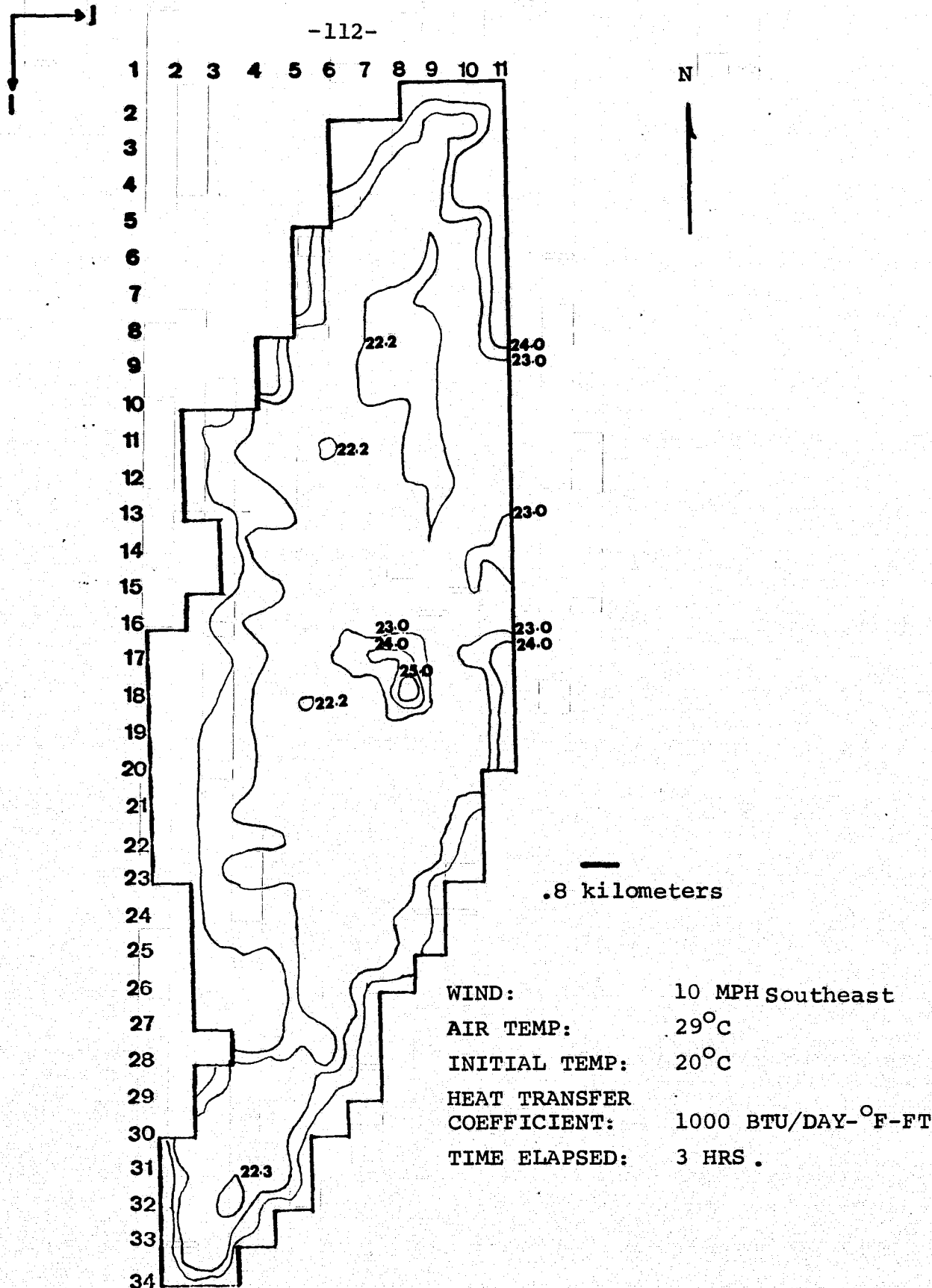
Surface Isotherms for Biscayne Bay
(Rigid-Lid Model)
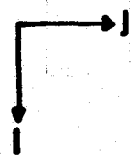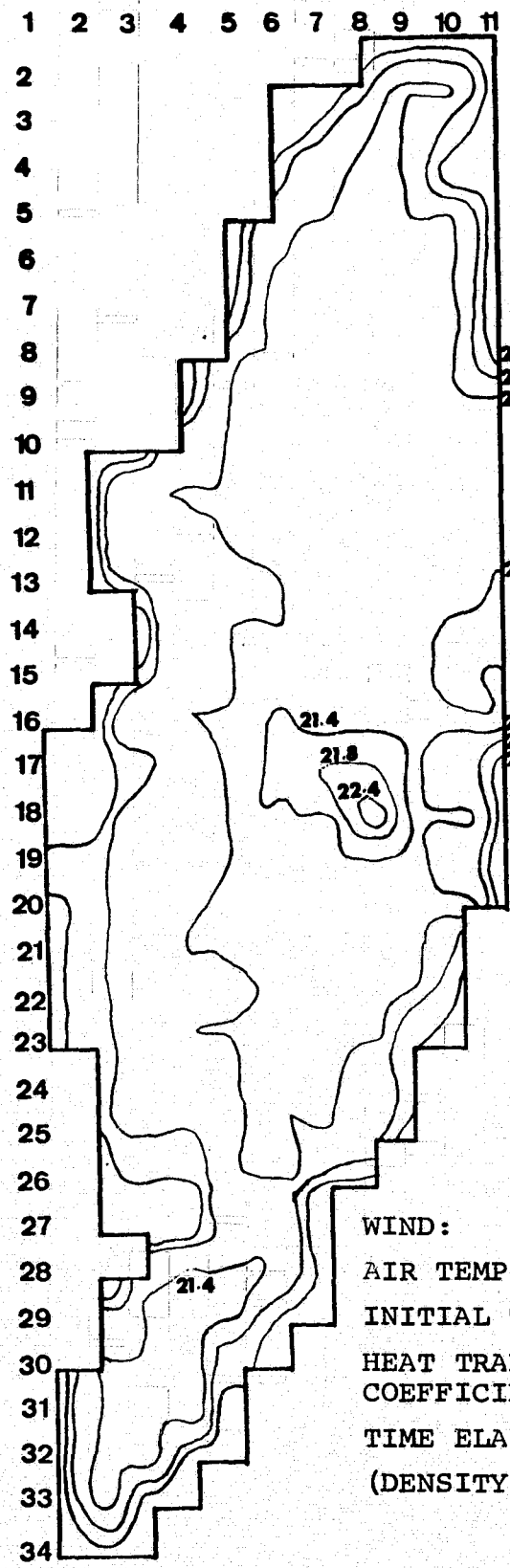
Fig. IV-30

.8 kilometers

WIND: 10 MPH Southeast

AIR TEMP: 29°C

INITIAL TEMP: 20°C

HEAT TRANSFER
COEFFICIENT: 1000 BTU/DAY-°F-FT^2

TIME ELAPSED: 1 HR.

(DENSITY EFFECTS INCLUDED)

Surface Isotherms for Biscayne Bay
(Rigid-Lid Model)

Fig. IV-31

WIND: 10 MPH Southeast

AIR TEMP: 29°C

INITIAL TEMP: 20°C

HEAT TRANSFER
COEFFICIENT: 1000 BTU/DAY-°F-FT^2

TIME ELAPSED: 1 HR.

DENSITY EFFECTS INCLUDED

⬜ .8 kilometers horizontal scale

⬜ 3 ft. vertical scale

Isotherms for Vertical Section J=7

Fig. IV-32

Surface Isotherms for Biscayne Bay
(Rigid-Lid Model)

Fig. IV-33

Surface Isotherms for Biscayne Bay
(Rigid-Lid Model)

Fig. IV-34

Surface Isotherms for Biscayne Bay

(Rigid-Lid Model)
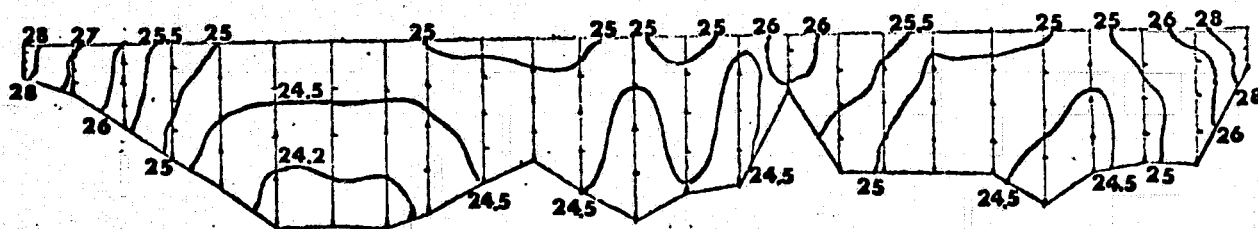
Fig. IV-35

WIND: 10 MPH Southeast

AIR TEMP: $30^{\circ}C$ ⊏⊐ .8 kilometers horizontal scale

INITIAL TEMP: $23^{\circ}C$ ⊏⊐ 3 ft. vertical scale

HEAT TRANSFER
COEFFICIENT: 750   BTU/DAY-$^{\circ}$F-FT^2

TIME ELAPSED: 6 HRS.

Isotherms For Vertical Section J=7

Fig. IV-36
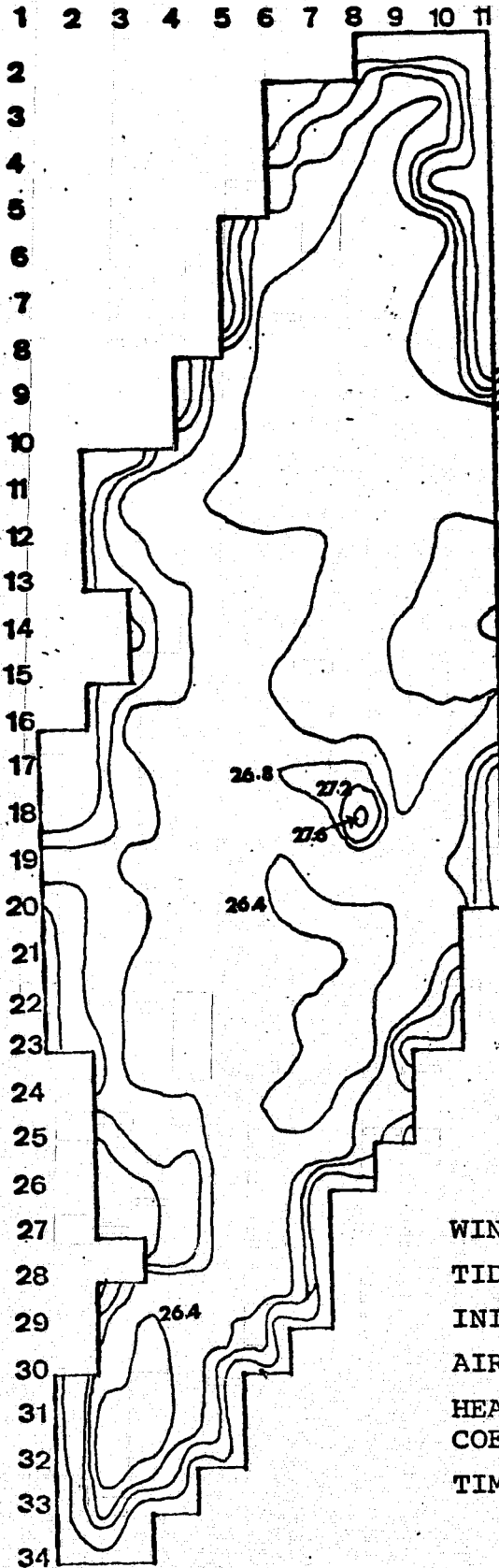
WIND: 10 MPH Southeast

TIDE: Incoming (10 cm/sec)

INITIAL TEMP: 25.5°C

AIR TEMP: 30°C

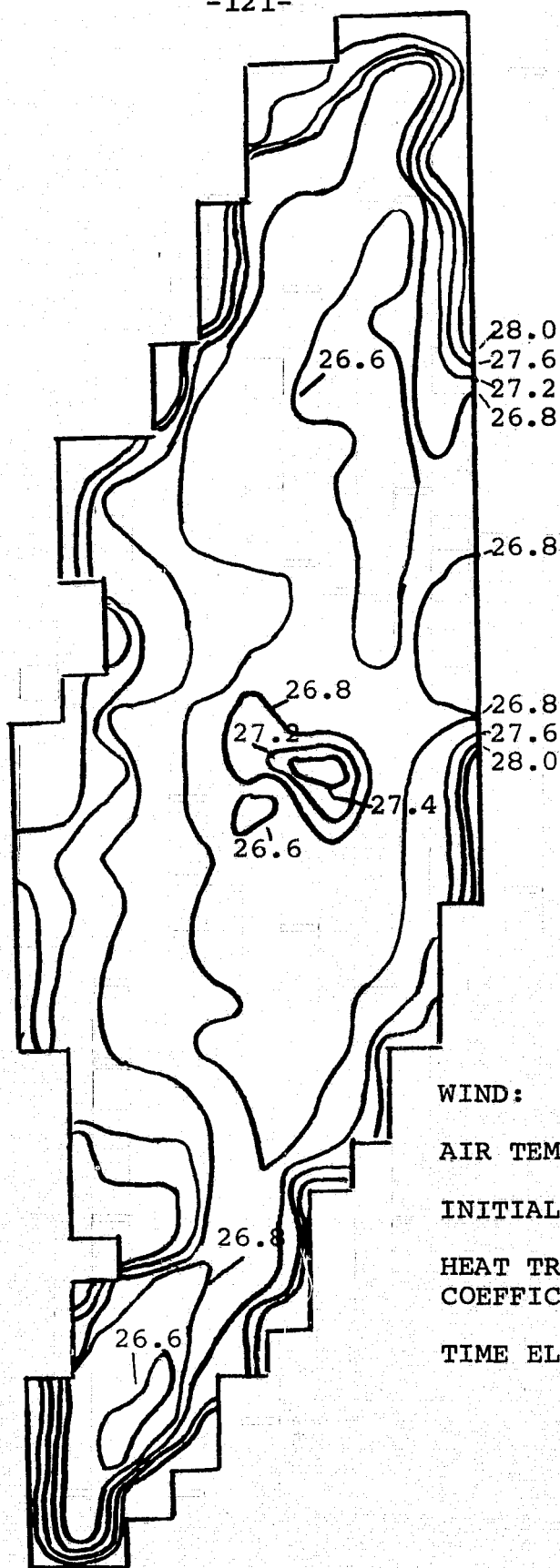HEAT TRANSFER COEFFICIENT: 750 BTU/DAY°F-FT²

TIME ELAPSED: 3 HRS.

Surface Isotherms for Biscayne Bay
(Rigid-Lid Model)
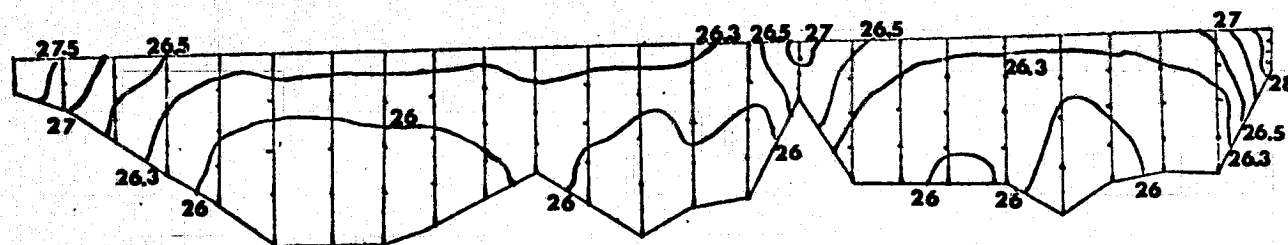
Fig. IV-37

WIND :   10 MPH Southeast

AIR TEMP :   30°C   ☐ .8 kilometers horizontal scale

INITIAL TEMP : 25.5°C   ☐ 3 ft. vertical scale

HEAT TRANSFER
COEFFICIENT : 750 BTU/DAY-°F-FT^2

TIDE :   Incoming (10 cm/sec)

TIME ELAPSED : 3 HRS.

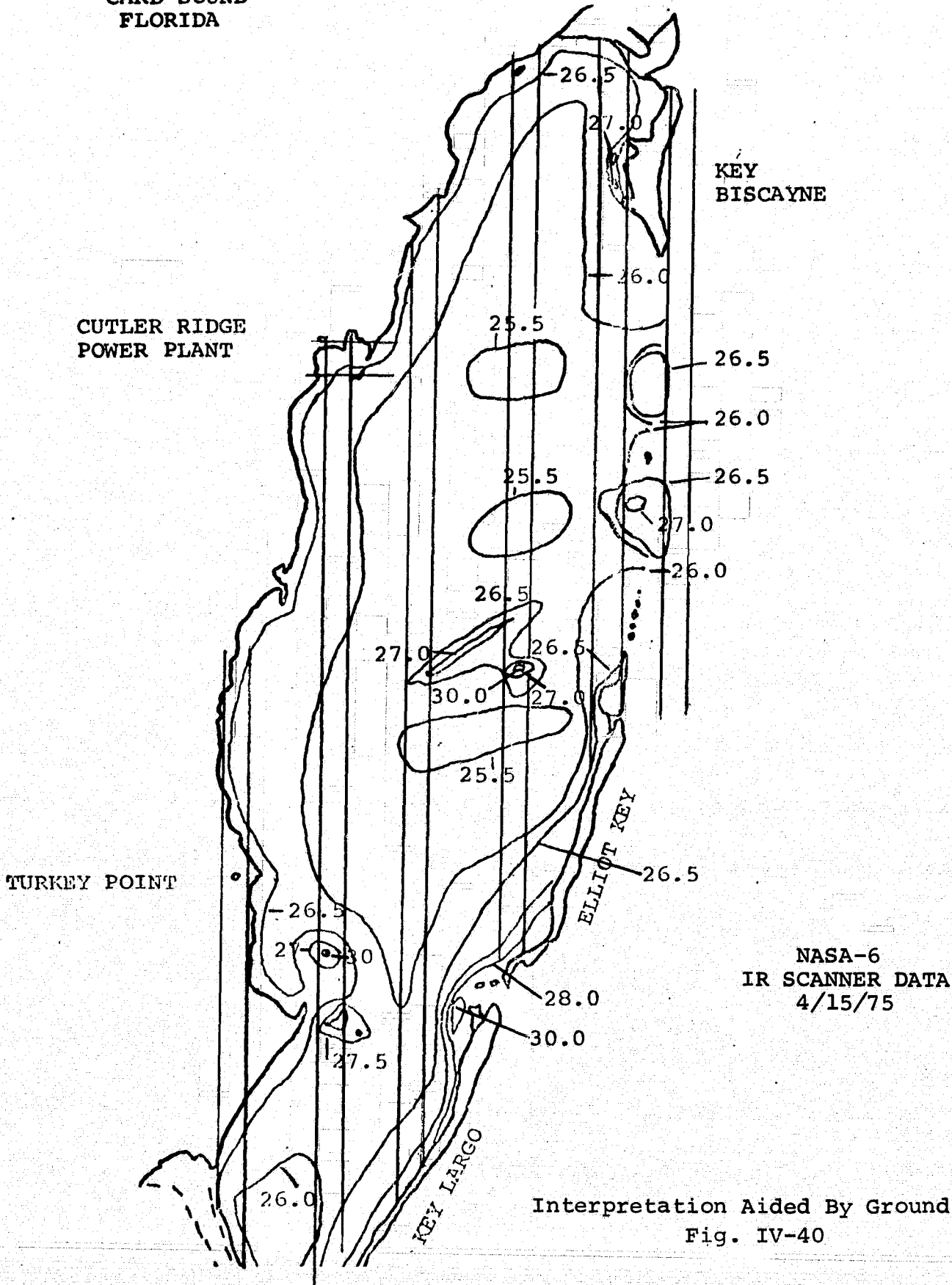Isotherms for Vertical Section J=7

Fig.IV- 38

N

28.0
27.6
27.2
26.8
26.6

26.8

26.8

27.2

26.8
27.6
28.0

27.4

26.6

26.8

26.8

26.6

.8 kilometers

WIND: 10 MPH Southeast

AIR TEMP: 30°C

INITIAL TEMP: 25.5°C

HEAT TRANSFER
COEFFICIENT: 1000 BTU/DAY-$^{\circ}$F-FT^2

TIME ELAPSED: 3 HRS.

Surface Isotherms for Biscayne Bay
(Rigid-Lid Model)

Fig. IV-39.

BISCAYNE BAY
AND
CARD SOUND
FLORIDA

KEY
BISCAYNE

-26.5

27.0

26.0

CUTLER RIDGE
POWER PLANT

25.5

26.5

26.0

25.5

26.5

27.0

26.0

26.5

27.0   26.5

30.0   27.0

25.5

ELLIOT KEY

TURKEY POINT

26.5

-26.5

27   30

28.0

NASA-6
IR SCANNER DATA
4/15/75

30.0

27.5

KEY LARGO

26.0

Interpretation Aided By Ground Truth
Fig. IV-40

N

27.0
26.5
26.0
27.0
26.0
27.0
26.0
26.5
26.0
27.0
26.0
27.0
26.0
26.0
26.5
26.5
27.0
27.0
27
27.0
27.0
26.5 26.0
27.0
26.0
27.0
27.0
26.0
27.0
27.5
27.0
27.5
27.5
25.5

.8 kilometers

WIND:	10 MPH., Southeast
TIDE:	Incoming (10 cm/ sec)
AIRTEMP:	30°C
INITIAL TEMP:	24.5°C
HEAT TRANSFER COEFFICIENT:	750 BTU/DAY$^{\circ}$F-FT^2
TIME ELAPSED:	3 HRS.
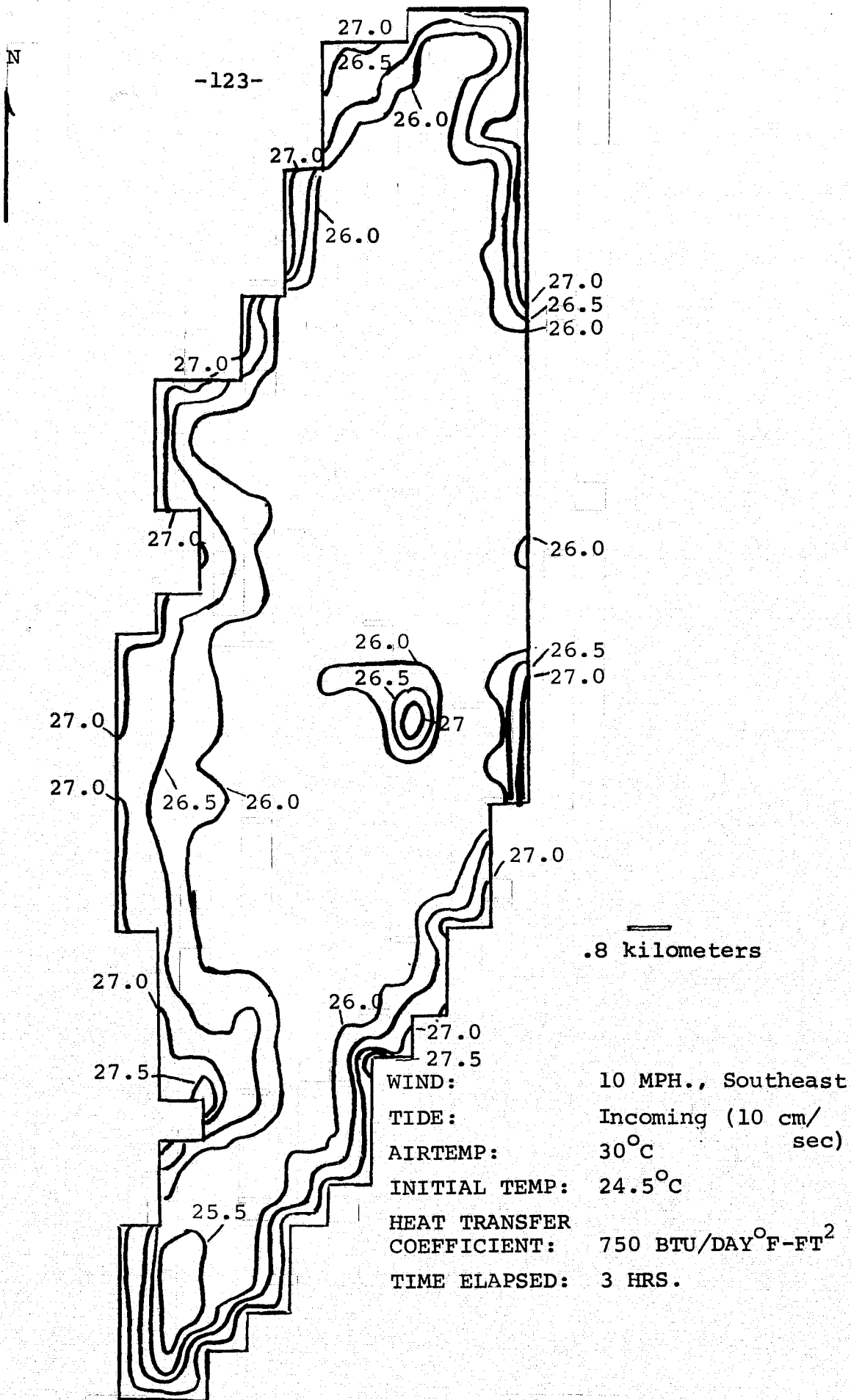
Fig. IV-41. Surface Isotherms for Biscayne Bay
(Rigid-Lid Model)

.8 kilometers horizontal scale

3 ft. vertical scale

26.5 26.0

27.0   25.5   26.0   25.5   26.0   27.5

25.0   25.0   25.0   25.0
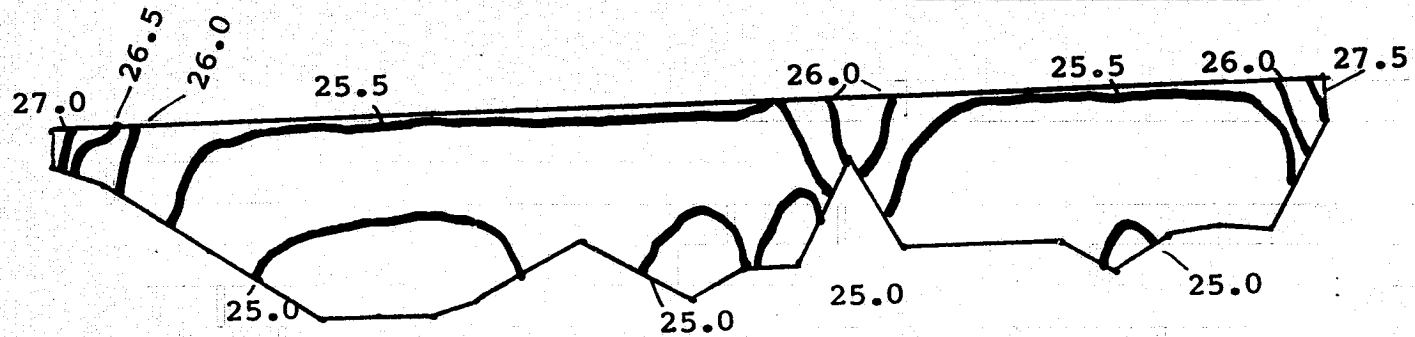
WIND: 10 MPH Southeast
TIDE: Incoming (10 cm/sec)
AIRTEMP: 70°C
INITIAL TEMP: 24.5°C
HEAT TRANSFER
   COEFFICIENT: 750BTO/DAY$^{\circ}$F-FT^2
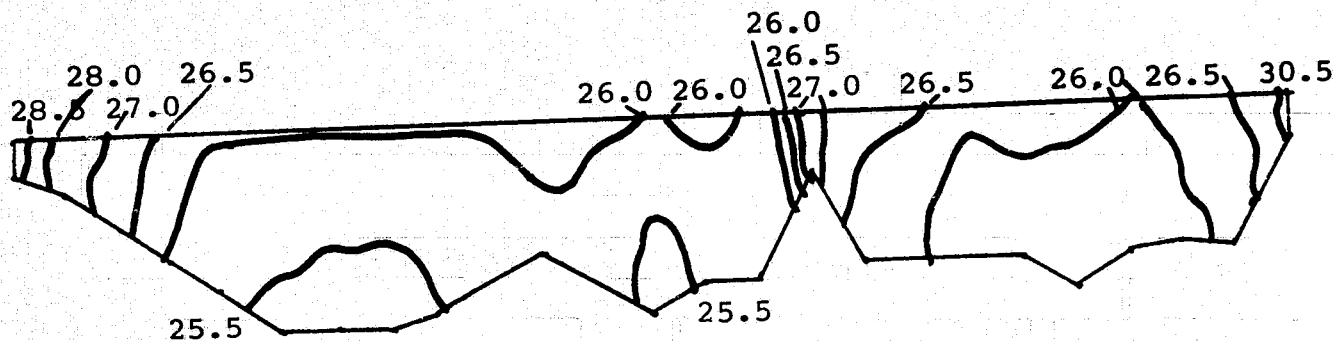TIME ELAPSED: 3 HRS.
SECTION: J=7

Isotherms for Section J=7

Fig. IV-42

BISCAYNE BAY

AND

CARD SOUND FLORIDA
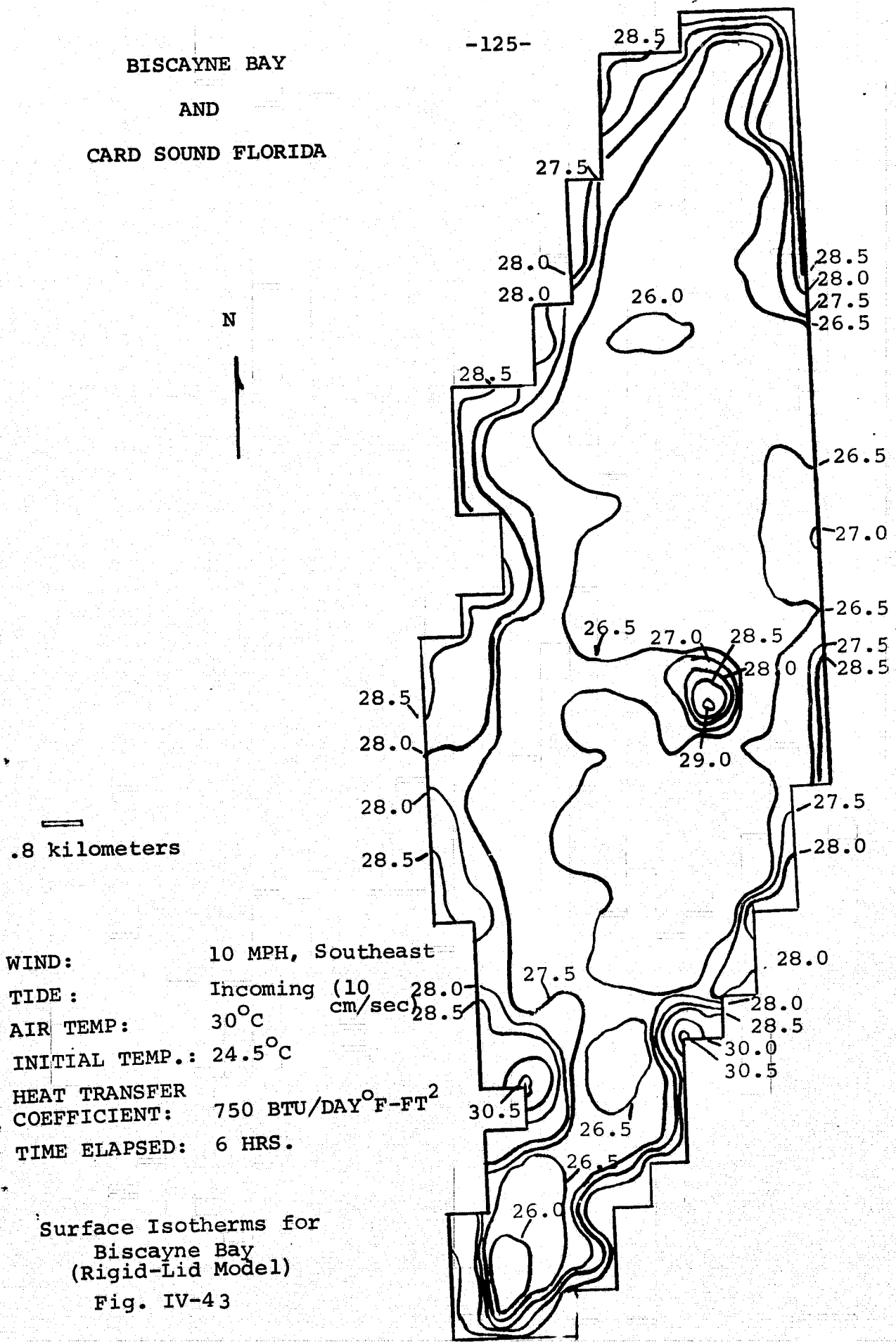
N

.8 kilometers

WIND: 10 MPH, Southeast

TIDE: Incoming (10 cm/sec)

AIR TEMP: $30^{o}C$

INITIAL TEMP.: $24.5^{o}C$

HEAT TRANSFER
COEFFICIENT: 750 BTU/DAY^{o}F-FT^{2}

TIME ELAPSED: 6 HRS.

Surface Isotherms for
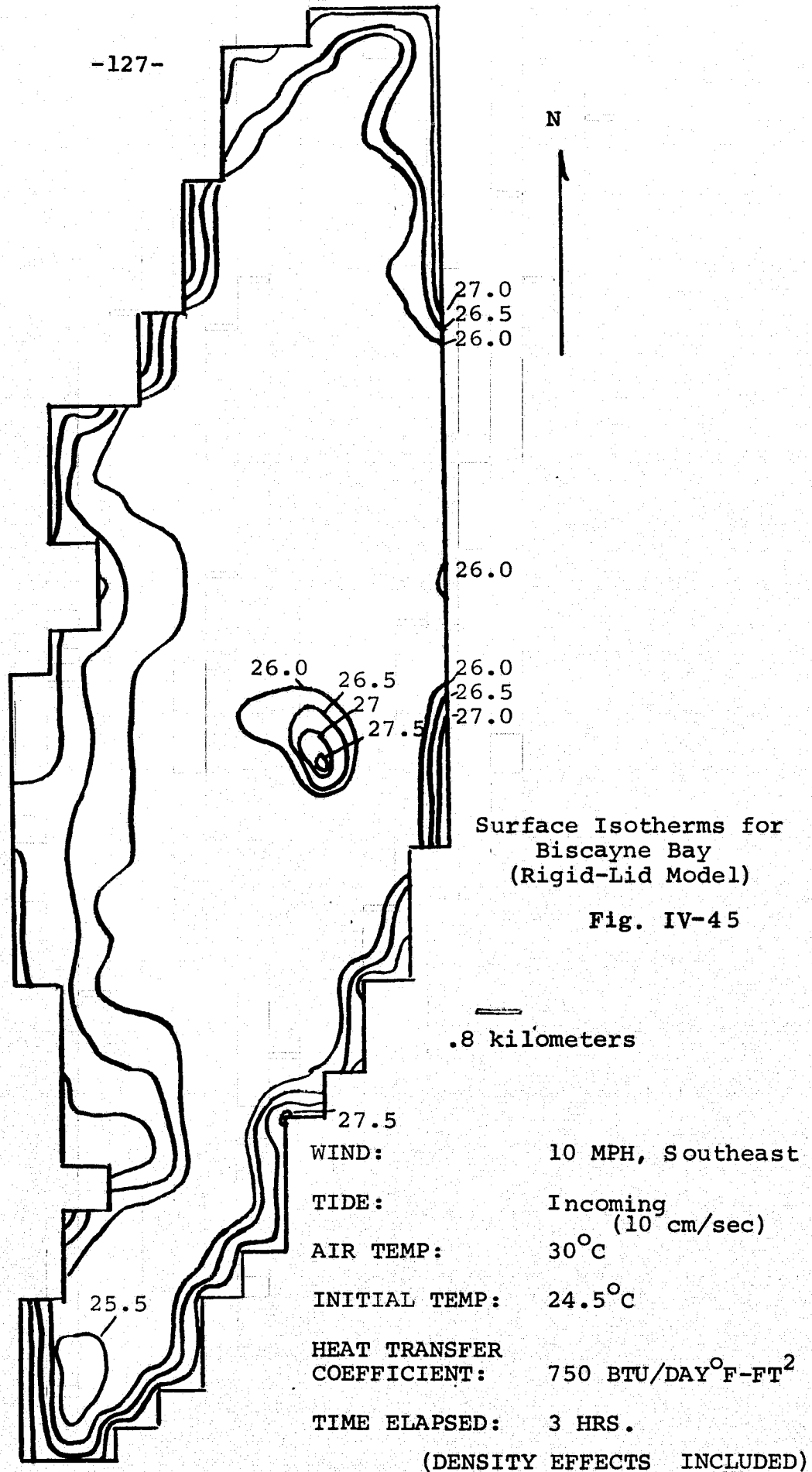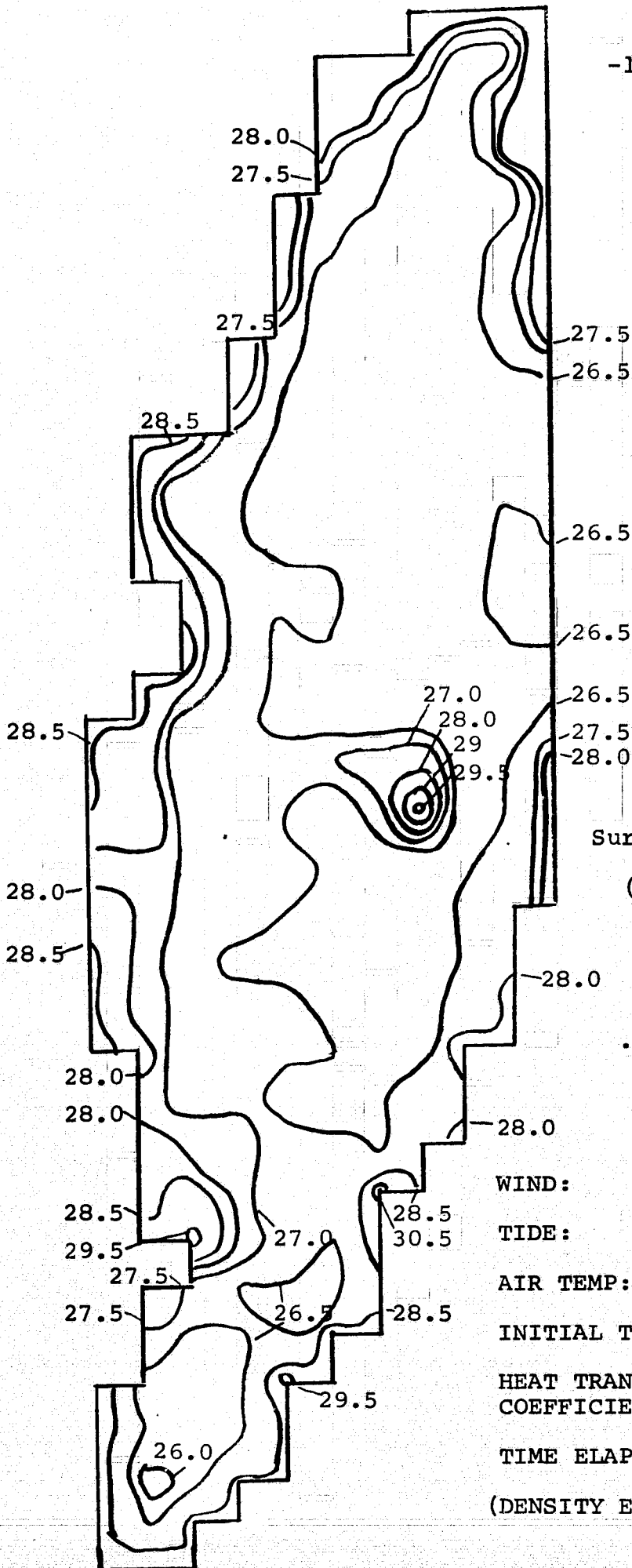Biscayne Bay
(Rigid-Lid Model)
Fig. IV-43

WIND: 10 MPH, Southeast

AIR TEMP: 30°C

INITIAL TEMP: 24.5°C

HEAT TRANSFER
COEFFICIENT: 750 BTU/DAY$^{\circ}$F-FT^2

TIME ELAPSED: 6 HRS.

Isotherms For Vertical Section J=7

Fig. IV-44

N

27.0
26.5
26.0

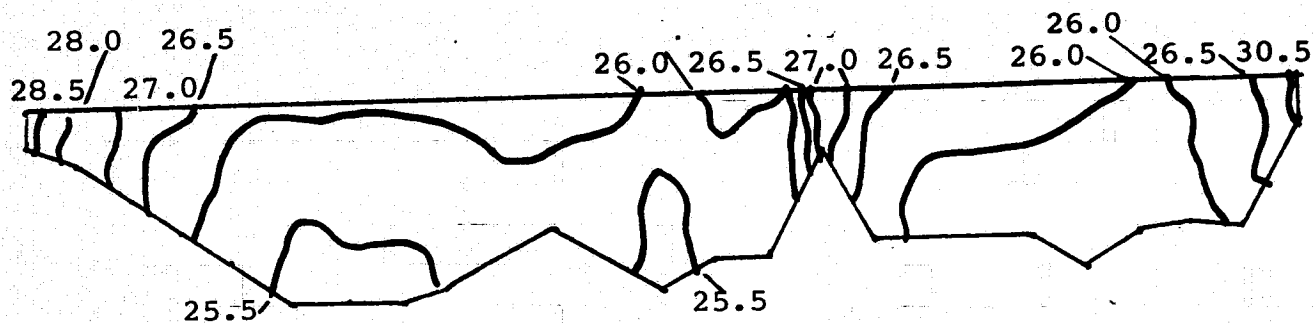26.0

26.0   26.5
       27
     27.5

26.0
26.5
27.0

Surface Isotherms for
Biscayne Bay
(Rigid-Lid Model)

Fig. IV-45

.8 kilometers

27.5

WIND:	10 MPH, Southeast
TIDE:	Incoming (10 cm/sec)
AIR TEMP:	$30^{\circ}C$
INITIAL TEMP:	$24.5^{\circ}C$
HEAT TRANSFER COEFFICIENT:	750 BTU/DAY$^{\circ}$F-FT^2
TIME ELAPSED:	3 HRS.

25.5

(DENSITY EFFECTS INCLUDED)

Isotherms for Vertical Section J=7

Fig. IV-46

N

Surface Isotherms for
Biscayne Bay
(Rigid-Lid Model)

Fig. IV-47

.8 kilometers

WIND:	10 MPH, Southeast
TIDE:	Incoming (10 cm/sec)
AIR TEMP:	30°C
INITIAL TEMP:	24.5
HEAT TRANSFER COEFFICIENT:	750 BTU/Day$^{\circ}$F-FT^2
TIME ELAPSED:	6 HRS.

(DENSITY EFFECTS INCLUDED)

WIND: 10 MPH, Southeast

AIR TEMP: $30^{\circ}C$

INITIAL TEMP: $24.5^{\circ}C$

HEAT TRANSFER
COEFFICIENT: 750 BTU/DAY$^{\circ}$F-FT^2

TIME ELAPSED: 6 HRS.

(DENSITY EFFECTS INCLUDED)

.8 kilometers horizontal scale

3 ft. vertical scale

Isotherms For Vertical Section J=7

Fig. IV-48

.8 kilometers horizontal scale

3 ft. vertical scale
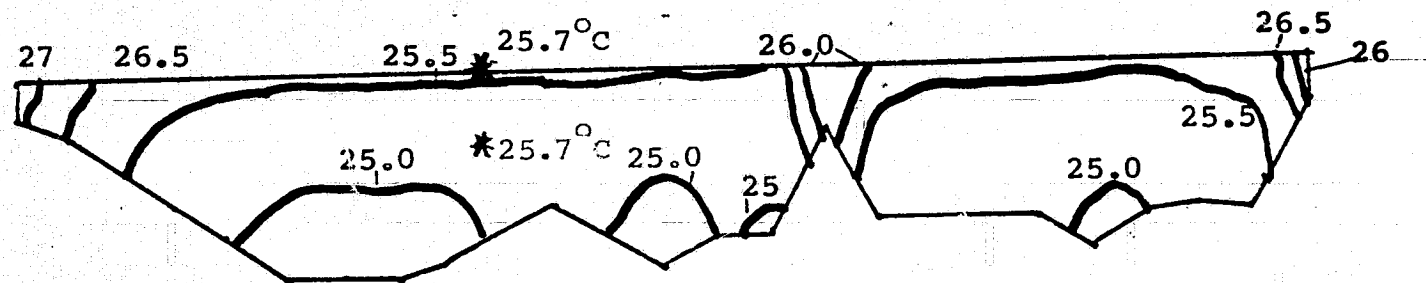
(* denotes location of ground truth measurement)

WIND: 10 MPH, Southeast
TIDE: Incoming (10 cm/sec)
AIR TEMP: 30°C
INITIAL TEMP: 24.5°C
HEAT TRANSFER COEFFICIENT:
    750 BTU /Day°F-FT²
TIME ELAPSED: 3 HRS
                (DENSITY EFFECTS INCLUDED)

SECTION: J=7

Comparison of Calculated Isotherms for Vertical Section J=7 With Ground Truth Data
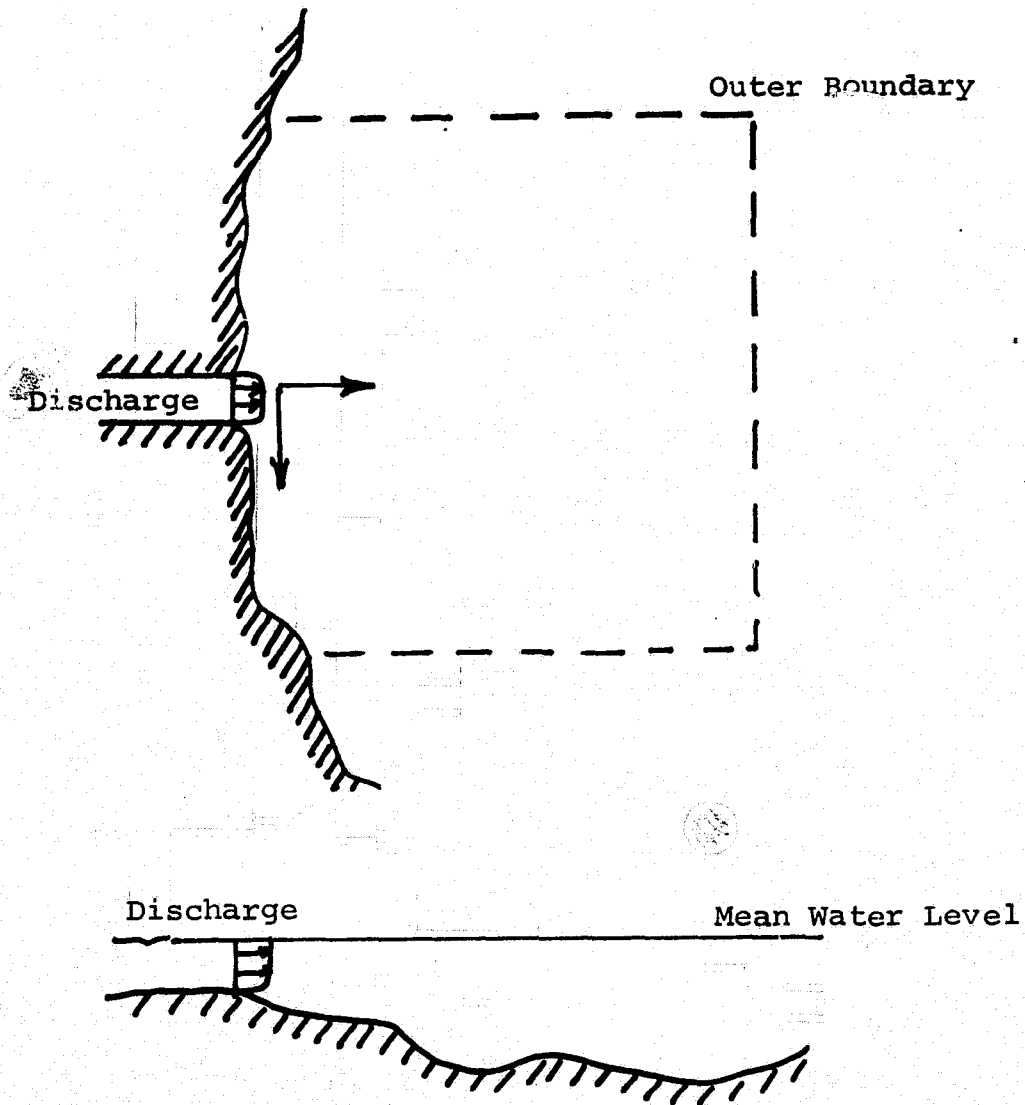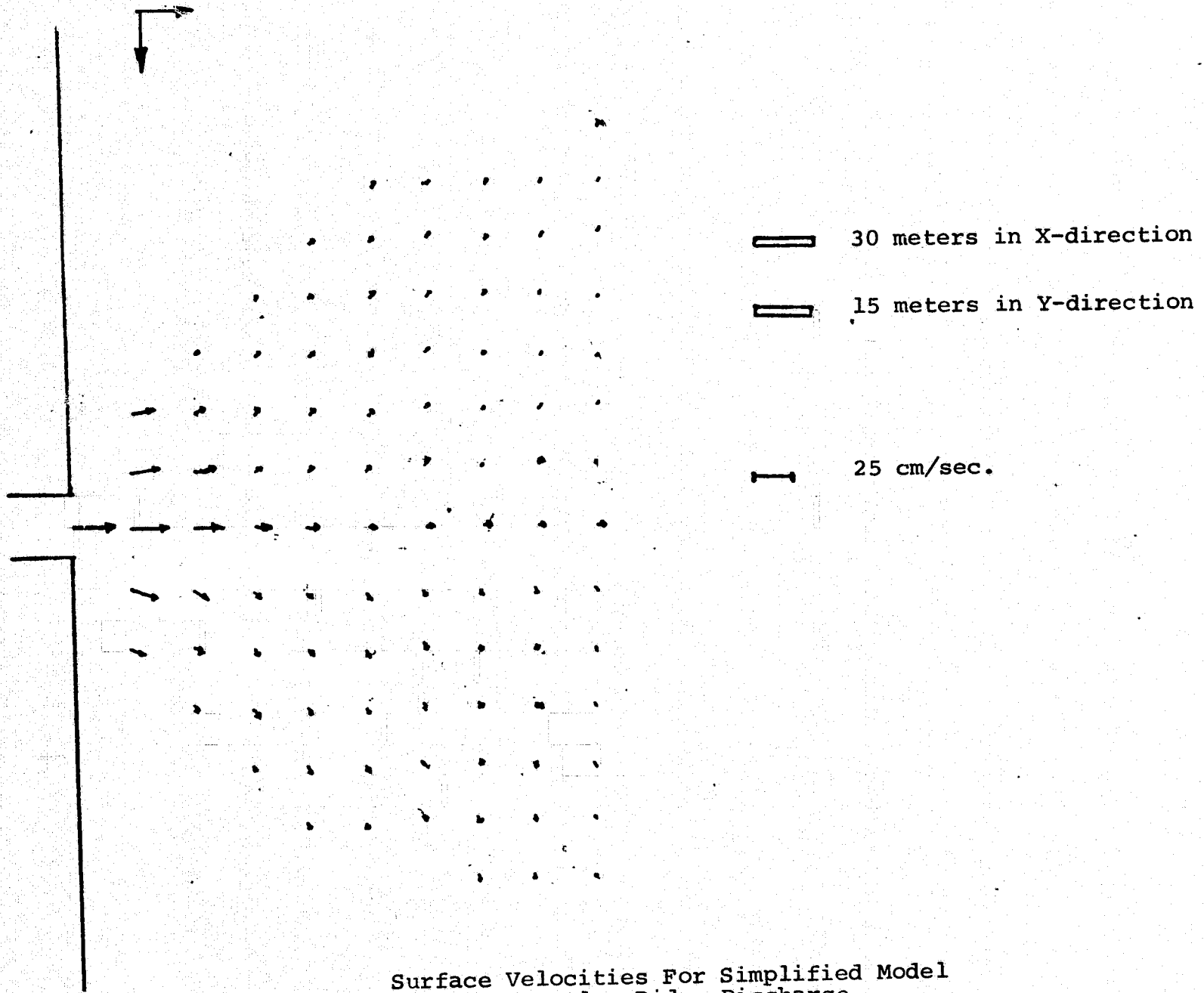
Fig. IV-49

Fig. IV-50. General Configuration of Near Field Problem

30 meters in X-direction

15 meters in Y-direction

25 cm/sec.

Surface Velocities For Simplified Model
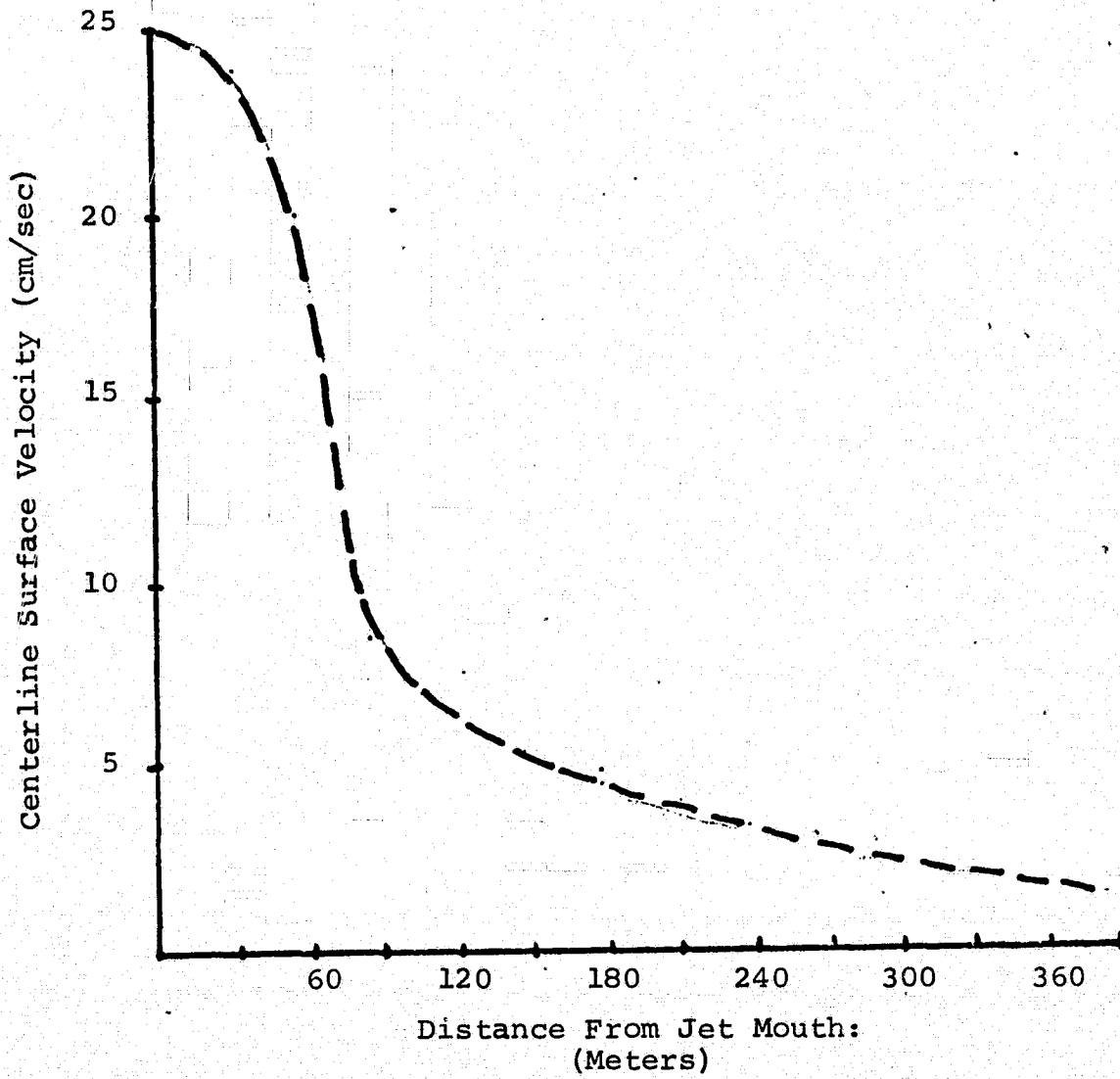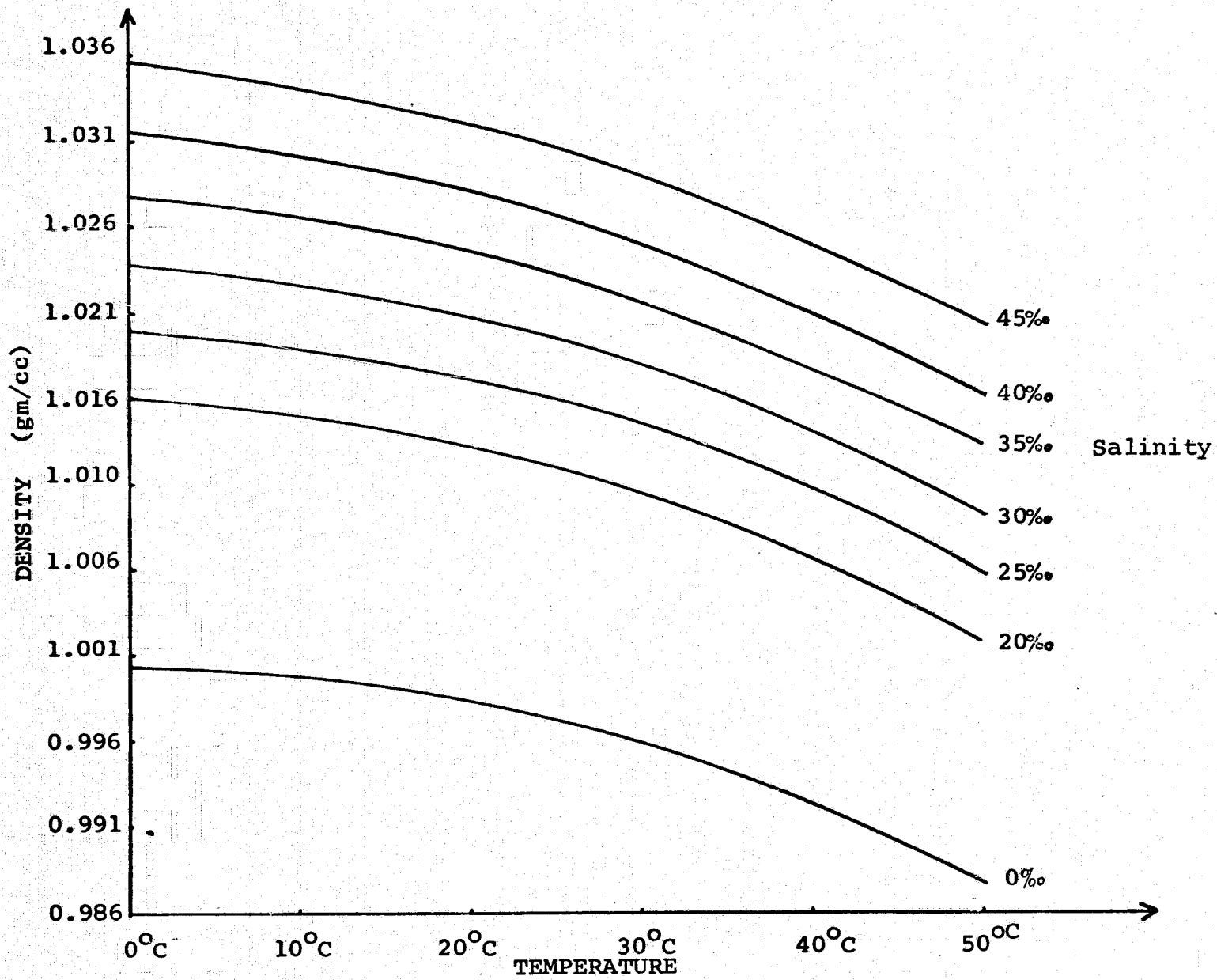of Cutler Ridge Discharge

Fig. IV-51

Fig. IV-52. Centerline Velocity Decay for Simplified Model of Cutler Ridge Discharge

Temperature Density Relations for Various Salinities

Fig. IV-53

V. TURBIDITY STUDY

A. Introduction

Until very recently, the quality of our waters in lakes, streams and near the coast at sea has been deteriorating steadily. Dredging operations, discharge of industrial and municipal wastes, and agricultural usage all have contributed to a decrease in quality of those very neighboring waters most useful to us for recreation and for fisheries. Since the general realization a few years ago that we must preserve our water heritage and limit our despoilation of this important natural resource, there seems to have been a dramatic turn of events. In some cases the rate of deterioration has apparently been slowed, and even reversed. Controls on activities which may serve adversely to affect water quality have multiplied, and considerable expenditures have been made or projected to improve water quality. Fishermen have reported improvements in the Great Lakes, and coastal waters such as Biscayne Bay seem somewhat clearer than a few years ago. But how is water quality to be measured? How are we to know whether we are winning the battle; whether the expenditures are fully effective.

Of the measurements of water quality, that of turbidity or lack of clarity is probably the most useful. This is not only because measurements can be made optically, and therefore quickly without complicated chemical analysis, but because it is exactly the lack of transparency which turbidity implies that is perhaps the most direct and obvious measure of water deterioration.

B. Defining Turbidity

The literature discloses [1] at least nine distinct definitions of turbidity or lack of clarity. Here we shall consider that turbidity causes the cloudiness in water which

obscures objects or the bottom. We shall not be concerned
with absorption, which limits the transparency of water but
does not reduce the definition or contrast of what we see.
The cloudiness that we wish to measure is caused by suspended
small particles in the water. When light encounters these
particles it is scattered in all directions. The result is
a decrease in clarity and contrast of an image.

Consider a beam of monochromatic light incident on
a sample of water. It is assumed to have wavelength λ and
irradiance I_o. As it passes through the water, the intensity
(irradiance) will decrease as energy is absorbed and scattered.
As mentioned above, we will not concern ourselves with the ab-
sorbed radiation, since absorption only decreases the intensity
of the image, not its clarity or contrast. We will therefore
evaluate only the scattering which occurs.

In an infinitesimal volume $dv = dxdydz$, a certain
amount of light, dI, is scattered. This amount is proportional
to the incident intensity $I_o(\lambda)$, to the volume $dxdydz$, and is
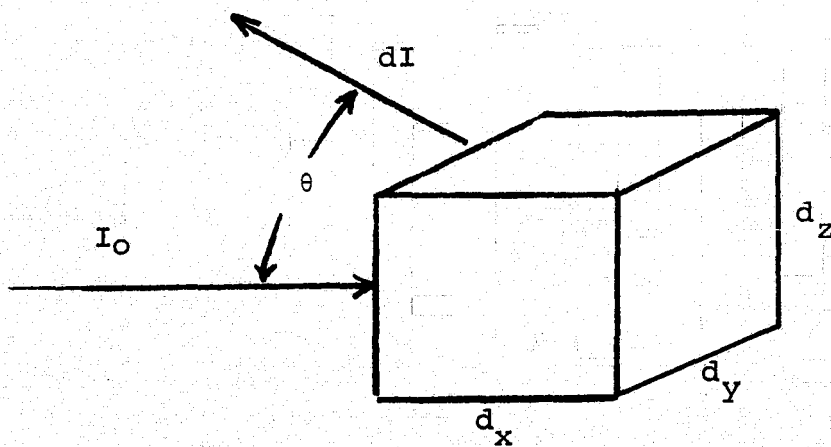a function of angle and wavelength.

Figure V-1

Then $\qquad dI = I_o \; \alpha(\theta,\lambda) \; dx \; dy \; dz \; d\omega \; d\lambda$ $\qquad$ (1)

and $\qquad I = \int\limits_x \int\limits_y \int\limits_z \int\limits_\omega \int\limits_\lambda \alpha(\theta,\lambda) \; I_o \; dx \; dy \; dz \; d\omega \; d\lambda$ $\qquad$ (2)

Here $\alpha(\theta,\lambda)$ is the scattering coefficient which is to be measured. In those cases where the particles doing the scattering are small, of diameter d, the same order or smaller than the wavelength, λ, of the light, the angular dependence is very complicated. In most of the turbidity which affects water quality, however, the particles are considerably larger than the wavelength, $d \gg \lambda$, and the variations with angle are simple and not very strong; generally having the shape [2] shown in Figure V-2.
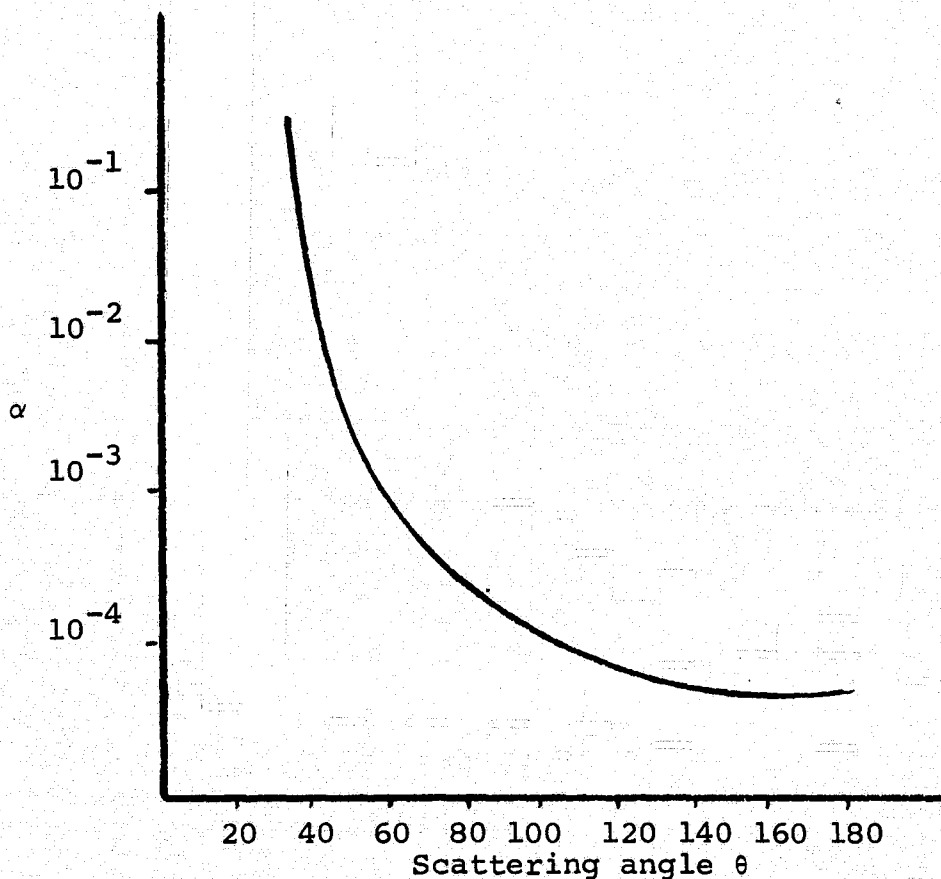

Figure V-2

Measurements of turbidity are thus equivalent to the
measurement of scattering, which is dependent on angle as
shown in Figure V-2. A type of scattering meter, the nephelo-
meter is adapted to measurements at 90°. Other methods in-
clude the taking of water samples, the Secci disk, and measure-
ment of a light beam after passage through a definite length
of water compared to its original intensity. These methods
require slow sampling, or a bulky optical assembly, difficult
to use in the sea, and liable to destruction by wave and ship
motion.

C. Turbidity Study Plan

We plan a three-stage approach to the problem of
turbidity:

1) The use of ERTS Satellite and/or airplane
   data suitably enhanced and applied as a time
   series for an overall view of a relatively
   large area.

2) The use of a shipborne and later an airborne
   laser probe to measure backscatter turbidity
   as a function of depth.

3) The development of a new ground truth turbidity
   meter based on a self-extinction method.

These are discussed in turn:

a) ERTS Satellite and/or Airplane Turbidity
Measurements.

Satellite and aerial photographic coverage aid in
understanding the gross movements of suspended solids, providing
information of circulation patterns [3], [4],[5]. When used in
conjunction with field methods, such coverage minimized the
physical sampling requirements.

Perhaps more important than the photographic data
taken by satellites and airplanes are the precise radiometric

data which are gathered by some satellites (ERTS-1 and ERTS-2) and specially equipped aircraft. Transmission of this data are routed directly onto computer compatible tape. This increases the resolution by a factor of 7.9 over conventional photographic techniques. (Computer tape commonly has 7 bit resolution or 127 gray levels where photographic products have 16 gray levels. [6]).

Bands 4 and 5 (approximately 5500 to 4500 and 6500 to 5500 angstroms respectively) of the Earth Resources Technology Satellite-1 (ERTS-1) have proved to be very effective in the observation of current patterns due to differential concentrations of suspended sediment [7]. Also observable by ERTS-1 imagery are waste effluents, production of planktonic organisms, river effluent and coastal landslides, variance in river discharge, and intensity of surf action [8].

ERTS imagery photographic products may be enhanced using a densitometer, and the computer tapes enhanced using computer techniques. Enhancement techniques may be used to show the distribution of turbidity, from which a time series may be obtained from multiple imagery of the same location. Also the effects of tide may be observed but only to a limited degree since ERTS overpasses occur once every eighteen days.

Using both enhancement techniques, photographic and computer, we propose to collect a time series of ERTS images, with corresponding field data, to draw conclusions into the nature, source and movement of turbidity through Biscayne Bay. By the use of time series, it is expected that the effects of turbidity may be separated from those due to reflection from the bottom, since the latter are probably much more slowly varying.

b) Laser Application to Measure Vertical Sea Temperature and Turbidity

This program is being developed by the Laboratory for Optics and Astrophysics of the Department of Physics, University

of Miami, under NASA contracts NAS10-8600 and NAS10-8795.

It is described in the Detailed Technical Report
NASA CR-139184 by J. G. Hirschberg, A. W. Wouters, F. N.
Cooke, Jr., K. M. Simon and J. D. Byrne, dated January 1975.

This method evaluates the ratio of the backscattered
Tyndall scattering to the backscattered Brillouin scattering.
Only the Tyndall scattering causes turbidity, but since both
are proportional to the incident light, the method is self-
compensating.

c) A Compact In-Situ Turbidity Measuring Meter

In order to evaluate results from both preceding
systems a compact ground truth turbidity measuring device is
necessary. Ordinary available meters either possess a very
small scattering volume and hence are insensitive, or are
bulky and hazardous to operate at sea.

This instrument measures the amount of backscatter,
or scattering at about 180° per unit length of water. When
looking downward into the sea with the light above, or when
illuminating the sea with a light mounted close beside the
viewer, this is the type of scattering which prevents observa-
tion when present. In order to eliminate background inter-
ference without a bulky mechanical target, near infrared
radiation is used, produced by a solid state laser. This
radiation is rapidly absorbed by water, so that the effect is
like looking into a black hole at night, even in the daytime.

The instrument contains one or more solid state lasers,
emitting a collimated beam of radiation in the wavelength
range from 700 to 850 nanometers. In this spectral region,
the transparence of the water is quite low; from a meter to a
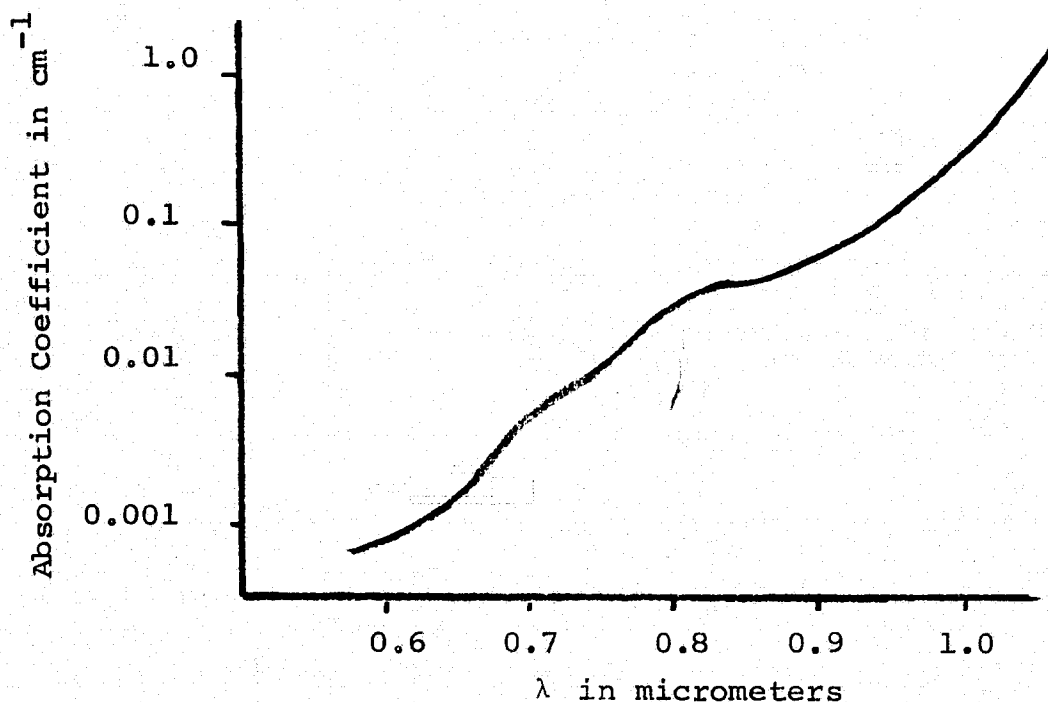few centimeters depending on the wavelength, see Figure V-3.

)

Figure V-3

A wavelength is chosen for which the light has an effective path of 10 to 40 cm. Thus, the background is black, exactly as though a black background target were used, without the necessity of providing a mechanical structure to hold it. This greatly simplified the apparatus for use at sea since no boom and disc are used.

A further advantage is that the acceptance beam and illuminating beam are in the same volume, being anti-parallel so that the scattering volume is maximized. This makes the instrument far more sensitive than the nephelometer type where the beams are crossed.

Finally, because the sea is absorbing to the
radiation used beyond about 20 cm daylight observations are
as favorable as nighttime for depths beyond about half a
meter.

REFERENCES

1. McCluney, W.R., "Radiometry of Water Turbidity Measurements," Journ W.P.C.F. $\underline{47}$, 252 (1975).

2. Kullenberg, G., "Optical Aspects of Oceanography," Ed. N.G. Jerlov and E. Steemunn Nielsen, Academic Press, 1974, p. 30.

3. Klamas, V., Borchardt, J.F., and Treasure, W.M., "Remote Sensing of Environ," $\underline{2}$ (1973).

4. Wright, F.F., Sharma, G.O., and Burbank, D.C., Paper M-8, NASA SP-327 (1973).

5. Klamas, V., Srna, R., Treasure, W.M., and Otley, M., Paper M-3, NASA SP-327 (1973).

6. Kritikos, H, Yorinks, L., and Smith, H., "Remote Sensing of Environ," $\underline{3}$ (1974).

7. Anderson, D.M., Gatto, L.W., McKim, H.L., and Petrone, A, Paper M-9, NASA SP-327 (1973).

8. Carlson, P.R., Janda, R.J., and Conomos, T.J., Paper M-6, NASA SP-327, (1973).

APPENDIX I

EQUATION OF STATE:

The generalized equation of state for water may be written as

$$\rho = \rho(S,T,p)$$

where

ρ = density

T = temperature

P = pressure

S = Salinity

For most applications the effect of pressure on density is minimal since water is incompressible. Therefore, the significant variables are salinity and temperature. Thus :

$$\rho = \rho(S,T)$$

Dittmar (1884) showed that the majority of ions in sea water are present in remarkably constant ratios to one another.

Salinity as defined by Forsch et al. (1902) is "the total solid material in grams contained in one kilogram of sea-water when all carbonate has been converted to oxide, the bromine and iodine replaced by chlorine, all organic matter completely oxidized, and the residue heated to a constant weight at $480^{\circ}C$."

So, salinity is not the total salt content. Estimates by Lyman and Fleming (1940) related salinity S to total salt content by a linear relation :

$$S_{total} = 0.043 + 1.0044 \ S.$$

The chlorine-equivalent of the precipitated halides in grams per kilogram of sea water is called the chlorinity of sea-water. An empirical relation is :

$$S = 0.03 + 1.8050 \ Cl.$$

here salinity S and chlorinity Cl are expressed in parts per thousand (0/00).

Forsch et al. (1902) related specific gravity to chlorinity (at $0^\circ C$ and atmospheric pressure):

$$\sigma_O = 0.069 + 1.4708 \, CL - 1.570 \times 10^{-3} Cl^2 + 3.98 \times 10^{-6} Cl^3$$

σ_O = specific gravity anomaly

$$\sigma_O = 10^3 (S_O - 1)$$

here S_O = specific gravity.

The effect of temperature variation is included as:

$$\sigma_t = A + B\sigma_O + C\sigma_O^2$$

where
A, B and C are functions of temperature.

Knudsen (1901) used the formula :

$$\sigma_t = \Sigma_t + (\sigma_O - \Sigma_O)[1 - A_t + B_t(\sigma_O + \Sigma_O)]$$

here

$$\Sigma_t = \frac{-(\theta - 3.98)^2 (\theta + 283)}{503.70(\theta + 67.26)}$$

$$\Sigma_O = -0.1324$$

$$B = 1 - A_t = 1 - 4.7867 \times 10^{-3}\theta + 9.8185 \times 10^{-5}\theta^2 - 1.0843 \times 10^{-6}\theta^3$$

$$C = B_t = 1.8030 \times 10^{-5}\theta - 8.164 \times 10^{-7}\theta^2 + 1.667 \times 10^{-8}\theta^3$$

$$A = \frac{(4.53168\theta - 0.545939\theta^2 - 1.98248 \times 10^{-3}\theta^3 - 1.438 \times 10^{-7}\theta^4)}{(\theta + 67.26)}$$

where θ is temperature in degrees Celsius.

For pure water $\sigma_O = \Sigma_O = 0.1324$

Therefore $\sigma_t = \Sigma_t$

Another approach for particular cases is to fit the data to a suitable curve through density - temperature data. The C.R.C. Manual (1968) gives data for pure water in the range of $10^\circ - 50^\circ C$.

Temperature (°C)	Density (gm/per cc)
10	0.99973
15	0.99913
18	0.99862
20	0.99823
25	0.99767
30	0.99567
35	0.99406
38	0.99229
40	0.99224
45	0.99025
50	0.98807

A second degree least-square curve fit is used to obtain the empirical relation below:

$$\rho = 1.000428 - .0000019\theta - .0000046\theta^2.$$

Fig. IV-53 shows the variation of density with temperature and salinity calculated from the above formulae.

In Biscayne Bay the salinity ranges from 35 to 38°/00. The corresponding density change has been ignored in the rigid-lid model since the rigid-lid model is primarily intended for inland water bodies where salinity is unimportant. Even in Biscayne Bay, the salinity variation is small so its effect on circulation is minimal and ignoring it in the thermal pollution math model can be justified.

A second degree fit for the 35°/00 salinity data yields a formula relating density and temperature; which has been used in the rigid-lid model application to Biscayne Bay:

$$\rho = 1.029431 - .0000020\theta - .0000048\theta^2.$$

For the free surface model, the salinity may or may not be included depending on the densimetric Froude number of the water body. The system of equations described can then be used to approximate the effects of variations in salinity and temperature.

APPENDIX II

A Model of the Sea Surface
Consistent with Temperature Measurements

Our measurements have shown that the infrared measurements of the sea surface temperature are often not in agreement with measurements made with thermistors of the water just beneath the surface. In many cases these measurements are about a degree lower than the bulk measurements. When made from a satellite or high-flying aircraft, the reason for any discrepancy may possibly be ascribed to uncertainty in the quantity of water vapor in the atmospheric layer between the sensor and the sea surface. With our low-flying aircraft, NASA 6, this is not likely to be the case. Radiosonde data was available for all our experiments, and was utilized to correct the infrared observations.

In addition, a hand-operated infrared sensor, the Wahl Corp. Heat Spy was used directly from the boat. In this case where no water vapor correction applies, the measured sea surface was also usually about a degree cooler then the thermistor measurements. In the following paragraphs a model yielding a possible explanation of these results is presented.

As Figure 1 shows, the infrared in the 8 to 12 micron band which is used for infrared measurements of temperature is so strongly absorbed by water that infrared measurements are sensitive only to the upper 0.01 mm of the water depth. If for some reason this layer is warmer or cooler than the rest of the sea, the infrared results will not agree with bulk measurements. The below described model of the sea surface will serve to suggest why the top millimeter or so of the sea may be substantially cooler than the underlying water under typical conditions. We shall assume that these conditions include a relatively calm sunlit day, with the sun angle greater than about 30 degrees. The water surface is then relatively
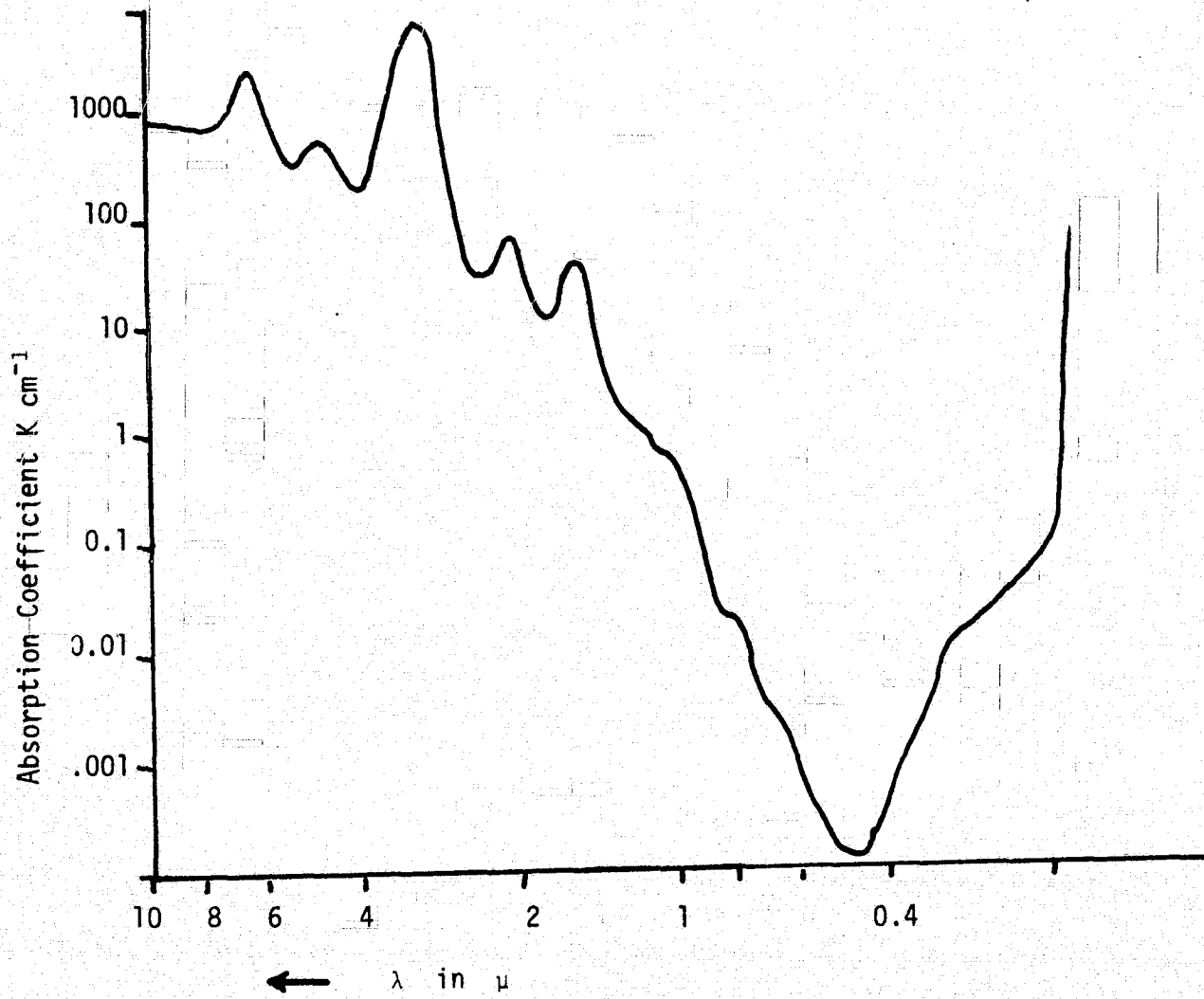
Figure[1] 1

[1]Redrawn from Brochett, Biological Effects of Radiation - Duggar -
McGraw Hill.

smooth without foam, spray or many breaking waves. These conditions

correspond rather closely to those obtaining during most of the experi-

ments on which we report.

The principal method of vertical heat transfer in the sea is by

convection - the bulk transfer of fluid. However, unless the convective

currents are very strong, or there is considerable wave motion, there

will in general be a thin layer of water at the sea surface where con-

vection cannot occur. This "skin" is maintained by the surface tension

of the water, and heat is transfered through this layer by radiation and

conduction alone. Let the thickness of the skin layer be t. In Figure 2,

we represent the heat budget of the skin. A is the flux of sunlight

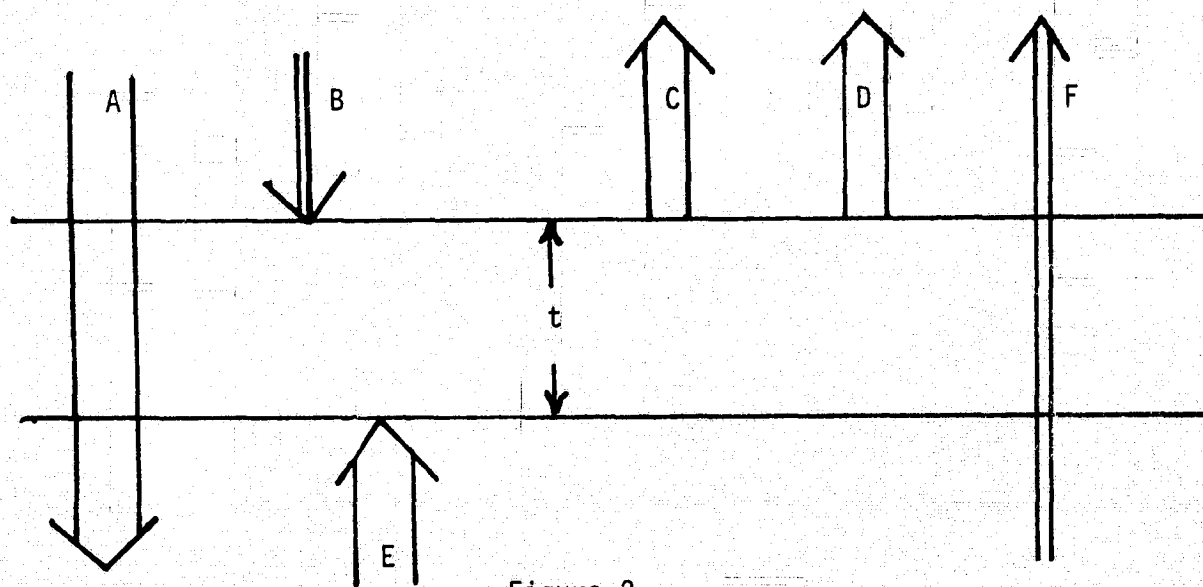falling on the sea. The sun's radiation is centered at about 530 micrometers,

Figure 2

and since water is relatively transparent to this radiation only a negligible

part is absorbed in the skin; most of it passes into deeper water where it

is finally absorbed or scattered back to the surface. B is infrared

re-radiated from the clouds and atmosphere, the total amount of which is small compared to A, except at night. C and D are the principal heat-loss processes for the sea. Let C be the infrared radiation, which for a temperature of 300°K has a maximum at about 12 micrometers. This cools directly only the upper 10 micrometers of the skin since water is practically opaque to this radiation as shown in Figure 1. D represents the heat loss by evaporation. This also cools only the upper layer of the skin directly, since only the few top molecular layers evaporate under the quiet sea-surface conditions we are considering. E is the delivery of heat from the deeper water to the skin layer, either by con-duction or convection. Finally F is the sunlight scattered by the water or reflected from the bottom. Typically this will be a small fraction of the arriving flux A. In this approximate treatment we shall neglect B and F since they are ordinarily, under the conditions assumed, much smaller than the other fluxes.

For a steady state situation we can then write:

$$A = E$$

and
$$E = C + D$$

Now A is the arriving solar radiation. An approximate 24 hour average value for 25° latitude is[2] 0.32 kilowatt/(meter)^2.

The principal mode of heat transfer in the skin layer is assumed to be conduction. The rate of heat conduction, dQ/dt, is given[3] by

$$\frac{dQ}{dt} = - Ak \text{ grad } T$$

---

[2]David Brunt. "Physical and Dynamical Meterology" Cambridge, England, 1941, p. 155.
[3]Ingersoll, Zobel and Ingersoll, "Heat Conduction" McGraw-Hill, 1948, p. 3.

where A is the area, k the thermal conductivity, and T the temperature. In terms of the flux of heat, ω, for conduction in one dimension this can be written:

$$\omega = - k \frac{\partial T}{\partial x} \quad .$$

For water, $k \cong 6 \times 10^4$ ergs/sec cm $°K^4$, A = 0.32 kilowatt/m² or 0.32×10^6 ergs/cm²-sec

$$\frac{\partial T}{\partial x} = - \frac{\omega}{k} = \frac{0.32 \times 10^6}{6 \times 10^4}$$

or, using differences:

$$\Delta T = 8\Delta x \quad .$$

If ΔT is about 1°K, which is typical of our observations, Δx is about 1 millimeter, which seems reasonable, in view of the strong surface tension of seawater. This tends to explain the depression by about 1 degree K of the infrared temperatures,which are representative only of the upper 1/100 mm of the ocean, compared to thermistor measurements at least a few millimeters below the surface. Refinements of this surface model may be made by combining it with the generalized force-surface model developed elsewhere in this report.

---

[4]Quoted in Hirschberg, Wouters, Cooke, Simon and Byrne. Detailed Technical Report NASA CR-139184, January 1975, p. 32.

ACKNOWLEDGMENTS